Towards Hybrid Qubits in Bilayer Graphene Quantum Dots

Master's Thesis

submitted to
Indian Institute of Science Education and Research Tirupati
in partial fulfillment of the requirements for the
BS-MS Dual Degree Programme

by

Rajlaxmi Vilas Bhoite
Roll Number: 20191138

Supervisor: Dr. Christoph Stampfer
RWTH Aachen University, Germany

April, 2024

Certificate

This is to certify that the MS Thesis entitled Towards Hybrid Qubits in Bilayer Graphene Quantum Dots submitted towards the partial fulfilment of the BS-MS dual degree programme at the Indian Institute of Science Education and Research Tirupati, represents the study / work carried out by Rajlaxmi Vilas Bhoite at RWTH Aachen University under the supervision of Dr. Christoph Stampfer Department of Physics, during the academic year 2023-2024 and the same has not been submitted for any other degree or diploma of any other university or institute.

Name of student: Rajlaxmi Vilas Bhoite

Roll Number: 20191138

Signature of student:

Date : 04.04.2024

Name of Supervisor: Dr.Christoph Stampfer

Signature of Supervisor:

Date: 04.04.2024

Declaration

I declare that the matter presented in the MS thesis entitled Towards Hybrid Qubits in Bilayer Graphene Quantum Dots are the results of the work carried out by me at the Department of Physics, RWTH Aachen University under the supervision of Dr.Christoph Stampfer.
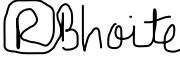
I declare that the study / work submitted is my own and expressed in my own words. My contribution to this work and those of the other collaborators (if any) have been explicitly indicated below.

I confirm that appropriate credit has been given within this thesis where reference has been made to the work of others. I also declare that I have adhered to all principles of academic ethics and integrity and have not fabricated or falsified any idea / data / fact / image source in my submission.

I understand that violation of the above will lead to disciplinary action by the Institute and can also evoke penal action from the sources which have thus not been properly cited or from whom proper permission has not been obtained.

Name of student: Rajlaxmi Vilas Bhoite

Roll Number: 20191138

Signature of student:

Date : 04.04.2024

Endorsed by:

Name of Supervisor: Dr. Christoph Stampfer

Signature of Supervisor:

Date: 04.04.2024

Acknowledgements

First of all, I would like to thank Professor Christoph Stampfer for providing me the opportunity to be a part of his dynamic research laboratory at RWTH Aachen University. I would also like to express thanks to Professor Anindya Das from IISC for being a part of the thesis committee. This exciting research project wouldn't be possible without the unwavering support of Samuel Moeller. His expertise in Quantum dots and immense clarity in explaining any topic of scientific interest motivated me a lot to continue my career in research. The opportunity and trust he had in me to be a part of a collaborative project under the guidance of Philipp Schmidt has become a game changer for my research career apart from making me a lot more confident. I am forever thankful to him. Being new to this dynamic research atmosphere he always helped me with many things before I joined the lab and working under his supervision I never felt demotivated for not knowing something new to me. Also, thank you for the wonderful game evening and talks.

I would like to thank Philipp Schmidt for his stupendous amount of effort in teaching me a lot of new things that were required in fabricating devices for my thesis project. His expertise in superconductivity followed by the guidance on how to plan scientific research and how to do scientific writing was indeed wonderful. Working under his supervision always gave me a new angle to direct my research ideas. I would like to thank Katrin for giving me that emotional support whenever I was stressed about my thesis. Talking to her used to make me feel at home. I want to thank Lucca and Leon for being there as wonderful friends in the office and the ones who also helped me with small queries.

Most importantly I want to thank my elder brother Omkar. Coming to Germany wouldn't have been possible without his help. His constant support, strong ambition, and attitude towards things, or rather a problem in life have taught me a lot. I am grateful for the amazing conversations with my grandparents and their blessings. I want to thank my parents for the immense love, care, and faith they have in me. Lastly, I also want to thank my friend Ashwin for helping me settle in a new country, with latex and Akhil for his help in CAD software. My faith in Lord Ganesha always helps me work towards my ultimate goal in life and I believe his blessings are making me stronger with each new experience just like this master's thesis experience did.

"Everything is theoretically impossible until it is done." – Robert A. Heinlein

ABSTRACT

Superconductor and semiconductor technologies are two of the most promising ways to build quantum computers for information processing. Semiconductor quantum dot offers a scalable approach for trapping single electrons in nanometre-sized regions, allowing for precise control and manipulation of electronic spin. For this thesis, the interest is to investigate the interactions when a quantum dot in BLG is proximitised to a BCS superconductor. The study involves understanding various kinds of processes that occur at an N-QD-S-QD-N interface. The fabrication process for this hybrid device involved micromechanical exfoliation and stacking of 2D heterostructures where the stacks were characterized with Raman spectroscopy and Atomic force microscopy. Different types of devices were designed to study Andreev supercurrent, Cooper pair splitting, and Cross-Andreev Reflection or Elastic Co-tunneling. These studies form a basis for understanding the possibility of encoding spin/charge information in specially formed Andreev-bound states. Lastly, the research is summarized by demonstrating the results of quantum transport measurements to characterize the formation of a single quantum dot and when this quantum dot is coupled to a superconductor. This has provided feasibility for doing the intended measurements in the fabricated devices.

Contents

List of Figures

Chapter 1

Introduction

1.1 Motivation

Qubits are basic units for processing information in a quantum computer just like a classical bit in a classical computer. These are quantum mechanical two-level systems where the general state can be described by a superposition of all available quantum states. The creation of qubits and being able to compute quantum information is possible nowadays with a lot of technologies ranging from trapped ions [1], Rydberg atoms [2], sophisticated superconducting circuits [3], spin qubits [4], and photonic quantum computing [5]. One of the very interesting quantum mechanical properties is quantum entanglement which can aid in storing and processing quantum information with the potential to revolutionize this noisy intermediate-scale quantum (NISQ) era.

The idea of combining superconductor and semiconductor systems has provided a dynamic platform for a wide range of studies [6, 7, 8, 9]. Electrostatically defined Quantum dots (QDs) offer precise control over electrons although they come with several limitations. Combining these QDs by proximity coupling a superconductor in devices like cooper pair splitters (CPS) has become a powerful tool for enabling future quantum technology [10, 11, 12]. The normal metal and superconductor interface has helped to understand many emergent phenomena like the formation of Majorana bound states with tunnel spectroscopic measurements [13, 14, 15], Cross-Andreev Reflection [16], and studying quantum entanglement [12]. Although this has been realized in InSb and GeSi nanowires [17, 18], studies of combining a bilayer graphene QD to a superconductor have not been done before. One might question the purpose of studying it on a different quantum system. The broader picture is of course to create an Andreev qubit [19, 20] in bilayer graphene QD but what lies underneath is an attempt to engineer a model that can

help develop a fundamental understanding of Andreev processes arising in this system and aid the search for majorana fermions by gaining control to manipulate Andreev bound states (ABS). Semiconducting platforms offer an advantage because of their versatility in qubit implementation, scalability, and longer coherence times along with the disadvantage of susceptibility to environmental noise and error correction [21]. By integrating them into superconducting electronics, the goal is to reach a hybrid ultimatum where the disadvantages in these individual systems can be mitigated [22].

Bilayer Graphene (BLG) is a novel material that exhibits remarkable properties like excellent mobilities of up to 40,000 cm^2/Vs [23] and thermal conductivity of 2,800 Wm^{-1}K^{-1} at room temperature [24, 25]. The Nobel Prize in Physics awarded to Andre Geim and Konstantin Novoselov in 2010 marked a significant milestone, sparking a new era in research focused on 2D materials [26]. Their pioneering work in isolating atomically thin layers of graphene from bulk graphite crystals, an extraordinary two-dimensional material initiated a paradigm shift [27] in research across various scientific disciplines ranging from biomedical applications and flexible electronics [28, 29]. While superconducting materials have been extensively studied for more than 100 years with several types of superconductors already discovered like conventional metallic superconductors [30], high-temperature cuprate superconductors [31, 32], and more recently, two-dimensional superconductor niobium diselenide [33] not all of these are studied extensively, making superconductivity still a vast and engaging field of research. In the scope of this thesis, the interests lies in combining aluminum and/or niobium to BLG QDs and investigating interactions when these quantum dots are coupled with Cooper pairs rather than individual electrons. The Cooper pairs from the superconductor can influence the behavior of electrons in the semiconductor, leading to the formation of novel quantum states.

The motivation for this thesis is to explore possibilities for creating an Andreev qubit with the thought of making the design viable for studies in hybrid systems. Multiple numbers of qubits are predicted to maintain quantum entanglement in space. Passing on the information with multiple numbers of entangled qubits in a 1-D or 2-D array of coupled QDs could be a much faster way of communicating information and in computations. The attempt to create a 2D array of QDs in BLG is not yet explored although there have been studies on this in Si/SiGe heterostructures [34]. Quantum entanglement offers ways of enhancing computational possibilities by 2^n folds. Having five entangled qubits would increase the capabilities by thirty-two times. This is another reason why future quantum processors are predicted to be fueled with the properties of entangled qubits [12] and as a roadblock for quantum cryptography in secured communication.

1.2   Research Questions

Before describing what each section of this thesis wants to convey, it is essential to draw attention to some important questions that this study aims to answer and contribute to. The first and most basic question is how to create a superconductor quantum dot device in BLG. What kind of andreev processes can occur at the interface and how does the presence of a superconductor influence the working of QDs? How can bell inequalities be tested in such a hybrid system? Is it possible to gain control over quantum processes like Cross Andreev Reflection (CAR) and Electron Co-tunneling (ECT)? How does the Cooper Pair Splitter (CPS) help to split electrons from a Cooper pair into proximitised QDs? What are the practical benefits of achieving this control?

1.3   Outline of Thesis

This subsection describes the general outline for the upcoming chapters. Chapter 2 focuses on building a theoretical background for the experimental studies for this thesis. It begins with the introduction of "Bilayer Graphene" followed by a section describing the fundamentals of QDs with a simple capacitor model. Finally, the superconductor semiconductor system is studied where a family of andreev processes across a normal-superconducting interface are described. Chapter 3 states the experimental methods involved in the fabrication of the device design starting from the sample layout, the nanofabrication process, and lastly, the measurement section which includes how is a quantum dot created and how can the transport be tuned for an N-QD-S-QD-N junction. The purpose of each device along with a possible measurement scheme has also been stated in this section. In Chapter 4, the results of transport measurements performed on a single quantum dot are described and consequently, the shift of coulomb diamonds for an N-QD-S junction is demonstrated. Finally, chapter 5 summarizes the research along with an outlook of what other studies are possible in these hybrid devices.

Chapter 2

Theoretical Background

2.1 Bilayer Graphene

Bilayer Graphene (BLG) consists of two layers of monolayer graphene sheets held together by weak van-der-waals forces. Each layer forms a honeycomb lattice structure made up of sp^2 hybridized carbon atoms. These carbon atoms are separated by an interatomic distance of 1.42 Å and a bond angle of $120°$ creating a trigonal planar geometry. For a Bernal stacked BLG, the unit cell comprises four atoms which are labeled as A_1, B_1 on the lower layer, and A_2, B_2 on the upper layer as depicted in figure 2.1 (b). The atom B_1 lies exactly below A_2 which are referred to as dimer sites while the rest two atoms A_1 and B_2 form the non-dimer sites. At dimer sites, the electronic orbitals are coupled by relatively strong interlayer coupling as compared to non-dimer sites. In order to describe the lattice structure for BLG two lattice vectors are needed i.e. $\mathbf{a}_1$ and $\mathbf{a}_2$ with $|a_i|= a = 2.46$ Å. This corresponds to $\sqrt{3}$ times the bond length between two carbon atoms [35]. The vectors $\mathbf{a}_1$ and $\mathbf{a}_2$ are:

$$\mathbf{a_1} = \left(\frac{a}{2}, \frac{\sqrt{3}a}{2} \right) \qquad \mathbf{a_2} = \left(\frac{a}{2}, -\frac{\sqrt{3}a}{2} \right) \qquad (2.1)$$

The reciprocal lattice is spanned by the lattice vectors $\mathbf{b}_1$ and $\mathbf{b}_2$ in the momentum space which are given by:

$$\mathbf{b_1} = \left(\frac{2\pi}{a}, \frac{2\pi}{\sqrt{3}a} \right) \qquad \mathbf{b_2} = \left(\frac{2\pi}{a}, -\frac{2\pi}{\sqrt{3}a} \right) \qquad (2.2)$$

In order to describe the band structure for BLG, the tight-binding model can be used. This model is explained by considering an arbitrary crystal with translational invariance and M number of atomic orbitals ϕ_m per unit cell with m = 1...M.
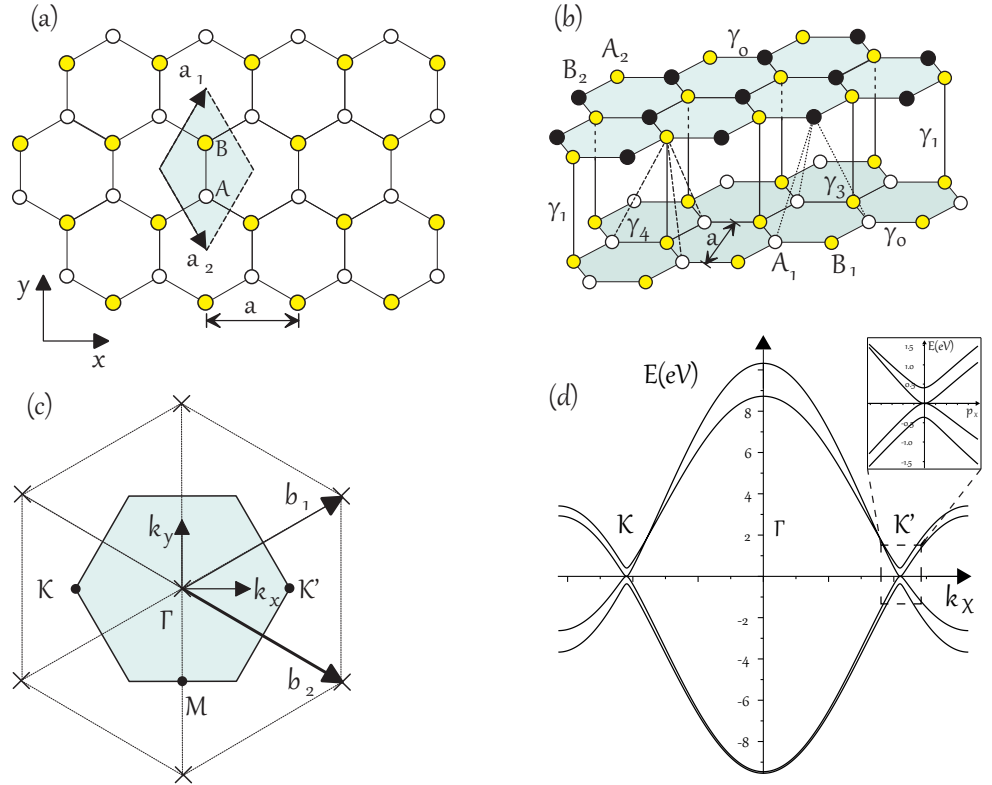
Figure 2.1: (a) Top View of Hexagonal Lattice Structure of BLG. Dimer atoms are illustrated in yellow and separated by lattice constant 'a'. (b) Side view of crystal structure. Carbon atoms in white (black) are non-dimer atoms in the lower (upper) layer. The vectors **a**$_1$ and **a**$_2$ form the unit cell which contains four atoms A$_1$, A$_2$, B$_1$, B$_2$. The hopping parameters γ_0, γ_1, γ_2, and γ_3 describe the nearest neighbour hopping between the sites. (c) First Brillouin zone of BLG is formed by the reciprocal lattice vectors **b**$_1$ and **b**$_2$ with high symmetry points Γ, M, K and K' (d) Energy bands of BLG obtained from the BLG Hamiltonian as a line cut from Γ to K, K'. Figure is adapted from [35]

The Bloch states at any given position vector r and wave vector k for this crystal can be defined as:

$$\Phi_m(k,r) = \frac{1}{\sqrt{N}} \sum e^{ikR_{m,i}} \phi_m(r - R_{m,i}), \tag{2.3}$$

Thus, the wavefunction for the electrons can be expressed as a linear superposition of these Bloch states

$$\Psi_j(k,r) = \sum \psi_{j,m}(k)\Phi_m(k,r), \tag{2.4}$$

where $\psi_{j,m}$ are coefficients of expansion. There are M different energy bands where the energy of the jth band is given by $E_j(k) = \langle \Psi_j | H | \Psi_j \rangle / \langle \Psi_j | \Psi_j \rangle$. By minimizing the energy

$E_j(k)$ with respect to $\psi_{j,m}$ the following expression can be obtained

$$H\psi_j = E_j S\psi_j \qquad (2.5)$$

Here ψ_j is a column vector, whereas $H_{mm'} = \langle \Phi_m | H | \Phi_{m'} \rangle$ and $S_{mm'} = \langle \Phi_m | \Phi_{m'} \rangle$ are the transfer and overlap intergal matrices [35]. By solving the general eigenvalue problem for the determinant matrix $\det(H - E_j S) = 0$ it is possible to obtain the band energies. The Hamiltonian in the eigenvalue equation for BLG can be obtained by taking into account $2p_z$ orbitals on all four atomic sites. This is given by :

$$H_{BLG} = \begin{pmatrix} \epsilon_{A_1} & -\gamma_0 f(k) & \gamma_4 f(k) & -\gamma_3 f^*(k) \\ -\gamma_0 f^*(k) & \epsilon_{B_1} & \gamma_1 & \gamma_4 f(k) \\ \gamma_4 f^*(k) & \gamma_1 & \epsilon_{A_2} & -\gamma_0 f(k) \\ -\gamma_3 f^*(k) & \gamma_4 f^*(k) & -\gamma_0 f^*(k) & \epsilon_{B_2} \end{pmatrix} \qquad (2.6)$$

where $f(k) = e^{ik_y a/\sqrt{3}} + 2e^{ik_y a/2\sqrt{3}} \cos(k_x a/2)$ describes the nearest neighbour hopping [35]. The diagonal elements in this matrix represent the on-site energies at four different atomic sites. The electron hopping can be described using four different parameters $\gamma_0 \approx 3$ eV, $\gamma_1 \approx 0.3$ eV, $\gamma_3 \approx 0.1$ eV, $\gamma_4 \approx 0.12$ eV which describe intralayer, on-site interlayer, interlayer B-A and interlayer A-A hopping respectively as labeled in figure 2.1 (b). Figure 2.1 (d) depicts the energy bands obtained from the eigenvalues E_j of equation 2.5.
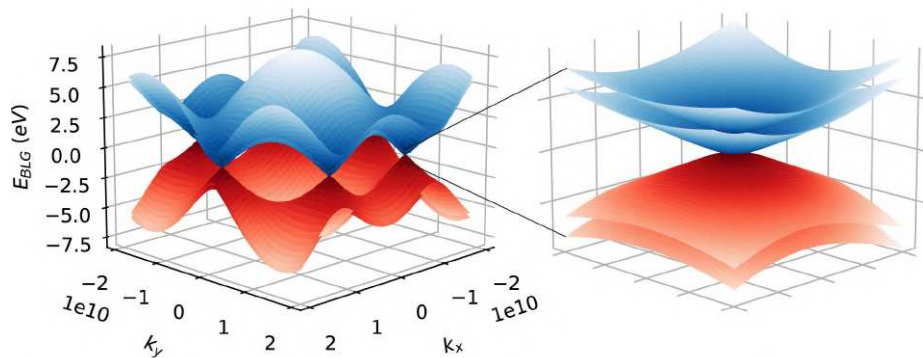

Figure 2.2: Band structure of BLG with a zoom-in of the symmetry point K (K') without an external displacement field applied. Figure is adapted from [36]

If no interlayer hopping ($\gamma_3 = \gamma_4 = 0$) is assumed the equation for four degenerate energy bands can be written as

$$E(k) = \pm\sqrt{\frac{\gamma_1^2}{2} + \frac{U^2}{4} + v_{\mathrm{F}}^2\hbar^2 k^2 \pm \sqrt{\frac{\gamma_1^4}{4} + v_{\mathrm{F}}^2\hbar^2 k^2(\gamma_1^2 + U^2)}}. \tag{2.7}$$

Here $v_{\mathrm{F}} = \frac{\sqrt{3}a}{2\hbar}\gamma_0$ is the fermi velocity and $U = \frac{1}{2}[(\epsilon_{A1} + \epsilon_{B1}) - (\epsilon_{A2} + \epsilon_{B2})]$ is the energy asymmetry between the two layers of BLG. In the limit of low momenta ($p = \hbar k \ll \gamma_1/2v_F$) equation 2.7 simplifies where the energy bands can be seen as parabolic dispersion curves.

$$E_{\mathrm{BLG}}(\mathbf{k}) = \pm\frac{\hbar^2 v_F^2 k^2}{\gamma_1} = \frac{p^2}{2m^*} \tag{2.8}$$

Under this limiting case, the electrons behave like massive quasiparticles in BLG with an effective mass of $m^* = \gamma_1/2v_F^2 \approx 0.03$ (m_e is the mass of an electron) [37]. In the absence of an external field, the energy bands of dimer sites are separated by the hopping parameter γ_1 while the energy bands of non-dimer sites intersect at zero energy making BLG a semi-metal. In the presence of a perpendicular displacement field (external), BLG shows the characteristic of a semiconductor where the inversion symmetry is broken leading to a potential difference between the two graphene layers [38]. This potential difference appears as a band gap between the conductance and valence band as shown in Fig 2.3 (b). The induced band gap can be expressed as [39]

$$E_{\mathrm{gap}} = \frac{U\gamma_1}{\sqrt{U^2 + \gamma_1^2}} \tag{2.9}$$

This explains the electrostatically tunable band gap of BLG which is a remarkably extraordinary feature that is of interest for this thesis[38, 40].
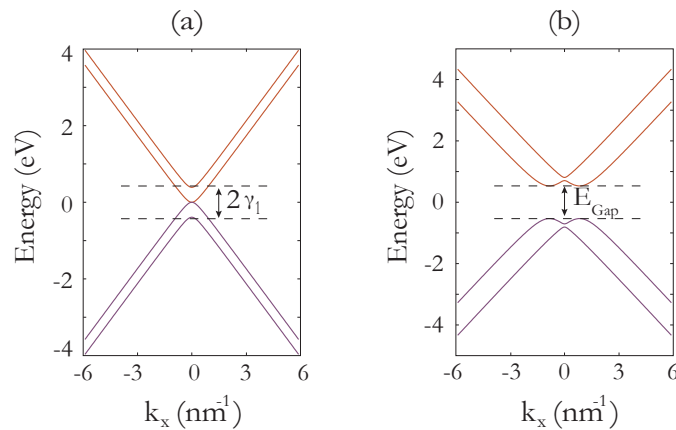

Figure 2.3: (a) Cut of the band structure along k_x near the K-point. When U=0 the non-dimer conduction and valence band intersect at zero energy. (b) In the presence of a perpendicular displacement field, the appearance of a band gap is shown (U $\neq$ 0). The figure is adapted from [41]

2.2 Fundamentals of Quantum Dots

Electrons are zero-dimensional particles that are subject to electrostatic confinement in all three dimensions in a QD. When these charge carriers are confined in the length scales that are smaller than the fermi wavelength, their energy spectrum can be described by discrete energy states [42, 43]. This is referred to as the level quantization. The level spacing between the discrete states of energies is of the order of 5-10 meV [44, 45]. One more interesting property of a QD is the coulombic repulsion between the electrons in a QD. The amount of electrostatic energy required to add an electron with charge e to a QD is called the charging energy E_c and is the order of ≈ 5 meV [44, 45]. This is termed as Coulomb charging. Two of these interesting properties of QD namely Coulomb charging and level quantization enable QDs to become hosts of single electrons. The Hamiltonian for describing such a many-particle system consists of two terms. The first term describes the sum of all single non-interacting particles and the second describes all possible coulomb interactions between these particles.

$$H_N = \sum_{n=1}^{N} h(\mathbf{r}_n) + \sum_{n=1}^{N} \sum_{m=1}^{n-1} V(\mathbf{r}_m, \mathbf{r}_n) \tag{2.10}$$

There are different approximations to solve this many-particle Hamiltonian like the constant-interaction model, the Hartree-Fock model, and the capacitance model. Here, the description will be made using the simple capacitance model from the reference [45].

Capacitance Model

In this model, QDs are considered as metallic islands that are capacitively coupled to the source (S) and drain (D) reservoirs. To understand the capacitance model the electrochemical potential for a QD ($\mu(N)$) needs to be defined. This quantity is a measure of the potential energy associated with the transfer of charge into or out of the quantum dot. The capacitive coupling helps in tuning the electrochemical potential of the QD. From the equation 2.10 the non-interacting term corresponds to quantum mechanical single particle energy $\epsilon_n^{(0)}$ whereas, the second term corresponding to the interactions is described using capacitance matrix $C_{i,j}$. The charges on the metallic islands and the gate electrodes are then given by

$$Q_i = \sum_{j=0}^{n} C_{ij} V_j + Q_i^{(0)} \tag{2.11}$$

Here, $i = 0$ represents the QD, and $i = 1, 2, ...n$ describes the surrounding gates. $Q_i^{(0)}$ denotes the charges in the absence of an applied potential V_j .
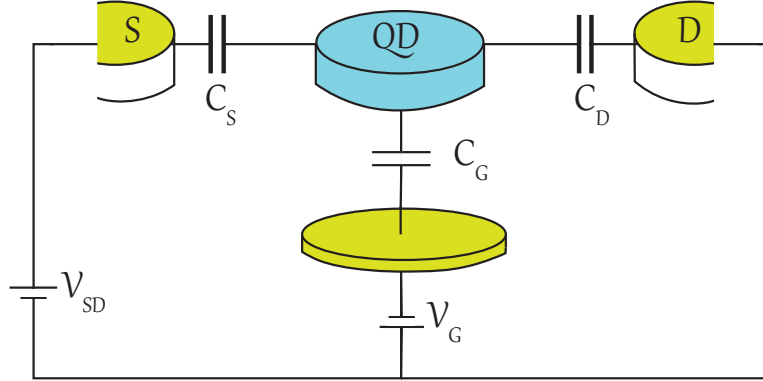
Figure 2.4: Schematic for Capacitor Model for QDs. The QD is coupled to the source, drain, and gate electrodes via tunnel barriers [46].

Equation 2.11 can be used to obtain the potential on the QD i.e. $V_0(Q_0)$

$$V_0(Q_0) = \frac{Q_0 - Q_0^0}{C_\Sigma} - \sum_{j=1}^{n} \frac{C_{0j}}{C_\Sigma} V_j \,, \tag{2.12}$$

Here, the total capacitance of the QD is C_Σ. The addition of 'N' number of electrons to a QD leads to an increase in the coulomb energy of QD. This electrostatic coulomb energy is given by

$$E_{\text{el.static}}(N) = \int_{Q_0^{(0)}}^{Q_0^{(0)}+|e|N} V_0(Q_0)dQ_0 = \frac{e^2 N^2}{2C_\Sigma} + |e|N \sum_{j=1}^{n} \frac{C_{0j}}{C_\Sigma} V_j \tag{2.13}$$

The total energy for the QD then consists of both single-particle energies and electrostatic coulomb energies. This can be written as

$$E(N) = \sum_{n=1}^{N} \epsilon_n^{(0)} + \frac{e^2 N^2}{2C_\Sigma} + |e|N \sum_{j=1}^{n} \frac{C_{0j}}{C_\Sigma}(V_j - V_j^{(0)}) \tag{2.14}$$

The first term here represents the sum of all single-particle energies. Using this equation it is possible to get a mathematical expression for the electrochemical potential of a QD. Here, it is expressed as the difference between the total energies of a QD with N+1 and N electrons.

$$\mu_N = E(N+1) - E(N) = \epsilon_{N+1}^{(0)} + \underbrace{\frac{e^2}{C_\Sigma}}_{E_C}(N+1/2) + |e| \sum_{j=1}^{n} \underbrace{\frac{C_{0j}}{C_\Sigma}}_{\alpha_i} V_j \tag{2.15}$$

Here, $\alpha_i = C_{0i}/C_\Sigma$ represents the lever arm. This gives a direct indication of the strength

of capacitive coupling/efficiency for each gate. The term $e^2/C_{\sum}$ is the charging energy of the QD which indicates the amount of electrostatic energy necessary to add an electron with charge 'e' to the QD whereas the amount of energy required to add additional electrons to a QD with 'N' electrons is called the addition energy. This can be expressed as the difference between the electrochemical potential of a QD

$$E_{add} = \mu_{N+1} - \mu_N = e^2/C_{\sum} + \epsilon_N^{(0)} - \epsilon_{N-1}^{(0)} \qquad (2.16)$$

When μ(N)=0 the energy required to add $(N+1)^{th}$ electron to a QD with N electrons is zero. This is referred to as the state of charge degeneracy.

In the following subsection, the electronic transport through QDs will be discussed.

Ground state transport through single quantum dots

To understand tunneling transport through the QD it is essential to assume that the direct tunneling of electrons between source and drain reservoirs is absent. The current flow from source to drain can happen only if the electrochemical potential for the QD lies between the electrochemical potentials of source and drain i.e. $\mu_{(S)} > \mu_{(N)} > \mu_{(D)}$ (in accordance with the bias V_{SD} in figure 2.4). When this condition remains unsatisfied the flow of current is strongly suppressed leading to the formation of diamond-shaped structures. These are referred to as Coulomb diamonds and the phenomenon of current being blocked in these regions is called Coulomb blockade. Tunneling transport is possible in the green-colored regions (see figure 2.5 (a)) whereas the number of electrons in the QD remains constant within the diamond. The two parameters that are used for investigating transport are the gate voltage V_G and potential across source-drain V_{SD} which can also be termed as the bias window. The regime for coulomb blockade is $\mu_{(S)} = \mu_{(D)} > \mu_{(N)}$. In this regime, an electron can tunnel into the QD from the source lead but cannot tunnel out from the QD into the drain electrode (see figure 2.5 b(1)). For a small bias window electron transport occurs if the potential for QD aligns with that of source and drain (see figure 2.5 b(2)). This is referred to as the linear transport regime ($\mu_{(S)} = \mu_{(N)} = \mu_{(D)}$) [47]. The current is because of the (N+1)th electron entering the QD from the source lead consequently hopping into the drain lead. For a finite bias window ($\mu_{(S)} = \mu_{(N+1)} > \mu_{(N)} = \mu_{(D)}$) there are two QD states accessible for an electron to occupy (figure 2.5 see b(3)). In this scenario, the coulomb resonances are broadened. Figure 2.5 (c) shows the coulomb resonances as a function of applied gate voltage. The positions (5) and (6) on the coulomb diamonds can be explained on similar lines. In the case of positions (7) and (8) the voltage of the drain electrode is positively biased with respect to the source electrode while position (4) will be explained when excited state transitions for a QD are considered. In the scope of

this thesis, it is essential to know how to estimate the lever arms of a coulomb diamond from the bias spectroscopy measurements in order to determine the strength of capacitive coupling offered by the surrounding gates. The width of coulomb diamonds represents the amount of energy required to add an electron given by $E_{add} = \alpha e\Delta V_G$ and the height of the diamond from the gate axis also corresponds to the addition energy i.e. $E_{add} = e\Delta V_{SD}$. Using these two equations the lever arm is estimated to be :

$$\alpha = \frac{\Delta V_{SD}}{\Delta V_G} \qquad (2.17)$$

Electron transport through a QD via GS transition was understood although the transport processes can also occur via excited state transitions which will be discussed in the following subsection.

Excited state transport through single quantum dots

When a QD is occupied with a fixed number of electrons the total energy of the QD is minimized to a state which is referred to as the Ground State (GS). Higher energy states are referred to as Excited States (ES). In the linear transport regime, the electron transport through QD occurs via GS transitions. Increasing the voltage bias can lead to the tunneling of electrons via ESs [45]. Figure 2.5 (d) displays the possible transitions for a QD in an energy spectrum where the QD can be occupied by N or N+1 electrons. The GS transition from N to N+1 state is shown in red in the figure 2.5 (a). This corresponds to the charging line outlining the coulomb diamond. A transition shown with yellow color in figure 2.5 (d) corresponds to a transition from GS of N state to the first excited state ES_1 of N+1 state. These transitions (positive transitions) require more energy and lie on the right side of GS transitions (shown in yellow and green). The transition between ES of N and GS of N+1 state requires less energy (negative transitions) as compared to GS transition in linear transport regime and hence they lie on the left side of GS transitions (shown in orange and violet). When these negative and positive transitions are available the tunneling current across QD increases because electron transport in a QD can occur via GS as well as ES transitions. Figure 2.5 (e) shows a line cut at fixed V_{SD} and increasing gate voltages V_G, which depicts the step-wise increase in the current when moving from GS to ES as there are additional transitions available in the bias window. Figure 2.5 (f) shows a line cut at fixed V_G and increasing source-drain voltages V_{SD}, which depicts similar behavior due to ES transitions. At the cross-over point for these line cuts, i.e. position 4 in the coulomb diamond, transport is possible from the GS of N to GS or higher ES of N+1 state (see figure 2.5 b(4)).

The following subsection is dedicated to discussing single-particle states in BLG.

Single particle states in bilayer quantum dots

A confinement potential of a quantum dot (QD) refers to the energy barrier that confines the motion of electrons or other charge carriers within the dot's spatial boundaries. This confinement potential leads to the discrete energy states whose solutions are termed as the orbital states. Each orbital state can be occupied by four electrons because of the two valley degrees of freedom and two spin degrees of freedom. Pauli's exclusion principle forbids the occupation of more than one electron with the same spin in a given energy state [48]. For a given orbital four electrons need to be filled before filling up the higher state orbitals. This sequence of electron occupation is called the shell-filling sequence. In the absence of a magnetic field, the wavefunction for these four electrons occupying four states of degenerate energies is given by [39]

$$\Psi_{K\uparrow}(\mathbf{r}) \qquad \Psi_{K'\uparrow}(\mathbf{r}) \qquad \Psi_{K\downarrow}(\mathbf{r}) \qquad \Psi_{K'\downarrow}(\mathbf{r}) \tag{2.18}$$
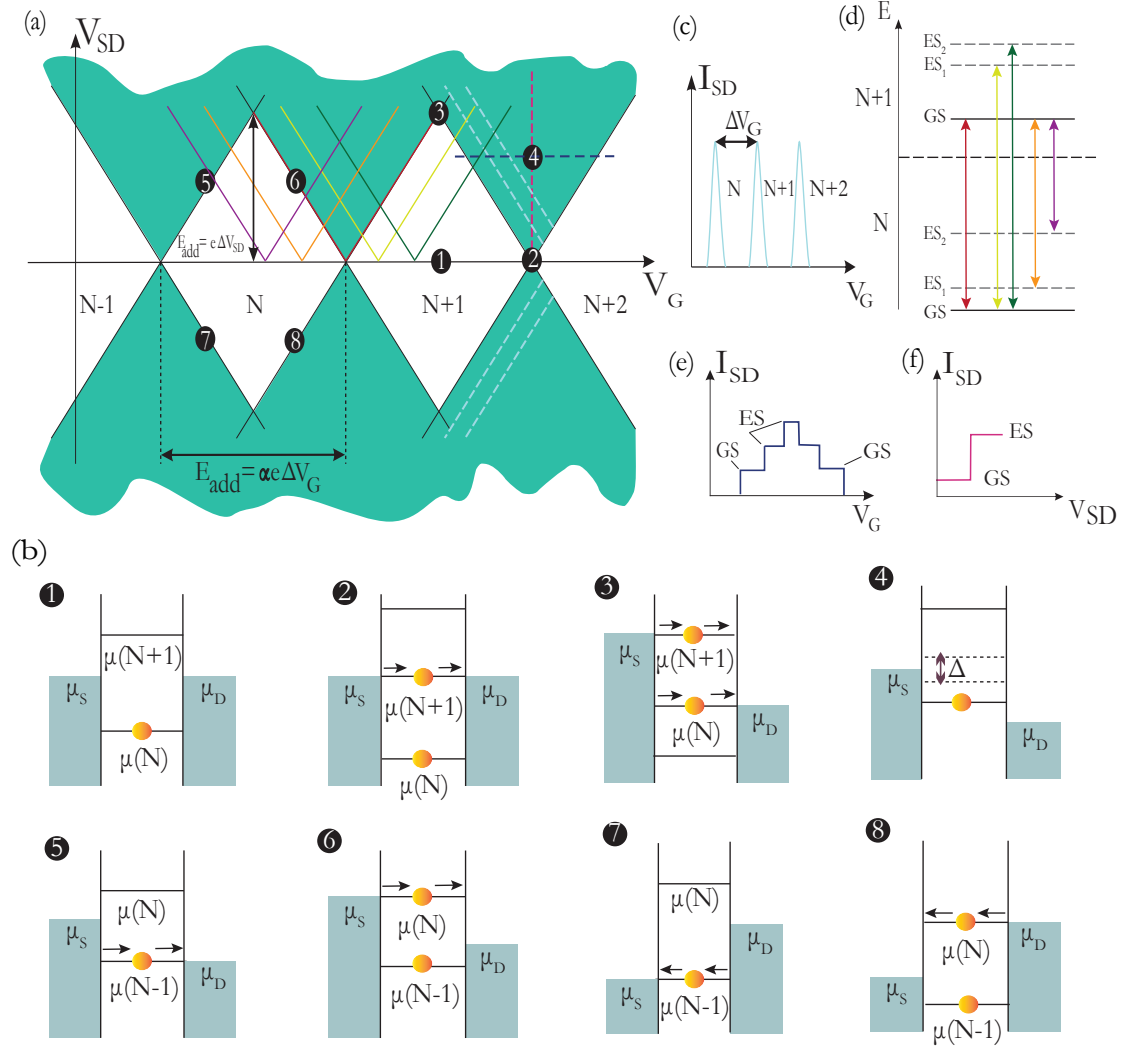
Figure 2.5: (a) Bias spectroscopy of a QD showing the formation of Coulomb diamonds. Tunneling transport occurs in the green region whereas the number of electrons in the QD remains constant inside the diamond. (b) Eight different regimes of transport in a QD with the chemical potential of the source and drain reservoirs in blue. (7) and (8) depict cases when the source voltage is negatively biased with respect to the drain. In (4) the Δ refers to orbital excited state energies which can be estimated from the Coulomb diamonds(c) Coulomb resonances as a function of gate voltage. (d) Schematic representation for the N and N+1 QD state with all possible transitions in different colors also depicted in the bias spectroscopy. (e) Line cut at fixed voltage bias depicting stepwise increase or decrease in conductance depending on positive or negative transitions. (f) Line cut at fixed finger gate voltage with a step increase in current from GS to an ES. The figure is adapted from two sources along with a few modifications [41, 49]

2.3 Superconductor-Semiconductor Quantum Dots

To establish a theoretical framework to understand the working of the devices built in the scope of this thesis, it is essential to begin with the basics of superconductivity and proximity effects.

Superconductivity and Proximity Effects

Superconductivity was observed for the first time during an experiment conducted by Heike Onnes in the year 1911 [50]. In this experiment, the electrical resistance of a mercury wire in seven U-shaped capillaries arranged in series was found to vanish suddenly at a temperature of 4.73K. However, the phenomenon was not recognized until Bardeen-Cooper-Schrieffer (BCS) laid the foundations of superconductivity in 1957 for which they were awarded the Nobel Prize in physics in the year 1972 [51, 50]. The assumption that lays the foundation for BCS theory states that there exists some attractive force between electrons (fermions) that has the potential to overcome coulombic repulsion leading to the formation of bound electrons called cooper pairs (bosonic pairs). These pairs of electrons have opposite wave vectors and spins (k↑, -k↓). This pairing is because of the weak electron-phonon coupling or the Fröhlich interaction [52]. But how do two negatively charged particles form a pair? There are two major forces in a metal that play a role in the context of cooper pair formation i.e. coulombic repulsion between electrons and weak electron-phonon coupling. When an electron moves through the metal it attracts the positively charged nuclei creating slight distortions that lead to lattice vibrations. These can be described as waves of lattice vibrations called phonons (see figure 2.6 (a)). When a material is cooled down to a lower temperature the thermal agitation is reduced significantly and the phonon waves can no longer break over short distances. This leads to the attractive force between electron and phonon becoming greater than the coulombic repulsion between electrons as the material reaches its critical temperature T_c [53] (see figure 2.6 (b)). Eventually, the material transitions from a normal conductor to a superconductor at T_c with nearly zero electrical resistance. For this thesis, the focus lies on BCS superconductors (conventional) mainly niobium and aluminum with a critical temperature of 9.25 K and 1.2 K respectively [54].

The behavior of Cooper pairs can be described with the help of a macroscopic quantum wavefunction. This wavefunction extends over the entire material and represents a coherent state of the paired electrons given by $\psi = \psi_0 e^{i\theta}$ with ψ_0 the amplitude and θ the phase [17]. The amount of energy required for two electrons to form a Cooper pair can be indicated by the size of the superconducting energy gap (Δ). This energy gap is a region

of suppressed density of states (DOS) around the fermi energy see figure 2.7 (a).
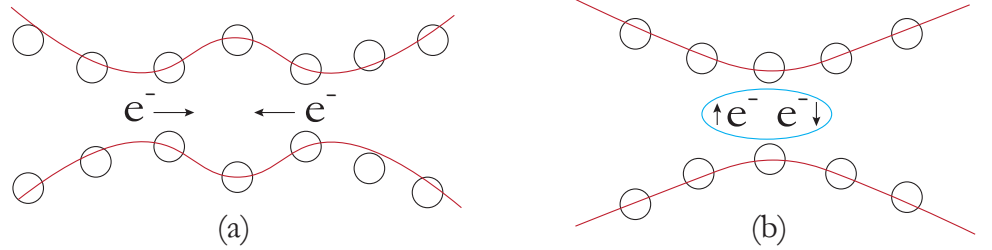

Figure 2.6: (a) Moving electrons creating lattice distortion leading to the formation of phonon waves (in red) (b) Electron-phonon attraction becomes greater than electron-electron repulsion leading to the formation of a cooper pair. Figure is adapted and reconstructed from [55]

BCS theory provides the relation between Δ and T_c : Δ(T=0) = 1.764 $k_b T_c$ [56]. In this energy gap, there are no available single-particle energy states for electrons to occupy. This is a consequence of the paired electrons collectively occupying the lowest energy state, often referred to as the 'condensate' state. Because the paired electrons have already occupied the lowest available energy states, there are no individual energy states left within the gap for single electrons to occupy. The absence of quasiparticle energy states within the gap prevents the usual scattering processes that leads to electrical resistance in non-superconducting materials, thus giving rise to the phenomenon of zero electrical resistance in superconductors [57]. The superconductors can be classified based on the relative angular momentum 'l' of Cooper pairs where l = 0 is described by an s-wave superconductor and l = 1,2,3 are p-wave, d-wave, and f-wave superconductors respectively. These can be characterized by odd/even parities and spin. An s-wave and d-wave superconductor has even parity and are spin-singlet superconductors while the other two are odd parity spin-triplets [58]. Most naturally occurring superconductors are spin-singlets with cooper pairs consisting of electrons with opposite spin [59]. Traces of triplet superconductivity (cooper pairs with parallel spins) have been observed recently in InSb nanowires coupled to aluminum [60]. It is still an unresolved mystery whether BLG QDs coupled to aluminum can help engineer equal spin pairing. However, if triplet superconductivity is observed it will become a great tool for realizing kitaev chains in a sequence of QDs [61].

In the case of an s-wave BCS superconductor, a superconducting coherence length can be defined as a measure of the distance between the electrons in a cooper pair [62]. Beyond this length, the superconducting properties break down due to reduced electron-phonon interaction, and the material transitions to a non-superconducting state.

It is given by [17]:

$$\xi_{BCS} = \frac{\hbar v_f}{\pi \Delta} \qquad (2.19)$$

where $\hbar$ is the reduced Planck constant, v_f is the Fermi velocity, and Δ is the superconducting energy gap. The coherence length plays an important role in fabricating quantum devices because it provides a limit to the physical dimensions of a superconductor in play. The ratio between coherence length and London penetration depth (λ) helps determine if a given material is a type 1 ($0 < \lambda/\xi < 1/\sqrt{2}$) superconductor or type 2 ($\lambda/\xi > 1/\sqrt{2}$) [63]. London penetration depth is referred to as the distance up to which the magnetic field can penetrate inside a superconductor and becomes equal to 1/e times the magnetic field at the surface [64]. In type 1 superconductors like aluminum the superconductivity breaks abruptly after the strength of the applied magnetic field crosses a certain critical threshold. In contrast, type 2 superconductors have two critical thresholds [63]. Recent studies have recognized niobium as a type 1 superconductor although the presence of disorders, impurities, and strains pushes it to become a type 2 superconductor [65].

The important question is what would happen if a normal conductor were in proximity to a superconductor [66, 67, 68]. The superconducting proximity effects come into play in addition to different types of electron transport processes occurring at the N/S interface. These include Local Andreev Reflection (AR), Crossed Andreev Reflection (CAR), and Elastic Co-tunneling (ECT) as can be seen in figure 2.7 (b). The Proximity effect leads to one material acquiring the properties of another material and vice-versa when they are in close contact [69]. Studies have shown that certain properties of semiconductor systems like spin-orbit coupling and g factor renormalize under the influence of proximitized metals requiring the presence of a higher magnetic field to open and close the superconducting gap [70]. But aluminum offers an advantage as it has shown zero field superconducting gap opening (200 to 300 μeV) [70]. These effects have become an engineering tool to study new properties that never co-existed in any material for practical applications [71]. Cooper Pair Splitter is one such device studied extensively to identify and manipulate entangled spin pairs for applications in quantum information processing [72]. Before studying an N-QD-S-QD-N junction it is necessary to understand transport in an NSN junction.
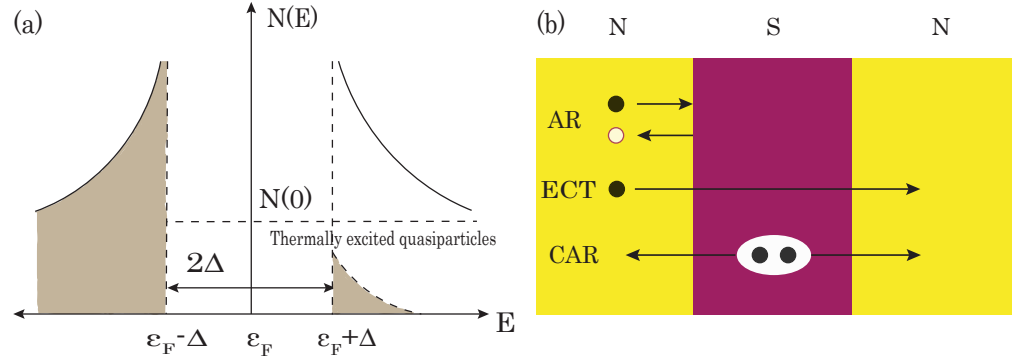
Figure 2.7: (a) Number density N(E) vs Energy (E) for a BCS superconductor at T>0. At temperatures T> T_c the phenomenon of superconductivity breaks down. Shaded regions represent the existence of single quasiparticle excitations below fermi energy and above fermi energy where they are in a state of thermal excitation. The region represented by 2Δ is the superconducting gap at temperatures below T_c where cooper pairs exist. A minimum energy of 2Δ energy is required to break these cooper pairs (b) Electron Transport Processes at an NSN junction showing andreev reflection (AR), elastic co-tunneling (ECT), and cross andreev reflection (CAR). In AR an electron is reflected as a hole while in CAR a cooper pair is split from the superconductor into the two normal regions. For ECT an electron in the first normal region tunnels into the other normal region. (a) is adapted from [73] with modifications. (b) is adapted from [60]

2.3.1 NSN Junction

Quantum Transport in a Normal-Superconductor-Normal (NSN) junction can be categorized into Soft gap (above-gap) [74] and Hard superconducting gap (sub-gap) [75]. In the former case, single-quasiparticle excitations exist in superconductors and the current flow is very similar to a normal metal with DOS being suppressed for a single energy value. For an NS junction if the voltage bias V applied across them satisfies this condition $|eV| > \Delta$ then the electrons have sufficient energy to tunnel through the interface. Many superconductor semiconductor systems show a soft gap due to intrinsic material disorder and inhomogeneous interfaces [76]. Theoretical models on superconductor-semiconductor nanowires have predicted the effects of non-magnetic disorders, and dissipative breaking of Cooper pairs as possible reasons leading to a soft gap [77]. However, for non-topological materials at zero magnetic fields, the gap is large or hardest [77]. To create a hard gap it is essential to have a homogenous and barrier-free [78] superconductor-semiconductor interface [79]. Hybrid devices with aluminum coupled to Ge-Si nanowires have achieved this by annealing devices at a temperature of 180° leading to the interdiffusion of aluminum in the germanium nanowire [79].

The interest here lies in studying transport for superconductors where single quasiparticle excitation is absent. This shows zero conductance for $|eV| < \Delta$ as electron and hole tunneling is forbidden. Previous studies on tunnel spectroscopic measurements of hard-gapped superconductors have confirmed little or no conductance for low tunneling rate [79]. The coupling between superconductor-semiconductor junctions is strongly affected by the tunneling rates of electrons which in turn depends on the applied gate voltages [80]. Change in superconductor-semiconductor coupling can help induce a transition from the above gap state to subgap states thus indirectly affecting the size of the superconducting energy gap [80]. A hard superconducting gap of 1 meV has been observed in PbTe nanowires where DOS is suppressed over an extended range of energy [81]. Although electrons can't tunnel the junction in a hard gap, a family of Andreev reflection processes can occur at the interface, which converts the electron/hole current flow in normal metal to supercurrent mediated by cooper pairs in the superconductor. It is necessary to highlight here that low-temperature transport is assumed ($k_B T \ll \Delta$) to describe the conventional BCS superconductor in its ground state. Understanding andreev processes in detail is the aim of the next section. To do that the most favored way is to further divide sections of subgap superconducting transport into cases where the conductance is local and non-local. The first question that needs to be answered is the difference between local and non-local conductances. Local conductance can be defined as the differential current measured at a junction in response to the voltage at the same junction whereas non-local conductance is current at one junction induced by the differential voltage applied across the other junction.
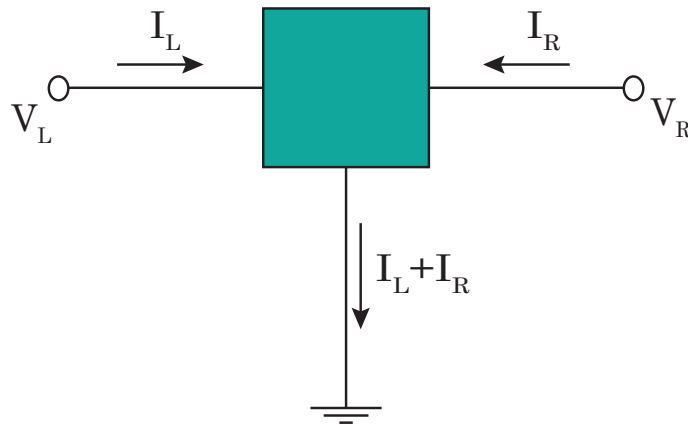

Figure 2.8: Three terminal circuit. Figure adapted from [60]

This can be expressed in terms of a conductance matrix :

$$G = \begin{pmatrix} G_{LL} & G_{LR} \\ G_{RL} & G_{RR} \end{pmatrix} \tag{2.20}$$

where G_{LL} = dI$_L$/dV$_L$, G_{LR} = dI$_L$/dV$_R$, G_{RR} = dI$_R$/dV$_R$, G_{RL} = dI$_R$/dV$_L$. The first and third terms describe local conductance while the rest two describe non-local conductance. In the coming section, the processes at the NS interface and NSN interface are discussed wherein few of them show local signals like andreev reflection while the other ones like cooper pair splitting exhibit non-local signals. Recent evidence has shown that non-local conductances in a cooper pair splitter can occur via cooper pair splitting as well as Shiba-assisted local pair tunneling (SPT) [10]. The following discussion on local and non-local conductances is based mainly on descriptions from [60, 17].

Local Conductance

Consider an electron with an energy ($|eV| < \Delta$) that is slightly higher than the Fermi level approaching the interface between normal (N) and superconducting (S) region under the influence of an applied bias voltage V. Because of the absence of single electron states in the superconductor, the electron would not be able to transmit. However, the electron has a small probability of reflecting from the interface. The reason for the probability being small is because of the absence of a barrier to absorb the momentum difference between the incident and the reflected electron. There is one more scenario when the electron reflects as a hole. In this scenario, the formation of a cooper pair happens in the superconductor wherein another electron is absorbed from the fermi sea of the normal conductor. The electronic vacancy created in the fermi sea can be interpreted as the creation of a hole carrying a positive charge. For the Cooper pair to form, the wave vector of the incident electron and the one absorbed from the Fermi sea should be opposite. However, it is known that wave vector and group velocity for a hole are in different directions hence the hole takes the same path as an incident electron in the reverse direction. This process is therefore called retroreflection. A total charge of 2e is transferred across the interface where it becomes the supercurrent carried by the cooper pair. The excess momentum because of the energy difference between the incident electron and the retro-reflected hole is taken up by the Cooper pair k_{Cooper} = k_e - k_h. The conduction at the NS interface is given by [60, 17]

$$G_{N-S} = \frac{4e^2}{h} \frac{T^2}{(2-T)^2} = \frac{e^2}{h}[1 - R_{e,e}(E) + T_{e,h}(E)] \tag{2.21}$$

where T is given by transmission probability. Whereas $R_{e,e}$ and $T_{e,h}$ are the reflection

probability of an electron incident on the NS interface back into the N lead and the other is the retroreflection of an electron as a hole which leads to 2e current in the superconductor, hence the positive/negative signs. Comparing this with the Landauer expression for the normal interface, where $G_{N-N} = 2e^2T/h$, and plugging the value for transmission probability as 1, it can be estimated that $G_{N-S} = 2G_{N-N}$. This confirms that the conductance for an NS interface is consistent with the charge transfer of 2e at the interface. However, the chances of Andreev reflection (AR) occurring are less and there is a need for a transparent barrier with high transmission probability. This is because the transmission probability for an electron is T and Andreev reflection goes by T^2 (see 2.21) which would be low for interfaces with low transmission probabilities [17].
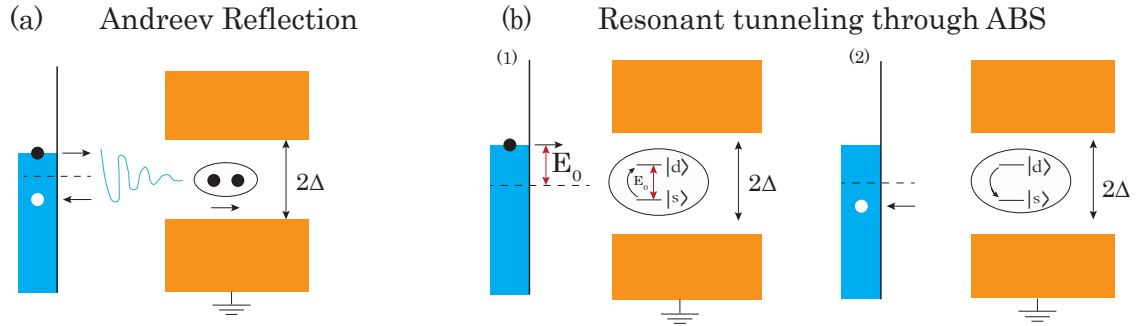

Figure 2.9: Orange region represents the superconductor whereas blue one is the normal junction (a) Retroreflection of a hole creating a cooper pair inside the superconductor (b) Andreev reflection occurring via two-step ABS process consisting of even ground state and odd excited state. The figure is adapted from [60]

Fabrication of a transparent NS interface is very difficult and several other factors like material mismatch, thermal instabilities, fabrication residues, and Schotkky barriers affect the transport processes [82, 83]. So the next crucial question arises to understand if some other types of Andreev processes can occur for less transparent interfaces. There is a process called Resonant Andreev tunneling which occurs with the formation of Andreev-bound states (ABS). This is a two-step quantum transport process. But what are these ABS? These can be described as discrete states of particle-hole symmetries formed in a semiconductor-superconductor system. ABS can exist either in a ground state or higher excitation states. Consider the ABS has two states. One is an even ground state $|s\rangle$ and the other is an odd excited state $|d\rangle$. The parities of these states differ by one and they are separated with an energy E_0. An electron with energy E_0 from the normal lead (N) induces resonant transitions of ABS. When in an even ground state (singlet) the ABS absorbs the incident electron at the interface and transitions to the odd excited (doublet).

As this is an excited state the electron transitions back to a ground state. For this process to occur another electron from the fermi sea of normal lead is absorbed thus relaxing back to the even ground state. Absorbing this electron has led to the formation of a hole. This process explains the mechanism of an ABS relaxing to the ground state by dissipating additional energy with the capture of another electron. With this resonant process, the conductance peaks can be observed at bias voltages which are equal to the transition energies E_0 between odd and even states of the ABS [60]. In the case of less transparent barriers, andreev reflection occurs via ABS leading to the transmission of 2e supercurrent in the superconductor. Tunneling spectroscopy measurements can reveal whether AR occurred via ABS or not thus acting as a tool to identify the transparency of the N/S interface [60]. The discrete ABS states are visible as particle-hole symmetries in the superconductor which also extends in the hybrid semiconducting segment and the local conductance measurements reveal the subgap resonances at low magnetic fields [84].

Non-Local Conductance

At an NSN junction, a whole range of dynamic physics exists [66, 85]. In all the above sections the study was based on an N/S interface where the electrons/holes reflected to the original N lead. This can be extended to the case where the electron from the first Normal electrode leads to an electron/hole in the other N electrode via the superconductor. The transmission probabilities for an electron injected from the first N lead (i) leading to an electron or hole to the other N lead (j) can be denoted as T_{ij}^{ee} and T_{ij}^{he} respectively. The two processes lead to current flow in the opposite direction hence the conductance is given by [60].

$$G_{ij}(E) = \frac{e^2}{h}[T_{ij}^{he}(E) - T_{ij}^{ee}(E)] \tag{2.22}$$

Non-local conductance can be because of sequential tunneling through an ABS or via off-resonance transmission through virtual occupation of ABS states i.e. Cross Andreev Reflection (CAR) and Elastic Co-tunneling (ECT). Sequential tunneling can occur only when the injected particle has an energy of or above ABS excitation energy E_0. When there is not enough energy supplied from the lead for sequential tunneling to occur, the CAR and ECT processes occur by the virtual occupation of the higher energy states. The interest remains in studying the latter for this section. The wavefunction amplitudes of electrons and holes can be represented by position-dependent functions u and v. The excitation energy for an ABS from an even ground state to an odd excited state is E_0.
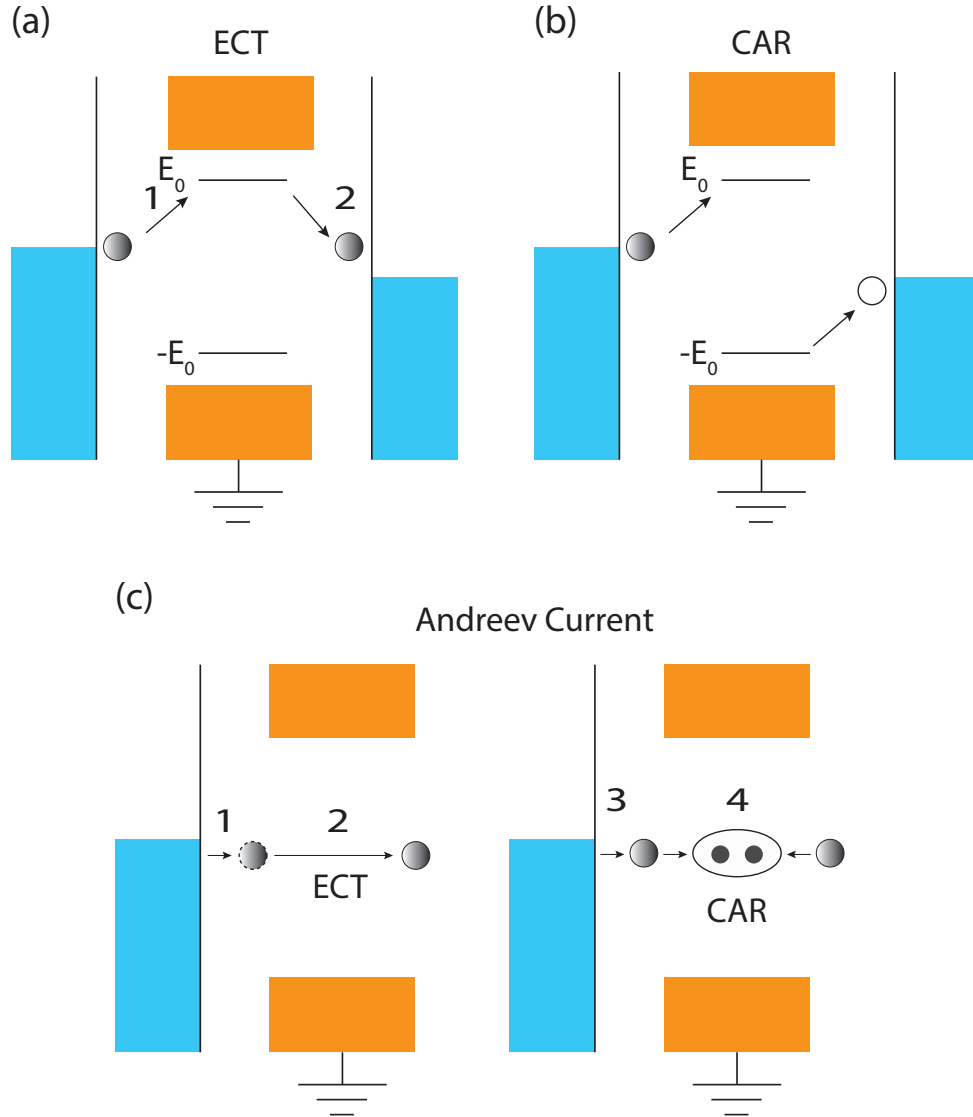
Figure 2.10: The orange region represents the grounded superconductor while the blue segment on its left and right side are the two normal leads (a) ECT process via virtual occupation of an ABS state (b) CAR process leading to the formation of a hole on the right normal lead and a cooper pair within the superconductor (c) Transport via ECT and CAR in a four-step cycle leading to an NS andreev current. Figure is adapted from [60]

The transition rates for the occurrence of ECT and CAR via ABS (see figure 2.10) can be written as [60]

$$W_{CAR} \propto \left| \frac{2uv}{E_0} \right|^2, \qquad W_{ECT} \propto \left| \frac{u^2 - v^2}{E_0} \right|^2, \qquad (2.23)$$

For both of these processes the energies of the incident and reflected electron/hole remain conserved and are less than the ABS excitation energies i.e. $E_i{=}E_f{<}E_0$. To understand this it is feasible to divide the description into three categories. Firstly, in the initial state where the ABS is in an even ground state (relaxed) with an electron approaching (with energy $E_i < E_0$) the N-S interface. Secondly, the intermediate state is where the ABS transitions to the odd excited state. Lastly, in the final state, the ABS relaxes back to the ground state. In the final state, ECT leads to the incident electron going into the right normal lead while for CAR a hole is formed. CAR can be visualized in two ways, one is the formation of one hole in each N lead while creating a cooper pair inside the superconductor whereas the other way involves visualizing the formation of one electron in the left normal lead and one electron in the right lead which are split from a single cooper pair. These electrons maintain entanglement even though they are separated in space. This process is called Cooper pair Splitting (CPS). In the case when E_0 is high, these electronic transitions are not possible because a large amount of energy is needed to excite an ABS. When u=v which is called the charge neutrality point (CNP), CAR is dominant and ECT is suppressed. Moving away from CNP it is predicted to see CAR decaying faster [86]. Previous studies have shown exponential decay of the CAR process when there is a large distance between the two normal leads because of which local transport processes like andreev reflection are more dominant than non-local processes [87]. To reduce these effects significantly introducing a quantum dot between the normal and superconducting lead can be advantageous because a QD imposes a condition of double electron occupation for a charge transfer of 2e via AR which requires high bias energies [88, 89] thus substantially reducing the chances of AR. One main problem that was still not addressed until recently was the ability of a QD to differentiate between CAR and ECT. Controlling the energy and charge of these ABS processes is possible using gate voltages which provide control knobs for studying these experiments separately as demonstrated in [86].

The following section describes the transport process for an N-QD-S-QD-N junction followed by a theoretical model and discussion on ECT/CAR for this hybrid system.
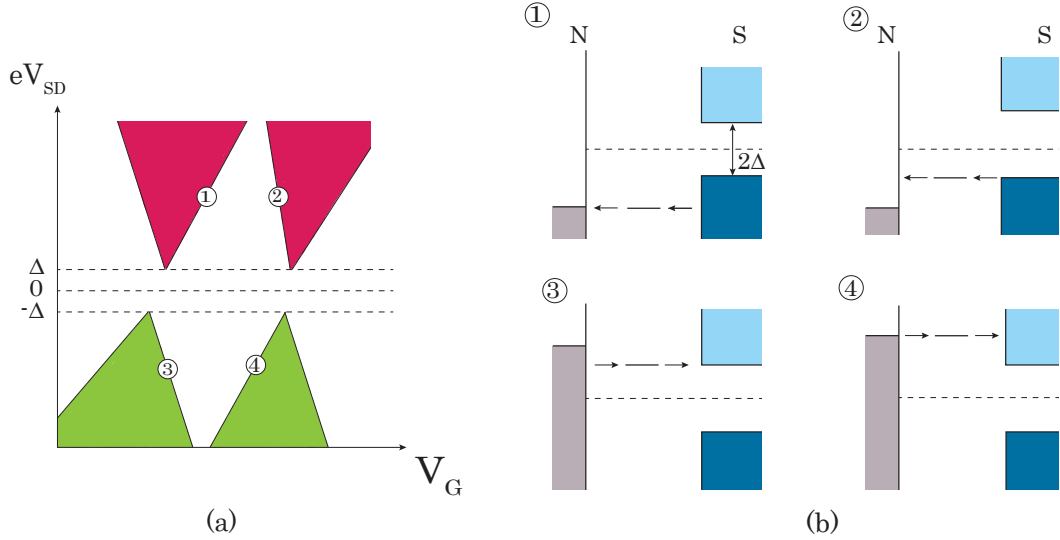
2.3.2 N-QD-S-QD-N Junction

Figure 2.11: (a) Coulomb diamonds for an N-QD-S junction showing the presence of superconducting gap which prevents tunneling of electrons across QDs (b) Depicts transport of electrons from S to N or N to S junction at different positions on the coulomb diamond. The figure is adapted from [60]

In an N-QD-S-QD-N junction, at least Δ energy is necessary for single electron transitions to occur even if the fermi energy of QD is aligned with the fermi levels of the superconductor. Thus the QD no longer behaves in the same way as explained with the capacitance model when proximitized to a superconductor. The reason is the presence of the superconducting energy gap Δ which prevents the direct tunneling of single electrons across the superconductor. The superconductor acts as an energy barrier that prohibits the entry of single quasiparticles unless an external bias voltage supplies sufficient energy (Δ). An energy of 2Δ will break up a pair and create two normal electrons.

The strength of coupling between QD and superconductor can be mainly of three types. The types of coupling are weak coupling ($\Gamma \ll \Delta$, E_{add}), strong coupling (Case 1 : $\Gamma \gg \Delta$, E_{add} or Case 2 : $E_{add} > \Gamma \gg \Delta$), and intermediate coupling ($\Gamma \approx \Delta \approx E_{add}$) [57]. Γ here represents tunnel broadening which can determined based on the transparency of the normal-superconductor interface. In the case where the superconductor is weakly coupled to the QD, there is a creation of a gap equal to $\pm\Delta$ where the current is forbidden [60] whereas, outside this gap, it is expected to observe Coulomb diamonds. In this regime, quasiparticle transport is possible for $|eV| > 2\Delta$ and processes like andreev

reflections are suppressed due to poor transparencies at the interface [17]. Exactly at $|eV| = 2\Delta$ conductance peaks can be observed because of the tunneling of electrons split from a cooper pair across the QDs [17]. In case 1 of a strongly coupled regime, a supercurrent can be observed whose magnitude is given by $I_s(n) = ne\Delta/\hbar$. Here 'n' is the number of parallel modes participating in superconducting transport which means the total number of independent conducting channels available for the flow of supercurrent. For case 2 the supercurrent is given by [17]

$$I_\text{C} = I_\text{C,MAX}(1)\left(1 - \sqrt{1 - T_\text{BW}}\right), \qquad T_\text{BW} = \frac{\Gamma}{(\mu(N)/h)^2 + \frac{1}{4}\Gamma^2}, \qquad (2.24)$$

Here, T_{BW} is the Breit-Wigner transmission probability [90]. Lastly, in the case of an intermediate coupling regime, there is a competition between single quasiparticle and superconducting transport via cooper pairs and the explanation is beyond the scope of this research.
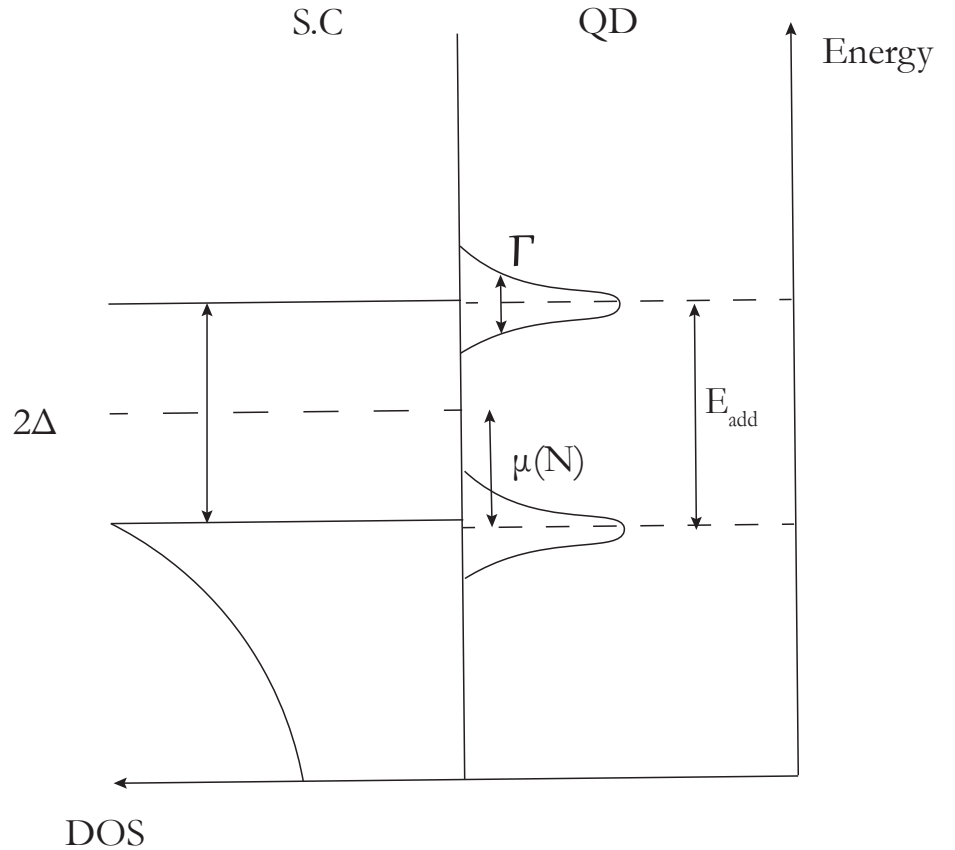

Figure 2.12: Energy Vs Density of State diagram for an SC-QD interface. The figure is adapted and remodified from [17]

After discussing the types of interactions at an SC-QD interface, the next subsection which is adapted from the theory chapter of [60] focuses on studying a model for an N-QD-S junction.

Model for proximitized QD

The model to describe a system consisting of a QD tunnel coupled to a superconductor is given by:

$$H_{sys} = H_{QD} + H_S + H_{tun} \tag{2.25}$$

Here, H_{QD} is the Hamiltonian for the single-level QD, H_S refers to the superconductor, and H_{tun} is the tunnel coupling term. The QD can be occupied by 0, 1, or 2 electrons which can be exchanged for creating or breaking cooper pairs in a superconductor. The Hamiltonian for the QD in this model is given by:

$$H_{QD} = \mu \left(n_\uparrow + n_\downarrow \right) + \frac{E_Z}{2} \left(n_\uparrow - n_\downarrow \right) + U n_\uparrow n_\downarrow \tag{2.26}$$

In the above equation, E_z represents a magnetic field in the z-direction which induces the splitting of electrons with up and down spin, while U is the charging energy and μ is the electrochemical potential of the QD. The Hamiltonian for superconductors can be explained with mean field BCS theory.

$$H_S = \sum_{\vec{k},\sigma} \varepsilon_k d_{\vec{k}\sigma}^\dagger d_{\vec{k}\sigma} + \sum_{\vec{k}} \Delta d_{\vec{k}\uparrow}^\dagger d_{-\vec{k}\downarrow}^\dagger + \text{h.c.}, \quad H_{tun} = \sum_{\vec{k},\sigma} t d_{\vec{k}\sigma}^\dagger c_\sigma + \text{h.c.} \tag{2.27}$$

Here, electron annihilation operator is $d_{\vec{k}\sigma}$ with momentum $\vec{k}$ and spin σ. The kinetic energy is given by ε_k. The superconducting order parameter Δ directly relates to the pairing interaction between electrons in a cooper whose magnitude is given by the strength of the interaction (here Δ is assumed to be greater than 0) while the phase describes the spatial structure of pairing [91]. The coupling of QD to the electrons in the superconductor is expressed with a tunneling amplitude term t. This model can be simplified to understand things more intuitively with two approximations. The first approximation is the zero bandwidth approximation (ZBW) where the superconducting quasiparticle continuum is replaced with one electron pair having a certain excitation energy. The second one is to consider Δ tending to infinity. The simplified Hamiltonian (in the superconducting atomic limit) then looks like

$$H_{atomic} = H_{QD} + \Gamma c_\uparrow^\dagger c_\downarrow^\dagger + \text{h.c.} \tag{2.28}$$

Where Γ describes the coupling strength. The discussion in the next subsection describes possible signatures for ECT, CAR, and the formation of ABS in an N-QD-S-QD-S junction.

ECT and CAR in an N-QD-S-QD-N junction

In an N-QD-S-QD-S junction, the process of CAR and ECT can occur via the virtual occupation of ABS states for less transparent interfaces. The currents induced by ECT and CAR through both these processes are given by [86] :

$$I_{ECT} = I_0 \left| \frac{u^2 - v^2}{E_{ABS}/\Gamma} \right|^2 , \qquad\qquad I_{CAR} = I_0 \left| \frac{2uv}{E_{ABS}/\Gamma} \right|^2 \qquad (2.29)$$

Here, I_0 is a proportionality constant ($e/\hbar$) that depends on the strength of coupling between ABS and QDs and also on the lifetime of QDs [86]. Tunnel broadening Γ can be determined by the transparency of the Superconductor-QD (SC-QD) interface [17]. The wavefunction amplitudes for electrons and holes are u,v as defined earlier. E_{ABS} refers to the difference between energies of singlet and doublet states of an ABS.
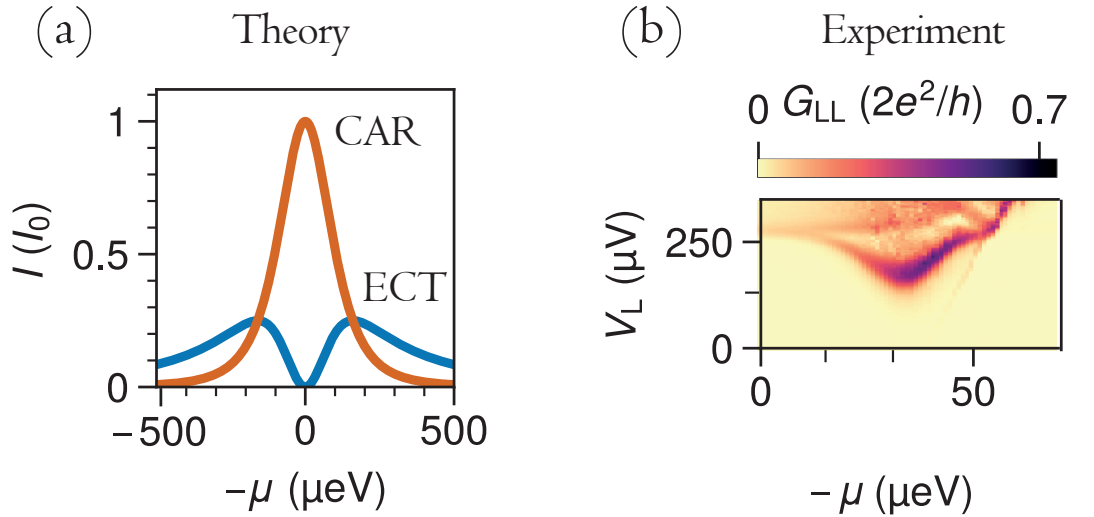
Figure 2.13: (a) Theoretical prediction for non-local conductance at an N-QD-S-QD-S junction as a function of the electrochemical potential of a QD (b) Local conductance across the hybrid segment where the bell-shaped ABS formation is depicted for an InSb nanowire coupled to aluminum. The figure is taken from [86].

Figure 2.13 (a) describes the possible signature of non-local conductances induced due to CAR and ECT as a function of the electrochemical potential of the QDs predicted with a

theoretical model in recent studies [86]. At $\mu = 0$ which is the charge neutrality point, CAR is the only dominant process suppressing the co-tunneling of electrons from a QD on the left side of a superconductor to the QD on the right. Measurements of local conductance as a function of gate voltage V_L applied to the normal junction and the electrochemical potential of QDs lead to the formation of the bell-shaped curves. Figure 2.13 (b) depicts this signature of an ABS featured in the hard superconducting regime of a superconductor for InSb nanowires coupled to aluminum [86]. It is expected to observe similar features of ABS with local conductance measurements. These bell-shaped curves can extend through the superconductor QD interface into the BLG channel.

Chapter 3

Experimental Methods

This chapter is divided into 3 sections. The first section states the sample layout for the devices followed by the details of the nanofabrication process and a measurement section explaining the experiments intended to be performed for these devices.

3.1   Sample Layout

The sample layout for the three device designs that are fabricated is shown in Fig 3.1. The device consists of BLG encapsulated by top hexagonal Boron Nitride (hBN) with thicknesses around 20-30 nm and bottom hBN with thicknesses around 25-40 nm placed on top of a graphite back gate (BG). The heterostructure is placed on a silicon substrate covered with 90 nm of silicon dioxide. The thickness of the top hBN used for fabrication is small as compared to the bottom hBN because the top hBN needs to be etched for creating source and drain contacts to the BLG. These contacts to the BLG should be avoided from getting in contact with the graphitic back gate as this leads to short circuits in the device. hBN serves as a dielectric layer between BLG and a graphite back gate (BG) with a dielectric constant of 3.4 [92] and a band gap of ($\approx$ 6 eV) [93] protecting BLG from extrinsic disorders arising from environmental contaminations due to the presence of atmospheric adsorbants [92, 94]. The lattice structure of hBN is very similar to BLG with a very small difference in lattice parameters ($\approx$ 1.8 %) [95] thus making it suitable for integration into graphene-based heterostructures with minimum strain and aiding the increase of charge carrier mobility in BLG [96, 92]. The use of graphite as a global back-gate helps achieve a cleaner band gap of around 120 meV for BLG-based van-der Waals heterostructures also allowing fine tuning of Fermi energies [38, 97].
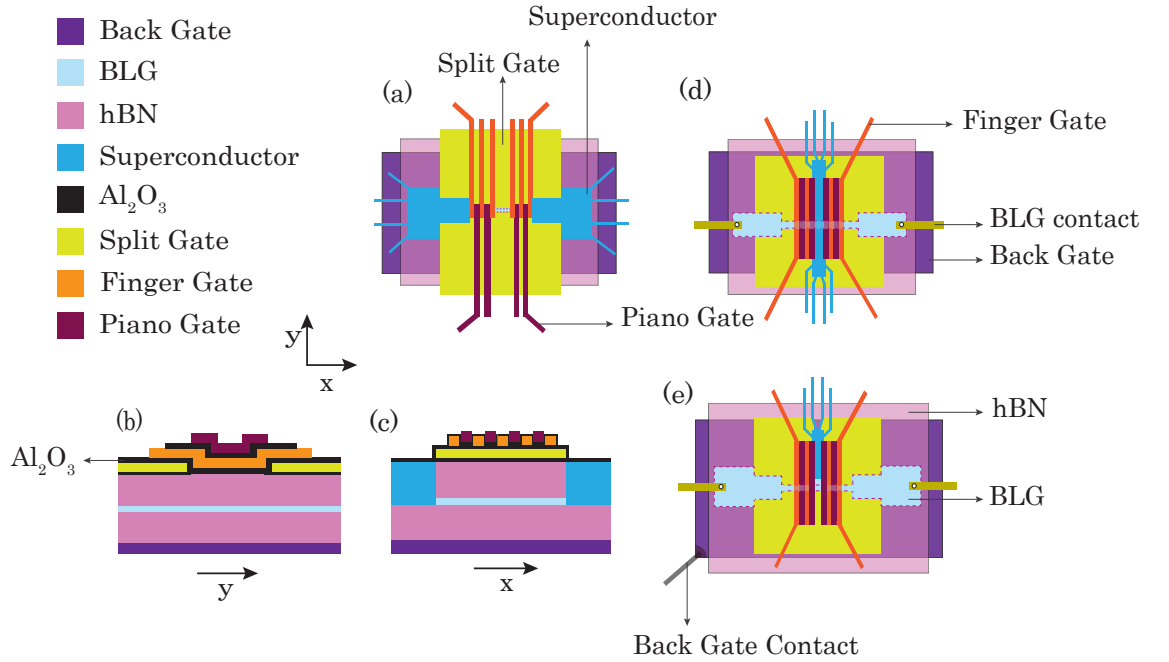
Figure 3.1: Schematic of the Superconductor QD device design. The heterostructure consists of a BLG flake that is encapsulated between hBN crystals and placed on top of a graphite back gate (BG). The Superconductor is metalized on top of the BLG. This superconductor is separated by a 15nm dielectric layer of Al_2O_3 separating it from the Cr/Au SG on top. Another layer of Al_2O_3 separates the SGs from the Cr/Au FGs and similarly for the PGs (a) Top view of Design 1 (b) View along the channel for Design 1 (c) View perpendicular to the channel for Design 1(d) Top view of Design 2 (e) Top view of Design 3

Several Cr/Au gates namely Split Gate (SG), Finger Gate (FG), and Piano Gate (PG) are needed to create a quantum dot which will be discussed ahead in this chapter. For devices (a) and (d), two SGs are created while for the third design (e), there are three SGs. These are made of a layer of Cr/Au (5nm/25nm) with a lateral separation of 100 nm for all three designs. Chromium here serves as a great adhesion layer for the gold contacts [98]. It also provides mechanical stability because of the formation of Cr-Au alloy that offers good electrical contact to nanomaterials [98]. The superconductor is 200 nm wide for all three designs although slight variations in this length ($\approx$ 20-30 nm) are done for experimentation purposes and also to vary the distances between two QDs that will be needed for studying cooper pair splitting. In the case of design (e), the superconductor does not cross the 1D channel in BLG (160 nm away from the lower split gate) as this design is made for splitting electrons from the cooper pair into QDs which also explains the requirement for three SGs. For design (d) the superconductor completely crosses the 1-D channel because the

processes of CAR and ECT are to be studied via the formation of ABS which also extends into the hybrid segment. For design (a) there are 2 superconducting leads on both sides of the 1D channel. The BLG is contacted on both sides of the channel to create ohmic point contacts (Source/Drain) and a separate contact to the graphite back gate is created. The width of PGs and FGs is 65 nm for all three device designs and the distance between two consecutive PGs or FGs is also 65 nm. The detailed steps involved in the fabrication process of these devices are explained in the following section.

3.2 Device Fabrication

The fabrication process starts with the micromechanical exfoliation of hBN and graphite crystals [99, 100]. These crystals are exfoliated on Si/SiO$_2$ wafers with the help of scotch tape. The silicon wafers are then examined with a flake database tool to identify clean and suitable flakes for building the heterostructure [101]. The next step involves creating stacks with the exfoliated flakes using the dry Van der Waals pick-up and transfer method [102]. For this purpose, a polydimethylsiloxane (PDMS)/polycarbonate (PC) stamp is created by melting a small segment of PC film on top of the PDMS and baking at 100°C for two minutes. This PDMS stamp is used to pick up top hBN, BLG, bottom hBN, and graphite in that order at 110-115 °C. Finally, this stack is placed in the central region on a marker chip by heating the stage of the transfer system to 170 °C. When in contact the temperature of the stage is increased to 180 °C to push the bubbles and contaminations between the layers of the stack. At higher temperatures, the PC film starts to melt and is transferred along with the stack on the marker chip. The marker chip is then cleaned using Chloroform (CHCl$_3$) solution for 20 to 30 minutes. If PC residues still exist it is preferable to keep the chips dissolved for a longer duration. The chips are then cleaned in IPA solution for another 1 minute to remove chloroform residues if any. In this 2D heterostructure, the position of BLG is not known as it is sandwiched between other layers. This is why the stack is characterized using Raman Spectroscopy to identify the BLG flake with its characteristic Raman spectrum. Figure 3.2 (c) shows the Raman G (f $\approx$ 1600 cm^{-1}) and 2D (f $\approx$ 2700 cm^{-1}) peak of graphite [103]. 2D peak provides information about the number of layers of the graphite. hBN shows its characteristic Raman peak at f $\approx$ 1360 cm^{-1}. Using the 2D and G sum filters, the Raman spectrum can be integrated in a specific range to create a map as shown in figure 3.2 (b). This helps in the identification of the exact position of the graphite back gate and bilayer graphene. To etch through the top hBN for creating source and drain contacts it is necessary to know the thickness of the top and bottom hBN flakes. This can be done by AFM measurements. It also provides clear information about the surface purity of the sample which is crucial as clean interfaces without the presence of huge bubbles in BLG can help attain good electrostatic pinch-off. AFM and Raman

Analysis are done using Gwyddion, and Project 5 software respectively. After a proper examination of AFM, Raman, and optical images of the stack the ideal location to place the device is decided. The device design is built in KLayout software.
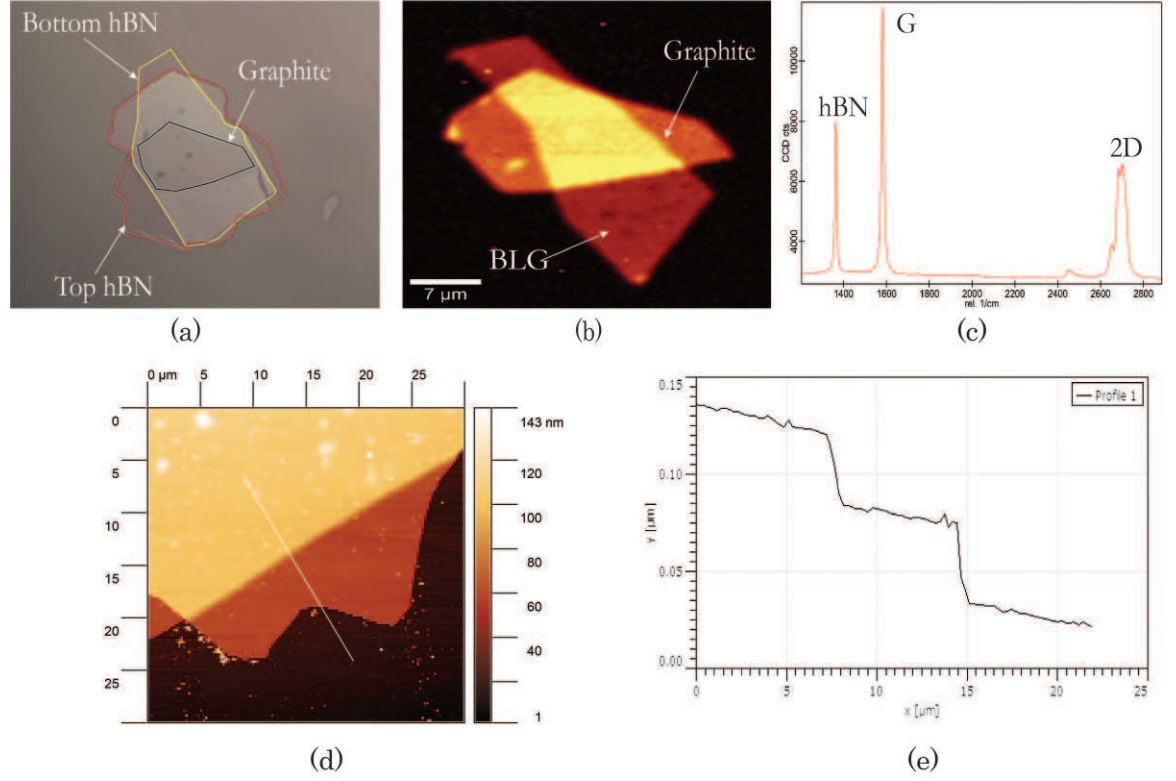

Figure 3.2: (a) Optical microscope image of a stack (b) Raman spectrograph with a filter which integrates over the characteristic Raman 2D peak (c) Characteristic spectrum of BLG on top of hBN (d) AFM micrograph for one of the samples showing regions of different thickness for hBN and graphite (e) Line-cut of the AFM map which is used to calculate hBN thicknesses before etching.

To achieve electrostatic confinement of charge carriers in BLG quantum dot devices several nanometre-sized gate structures are fabricated using standard nanofabrication tools. The metallic gates and superconducting contacts are built in multiple steps. The process begins with Ohmic Point contacts (Normal leads) to BLG. To do this the samples are spin-coated with 50K and 950K PMMA resist. This is followed by the use of electron beam lithography for creating/writing required structures. The samples are then developed using a solution of deionized water and IPA in a 1:3 ratio. Reactive Ion Etching (RIE) using O_2 and CF_4 plasma is done to contact the BLG surface through the top hBN. Consequently, Cr/Au is metalized followed by a lift-off process in an acetone bath. A similar process is followed for creating Leads and Bondpads. Before sputtering a layer of Aluminum or Niobium for

creating superconducting contacts to the BLG, the samples are spin-coated for lithography again followed by development and RIE.
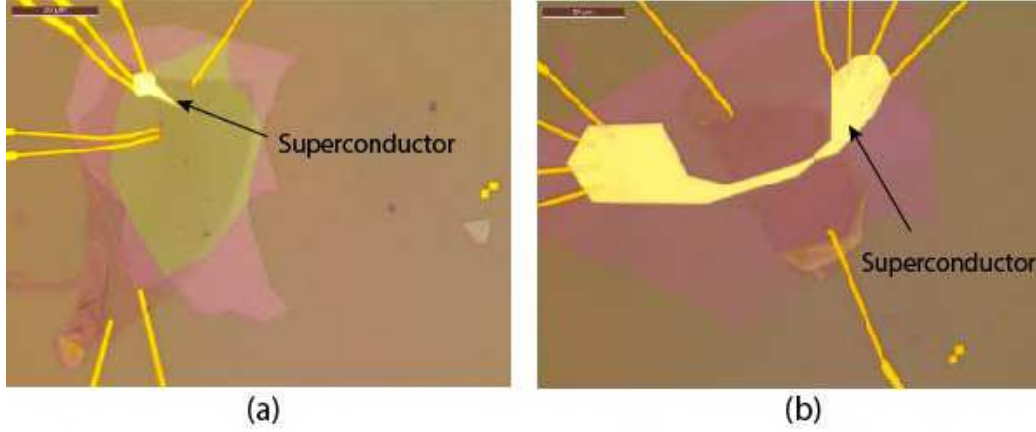

Figure 3.3: (a) Metallic Gate structure with the superconductor depicting device design (e) from figure 3.1(b) Metallic Gate structure with the superconductor depicting the device design (a) from figure 3.1

The superconductor is metalized on top of BLG. This is followed by an Atomic layer deposition of a 15 nm layer of Al_2O_3. Finally, a gate structure for SGs is created. Another layer of ALD is needed before creating the FGs and PGs with each of these again separated by a 15 nm insulating layer of Al_2O_3.

3.3   Measurement Scheme

This section broadly covers the role of all three devices designed for performing certain measurements along with a plausible explanation of how these measurements can be performed and what kind of experimental signatures can be predicted/observed. The main elements consist of leads, tunnel barriers, and QDs. The two types of leads are normal and superconducting which act as reservoirs of electrons connected to the rest of the circuit. Tunnel Barriers can be seen as interfaces separating QD from leads. These can be described with transmission probabilities and defined using electrostatic gating. QDs provide discrete states for electrons to occupy wherein they can retain or transmit an electron to leads separated by tunnel barriers. The first question that needs to be answered is how to create a QD in BLG. The process begins by using SGs for defining a 1-D conducting channel in BLG thus rendering the other regions insulating. Applying a positive voltage to the SGs and a negative voltage to the BG creates a displacement field perpendicular to BLG forming a band gap [38]. The negative BG voltage helps tune the

fermi energy in the 1-d channel making it p-doped. Applying a high positive voltage to a finger gate on top of this channel helps to overcome the negative BG voltage and creates an n-doped region in the p-doped channel forming a QD (see figure 3.4). If the thermal energies of electrons are small as compared to the charging energy and level spacing, the electrons can be confined in a QD whereas if they are comparable to or larger than the charging energy, electrons will readily escape from the dot due to thermal fluctuations, making it difficult to confine electrons. Satisfying this requirement is possible when the devices are cooled to a temperature as low as 20 mK such that the voltage applied across the source and drain contacts satisfies $V_{SD} < k_B T$ [46].
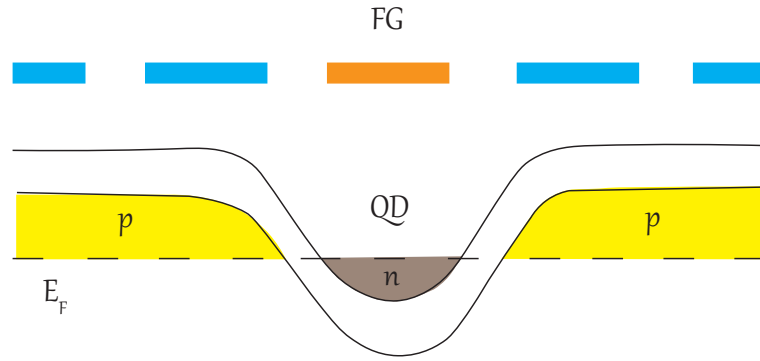
Figure 3.4: Schematic representation of a QD created in a 1-D p-doped channel in BLG

Firstly, the intended measurements for the device design (a) in figure 3.1 will be discussed. This device has been designed to study the formation of ABS and the Andreev supercurrent.

This device consists of two superconducting leads. Transmission of a supercurrent between the two superconducting leads is possible with the presence of discrete electron-hole symmetries extending inside the semiconducting channel of BLG. These symmetries refer to electron-like states (with negative energy) and hole-like states (with positive energy) that are symmetrically arranged around the fermi energy within the hard superconducting gap (see also 2.7 (a) and 2.13 (b)). During the process of AR, electrons are retroreflected as holes, which are time-reversed particles traveling in opposite directions [104]. Because of this back-and-forth electron/hole reflection, resonating standing waves are produced that consist of entangled pairs of electrons and holes with opposite spins [104]. These are termed as ABS.

Figure 3.5: Schematic illustration of DOS vs Energy depicting the formation of electron-hole symmetry states in the semiconducting channel with two superconducting leads. The figure is adapted from [104]

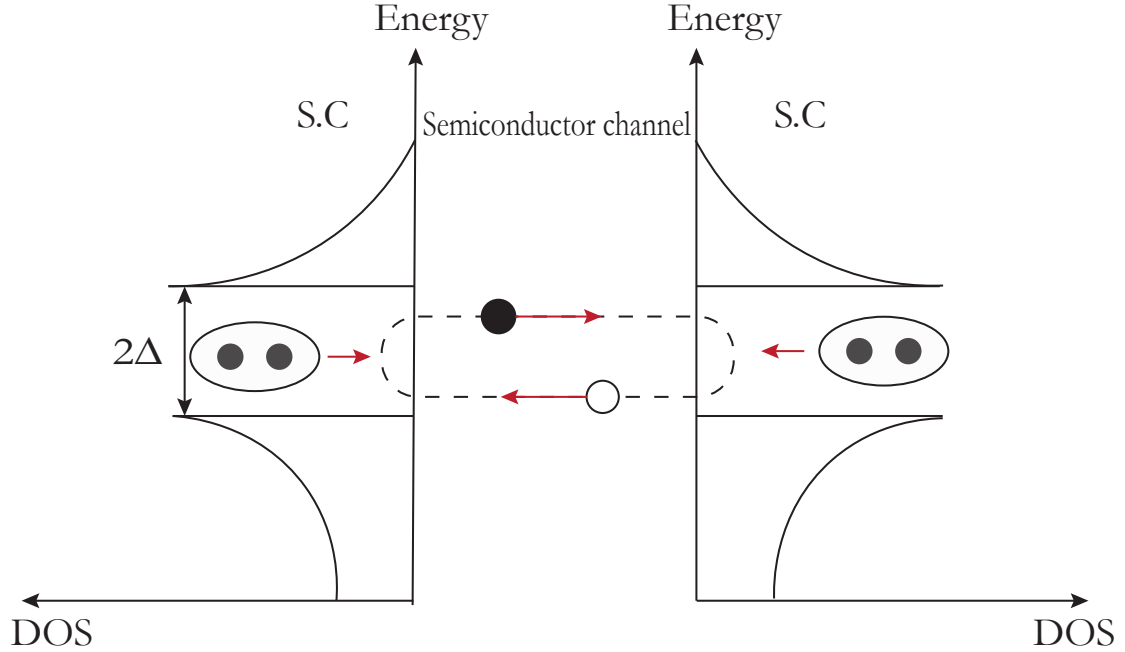The measurement of differential conductance across the two superconducting leads can help estimate the supercurrent. Formation of ABS requires the presence of tunnel barriers that can suppress subgap conductance for non-resonating states. These tunnel barriers can be created using discrete energy levels of a coupled QD. Well-defined resonances can be observed inside the superconducting gap. The experimental feature for an ABS peak consists of bell-shaped resonance curves facing each other while their bases rest on the edges of the superconducting energy gap i.e. $\pm\Delta$ [104, 105]. The occurrence of AR can be confirmed by measuring local conductance signals as a function of varying source-drain voltages. Conductance oscillations can be observed with G_{LL} or $G_{RR} >$ e^2/h as an evidence for AR [106].

Next, the device design labeled as (e) in figure 3.1 will be discussed [86]. This device is a Cooper pair splitter (CPS) designed to study the splitting of a Cooper pair from a superconductor in the middle into the two QDs that are created on either side. This device consists of two normal leads (N_L and N_R see figure 3.6) where the voltage across them is maintained at V_L and V_R respectively while the superconductor remains grounded. To tune the devices for measuring the number of cooper pairs split across the left and right

arms, time-averaged non-local current signals need to be measured i.e. G_{LR} = dI_L/dV_R and G_{RL} = dI_R/dV_L. This current is a direct indication of a cooper pair splitting across the left and right arms because both the electrons of a cooper pair cannot tunnel through one QD unless the chemical potential for a QD is aligned in a way that allows for two electrons to tunnel through the dot at the same time which requires large bias window and isn't possible in the hard superconducting gap.
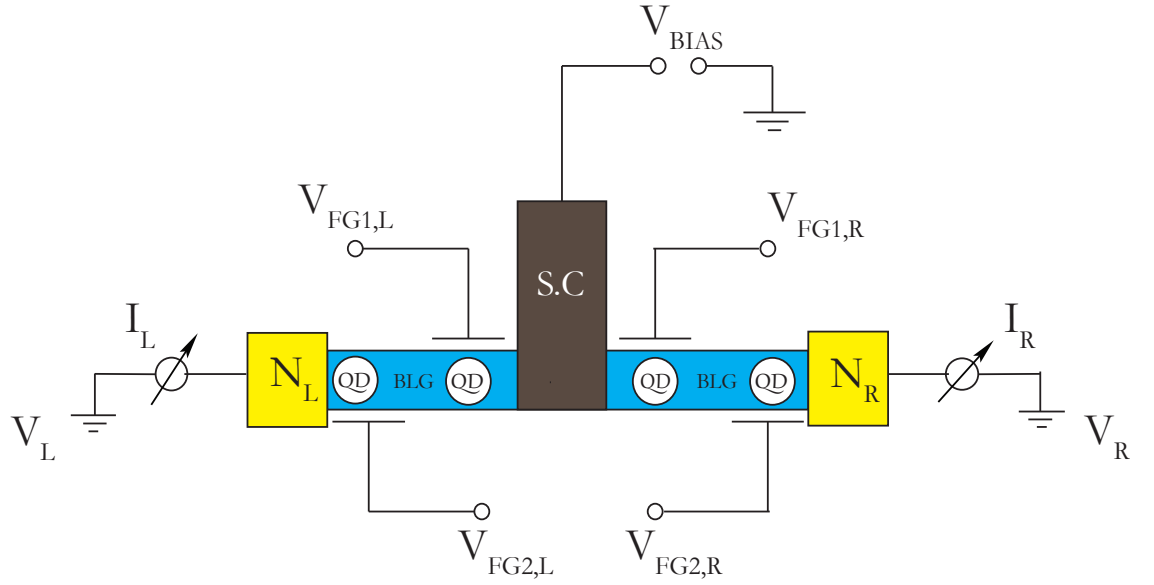
Figure 3.6: Schematic illustration for a Cooper Pair Splitter consisting of two normal leads, a central superconductor, and QDs defined by FG voltages. The figure is adapted and remodified from [60]

The mechanism to split a cooper pair is to first create a tunnel barrier with an FG closest to the superconductor by applying low voltages on left $V_{FG1,L}$ and right side $V_{FG1,R}$ creating two QDs [60]. To observe a hard gap in the superconductor where cooper pairs would be formed, the back gate voltage V_{BG} needs to be tuned to lower energies. The experimental signature for confirming this is possible with local spectroscopy measurements at a finite field (V_{SD} vs B) which demonstrates the features of an ABS and has already been studied (see also 2.13 (b)). It is possible to know the approximate number of electrons coming out of the left and right QDs by creating another tunnel barrier using two more finger gates that lie closest to N_L and N_R thus forming two more QDs (using $V_{FG2,L}$ and $V_{FG2,R}$) away from the superconductor. Performing conductance measurements in a voltage bias window defined for these QD can reveal the conductance resonance peaks. Although it is necessary to highlight two things here, firstly the local conductance can correspond to currents produced by local AR hence they should not be

taken into account as they haven't been produced due to the splitting of a cooper pair. To measure spins separately these local signals due to AR need to be suppressed completely. This can be achieved by creating quantum dots with large charging energies thus allowing only 1e transitions. Previous studies have shown that this method has reduced AR to 5 percent of the total current in each junction [107, 108, 109]. Fabrication of three SGs is predicted to significantly help in measuring non-local conductances in both arms of the Cooper pair splitter by finely tuning the chemical potential of left and right QD.

Before discussing the next device it is quite intriguing to highlight that the efficiency of Cooper pair-splitting can be determined [59]. This refers to estimating the approximate number of cooper pairs split into electrons that tunnel through QDs in the left and right arms of a CPS (see 3.6). In previous studies of splitting of a cooper pair in InSb nanowires, the splitting was found to be 90 percent which is much greater than the minimum requirement of 71 percent for a Bell test [59]. A brief explanation of how the efficiencies of a Cooper pair splitter as determined for InSb nanowires will be explained here. Measuring the non-local conductance across left and right normal leads as a function of time i.e. a time trace with a gradual increase in $V_{FG2,L}$ and $V_{FG2,R}$ allows split electrons from the Superconductor-QD interface to tunnel one by one across the QD-Normal interface. This time trace can be used to determine cooper pair visibilities at N_L and N_R using efficiencies given by $\eta_L = (1 - I_{L,BG}/I_{L,max})$ and $\eta_R = (1 - I_{R,BG}/I_{R,max})$ respectively. Here $I_{L,BG}$ represents the background current when $V_{FG2,R}$ is off-resonance and vice versa. Whereas $I_{L,max}$ represents the maximum current in the time trace. The product of $\eta_R\eta_L$ helps to recognize if the bell inequality is violated or not [110, 111, 112].

Lastly, the measurement scheme for device design (d) from figure 3.1 will be discussed which is based on [59].

This device consists of a superconductor that extends through the 1-D channel in BLG. In this case, two QDs need to be created on either side of the 200 nm superconductor channel where the electrochemical potential for the left dot is μ_{LD} while for the right dot is μ_{RD}. The knobs for controlling these two electrochemical potentials are the finger gate voltage $V_{FG,L}$ and $V_{FG,R}$ respectively. The mean level spacing between any two energy states for a QD can be calculated. This value is important for experiments involving charge sensing and manipulation because when a QD is close to the charge degeneracy point adding or removing electrons significantly changes the energy spectrum [60]. This helps in sensing the charges of electrons that are split from a Copper pair into the QDs. In cooper pair splitting of InSb nanowires, the level spacing of QDs was $\approx$ 1meV [60]. Both the normal leads (BLG source and drain contacts) N_R and N_L are biased with DC voltages V_R and V_L respectively. To study CAR and ECT processes it is essential to

measure non-local conductances i.e. I_L/V_R and I_R/V_L. However, the occurrence of non-local conductance can be either due to CAR or ECT.
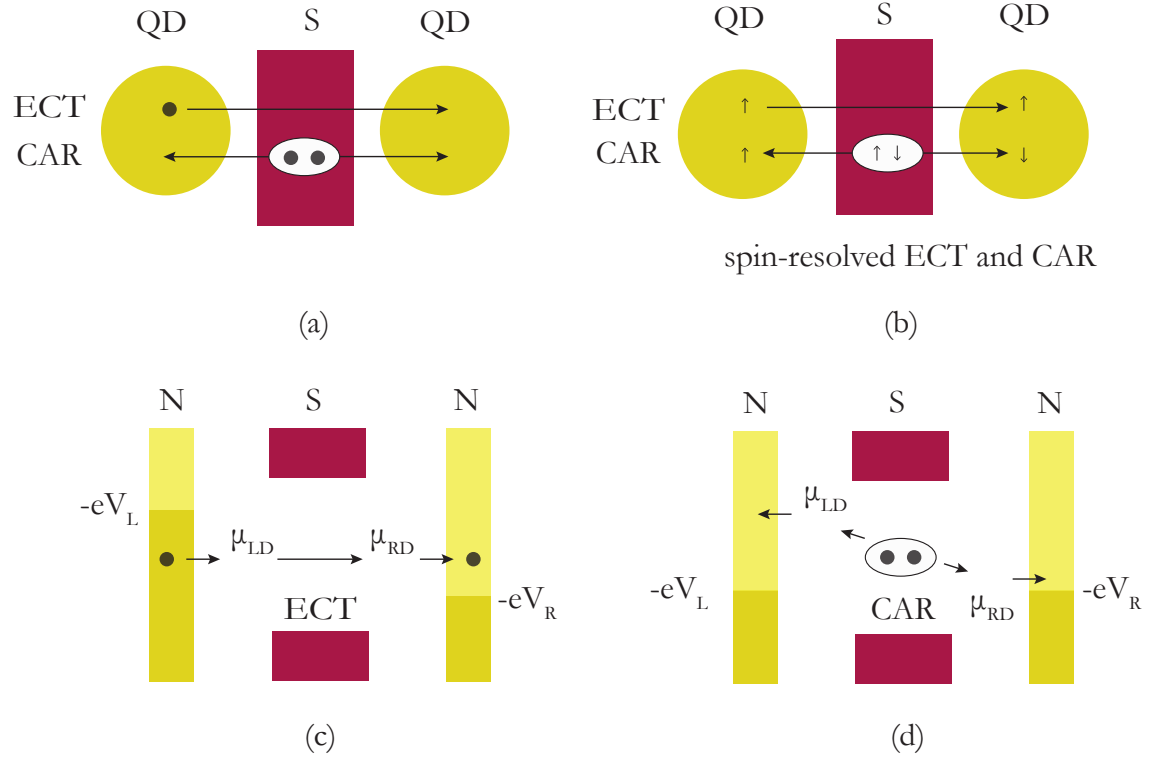
Figure 3.7: (a) The figure depicts the ECT of an electron from one QD on the left to another QD on the right side of the superconductor. For CAR the cooper pair breaks into electrons which tunnel into the QDs on the left and right (b) In the presence of a magnetic field QDs become spin selective allowing to distinguish between ECT and CAR processes(c) The energy alignment showcasing the voltages of normal leads, and electrochemical potentials of two QDs to observe ECT (d) The energy alignment showcasing the voltages of normal leads, and electrochemical potential to observe CAR. The figure is adapted from [60]

In order to distinguish between the currents produced by these two processes restricting the bias settings is essential [113]. To measure CAR signals the bias needs to be such that the electrons split from a cooper pair tunnel into the QDs on the left and right. The bias provides a control knob wherein the FG voltages are set such that μ_{LD} = - μ_{RD}. The voltages across the normal leads can be set such that $-eV_L = -eV_R > \mu_{LD}$ = - μ_{RD} or μ_{LD} = - $\mu_{RD} > eV_L = eV_R$ (see figure 3.7 (d)). In the former case, the cooper pair from the superconductor is split while the latter refers to the creation of a cooper in the superconductor where the V_{BIAS} across the superconductor has to be changed accordingly. The antisymmetric alignment for electrochemical potentials of the left and

right QD is because two electrons with opposite spin are either separated or combined to form a cooper pair whereas symmetric energy alignment for voltages across left and right normal leads (for -eV_L and -eV_R) allows for an equal amount of current to flow through the left and right QD into the normal leads.

For ECT, the electron spin remains conserved (see figure 3.7 (b)). The aligment in such scenario can be done such that $-eV_L < \mu_{LD} = \mu_{RD} < -eV_R$ (see figure 3.7(c)) [59]. This is because the higher bias of the left N lead as compared to the right creates a potential difference for the electron to travel from the left normal lead to the right normal lead. When the electrochemical potential of left and right QDs are aligned equally the electron can hop from the left QD to the right QD either directly or via ABS states in the superconductor. If the current direction is defined to be positive from N_L or N_R to the superconductor then the ECT measurement scheme should yield $I_L = -I_R$ as the electron travels into the superconductor from N_L and outside the superconductor into N_R. Whereas, CAR should give equal current $I_L = I_R$ [60] as can also be understood from the figure (c) and (d) in 3.7. These schemes rule out the process of andreev reflection due to the anti-symmetric energy and current requirements although strong suppression of local AR can also be verified if the transport across the N-QD-S junction remains blocked for bias energies eV $< \Delta$. Sequential resonant tunneling would not occur when the bias voltage and QD energies are less than ABS excitation energy E_0. So, the currents that are observed are solely due to CAR and ECT.

Change in V_{BG} voltage can lead to changes in the amplitude of ECT and CAR signals [59]. Although it can be predicted that in the presence of ABS states the current due to ECT (I_{ECT}) and CAR (I_{CAR}) would be high because more electrons can tunnel via ABS into the QDs without the requirement of a transparent SC-QD interface. The interplay between electron and hole components of ABS helps in controlling CAR and ECT currents via electrostatic gating [114, 115]. These two electron transport processes form the basis of charge detection studies [116]. In the presence of non-homogenous magnetic fields and spin-orbit coupling (SOC), the charge detection can become spin-selective [117, 118]. Although ECT involves the electron with the same spin in both QDs the process of singlet CAR leads to electrons with opposite spins in both QDs. SOC in the bilayer is low ($\approx$ 70 μeV) [119] as compared to that in InSb ($\approx$ 0.25 meV) where due to the presence of inhomogeneous magnetic fields and high SOC the rules of spin combination are not dominant [18]. SOC tends to increase the chances of s+p wave cooper pair formation while s+d is dominant when SOC is absent or low as in the case of BLG [120]. This reduces the chances of observing triplet superconductivity (equal spin pairing) in the devices for this thesis.

Chapter 4

Results and Discussion

This chapter consists of two sections. The first section discusses the transport measurements for a single quantum dot while the second section discusses finite bias spectroscopy measurements for an N-QD-S junction.

4.1   Transport measurements of a single quantum dot

The fabricated sample is characterized in a dry He^3/He^4 dilution refrigerator at a base temperature of 10 mK. The measurements are performed for one of the QD samples without the superconductor for characterizing the formation of QDs which is essential for confirming the viabilities for the rest of the measurements (see figure 4.1 (a)).

To create a QD, the BLG underneath the SGs is turned insulating. For the transport measurements presented here, the SG and BG voltages i.e. V_{SG} and V_{BG} are set to -4.14 V and 3.6 V respectively. This creates a displacement field perpendicular to the BLG forming a bandgap. The chosen values of V_{SG} and V_{BG} tune the fermi energies in the bandgap to form a 1-D channel that is n-doped (see figure 4.1 (b)). The application of a negative voltage to a FG on top of this n-doped channel helps overcome the positive BG voltage and creates a small p-doped region forming a QD (see figure 4.1 (c)). For $V_{FG} < $ -5.4V the 1-D channel is entirely n-doped and the conductivity decreases as there is local depletion underneath the FG. For $V_{FG} > 5.4$ the FG compensates for the charge carrier density induced by the BG voltage (see figure 4.2 a). The p-doped island formed beneath the FG is separated from the 1-D channel on the left and right where the fermi energy lies within the bandgap. These insulating regions create a tunnel barrier between the QD and the source/drain reservoirs.
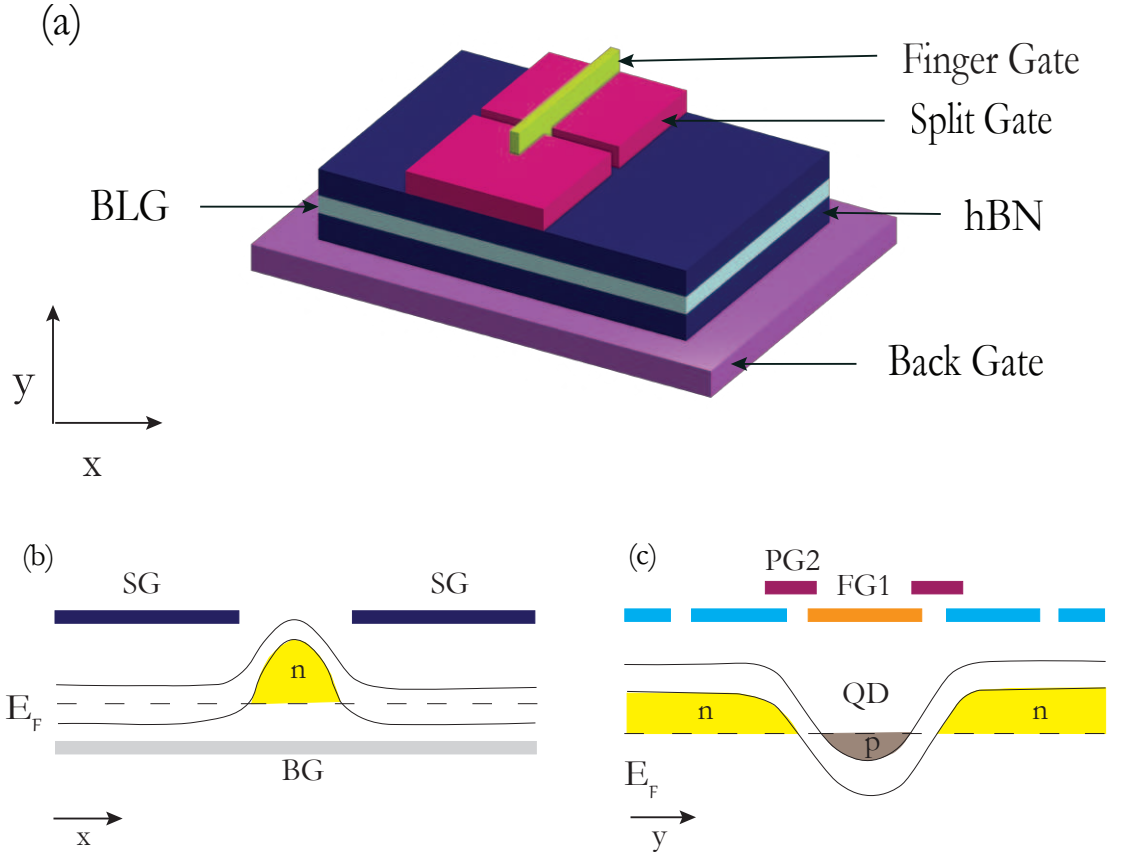
Figure 4.1: (a) QD device geometry. (b) Schematic of band structure perpendicular to the 1-D channel. The voltages applied across SGs and BG create a displacement field perpendicular to BLG forming a bandgap and tuning the fermi energy into this gap. (c) Schematic of band structure along the 1-D channel where the voltage applied across FG1 creates a hole QD. Figure (a) and (b) is adapted from [121]

When the conductance across source and drain reservoirs is measured, the appearance of sharp resonance peaks indicates the tunneling of a hole into and out of the QD as can be seen in figure 4.2. Between two resonance peaks, the current is approximately zero, representing the coulomb blockade regime where there is no available state in the QD for a hole to occupy. At small values of V_{SD} the current I is directly proportional to conductance ($G = I/V_{SD}$). The measurements in figure 4.2 are carried out at a source-drain voltage, V_{SD} that is set to 200 μV. The spacing between any two resonance peaks is proportional to the addition energy required for adding an electron/hole to the QD [45]. Close examination of this spacing between every four resonance peaks indicates the shell-filling sequence of

BLG that originates due to the degenerate spin and valley degrees of freedom [122].
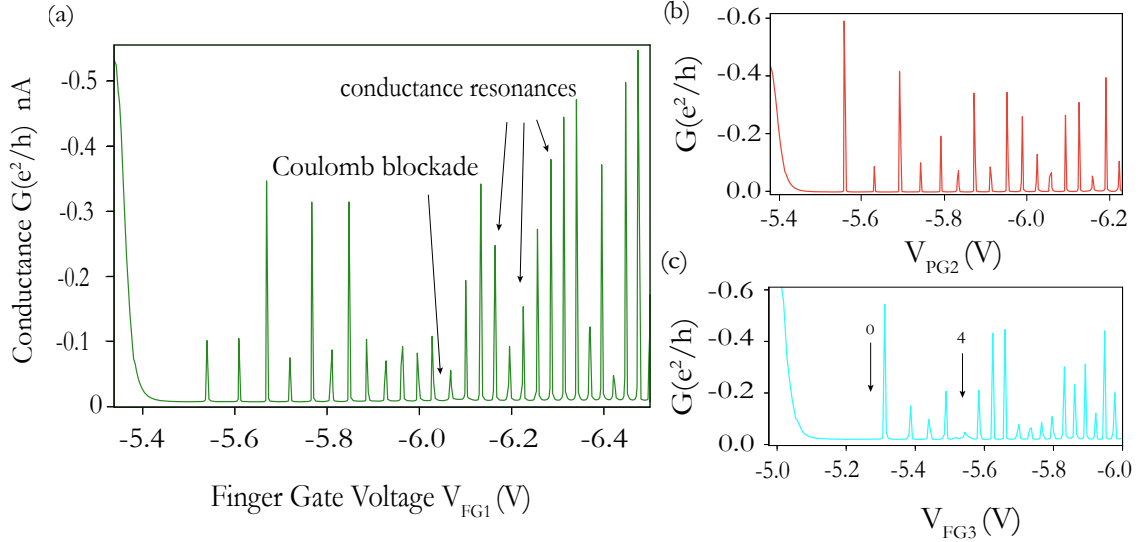
Figure 4.2: (a) Conductance as a function of FG voltage depicting the pinch-off of the 1-D channel and appearance of coulomb peaks when tunneling of holes through the QD takes place. For $V_{FG} < $ - 5.4V the 1-D channel is entirely n doped while for $V_{FG} > $ -5.4V the FG compensates the positive BG voltage creating a hole QD. (b) Conductance measurements for varying PG2 voltages (c) Another QD is created using FG3. At $V_{FG3} \approx 5.5$ V four holes have entered the QD. The filling of orbitals in a QD follows the shell-filling sequence owing to the fourfold degeneracy of spin and valley states in BLG.

For larger source-drain voltages V_{SD} the conductance curve becomes non-linear and in that case, one also has to measure differential conductance (dI/dV$_{SD}$). Effects of coulomb blockade can be observed for non-linear off-resonance conductances [45]. Figure 4.3 shows the two curves where the blue one (on resonance) is for the conductance measured by varying source-drain voltage at a resonance peak for a fixed FG voltage. The conductance increases linearly when $|V_{SD}| < 4k_BT$ while the current remains suppressed when source-drain voltages are larger than $4k_BT$. The red curve shows the non-linear current-voltage characteristic measured at the valley between two resonance peaks where the coulomb blockade is observed (off-resonance) [45].

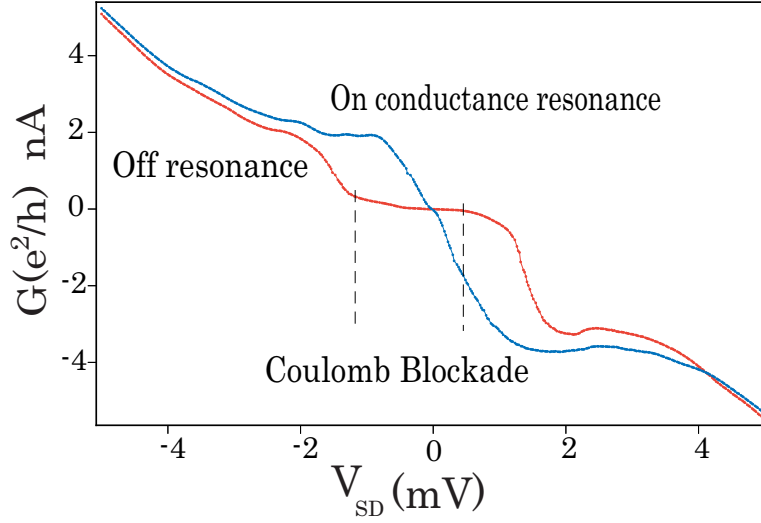Figure 4.3: Conductance of a QD at varying source-drain voltages with the red one showing off-resonance conductance and the blue one shows on resonance. For the former case, coulomb blockade is observed for low V_{SD}.

Excited state spectroscopy of few-electron QDs

Figure 4.4 shows finite bias spectroscopy measurements for FG1. In this plot, the differential conductance is plotted as a function of V_{FG1} and V_{SD}. As discussed in Chapter 2 the data here depicts the formation of coulomb diamonds. It is possible to extract the charging energy of the QD from these diamonds which allows a rough estimation of the size of the QD that is created. However, the electrostatics of BLG QDs having leads with low charge carrier densities is a factor that needs to be accounted for. For these scenarios estimating sizes of different QDs from charging energies doesn't remain well suited [122]. So, it is essential to make two assumptions here. Firstly, it is assumed that the leads have a significant charge carrier density. Secondly, the charging energy is larger in comparison to the level spacing of the QD, such that E_C remains $\approx$ E_{add}. Using the height of the first coulomb diamond the addition energy required to add the 1st hole is determined to be E_{add} = 8.6 meV. This value can be used to determine the QD capacitance and its diameter. The total capacitance of the QD given by $C_{total} = e^2/E_C$ is found to be $\approx$ 18 aF. Using the simple capacitor model by considering BLG separated from BG with a bottom hbN in between serving as the dielectric layer, the diameter can be estimated. The dielectric constant for bottom hBN is $\approx$ 4 with a thickness of $\approx$ 20 nm while the dielectric constant of Al_2O_3 is 9 with a thickness of 15 nm [49].
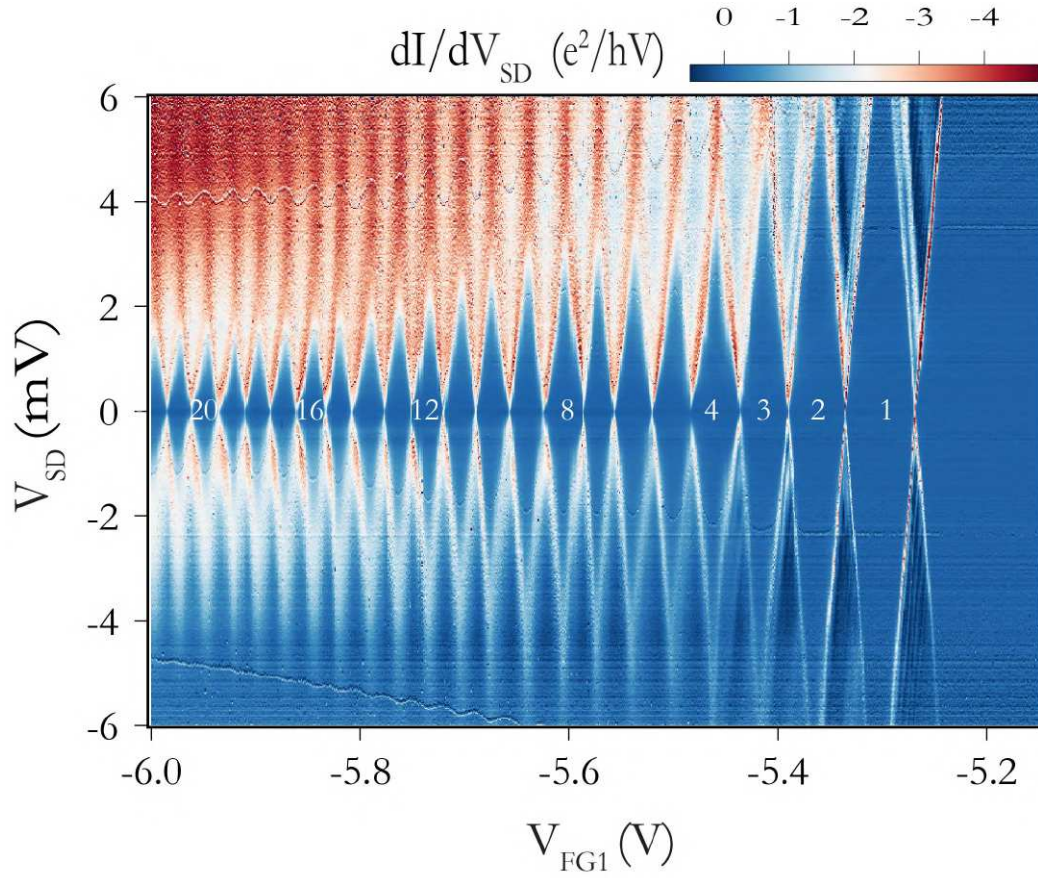
Figure 4.4: Finite bias spectroscopy measurements for FG1. The differential conductance is plotted as a function of V_{FG} and V_{SD}. The numbers indicate the constant hole occupation. The lever arms are tabulated in table 4.1.

To estimate the dot diameter the following relation is used [49]:

$$C_{FG} = \frac{\epsilon_0 d^2}{4\left(\frac{t_{hBN}}{\epsilon_{hBN}} + \frac{t_{Al_2O_3}}{\epsilon_{Al_2O_3}}\right)} \tag{4.1}$$

The FG capacitance C_{FG} can be calculated from the total capacitance using the lever arms i.e using $\alpha_i = C_{0i}/C_{\sum}$ where the numerator would be FG capacitance and the denominator would be the total capacitance of the QD. Using the equation 2.17 the lever arms can be determined. For the QD created with FG1 it is found to be 0.128 for the first-coulomb diamond using which the value of C_{FG1} is estimated to be 2.3 aF. A dot diameter of 83.5 nm is obtained using equation 4.1, which is reasonably close to the lithographic dimensions for the FG1. The lever arms calculated for the first 10 diamonds

are tabulated in 4.1. This finite bias measurement was performed at zero magnetic fields. The variations in the size of coulomb diamonds are because of the four-fold shell filling due to spin and valley degeneracies.

Another QD is created with FG3 in the same way as described for FG1 in figure 4.1 (b). Differential conductances across the channel are measured by tuning voltages for PG2. These are plotted in figure 4.5 (b) and the lever arms for the coulomb diamonds for these plots are tabulated in 4.1. The lever arms calculated for the coulomb diamonds for PG2 are smaller than that due to FG1 and FG3 (see 4.1) because the gate lies farther away from the BLG reducing its efficiency for electrostatic gating. FG1 and FG3 are used for creating QDs one at a time and both are equally efficient in electrostatic gating which is why their lever arms are comparable. The QD capacitance and diameters for FG3 are found to be 1.6 aF and 70 nm respectively which is in agreement with the lithographic dimensions of the FG. The differential conductance as a function of source drain and FG3 voltages is plotted in figure 4.5 (a).
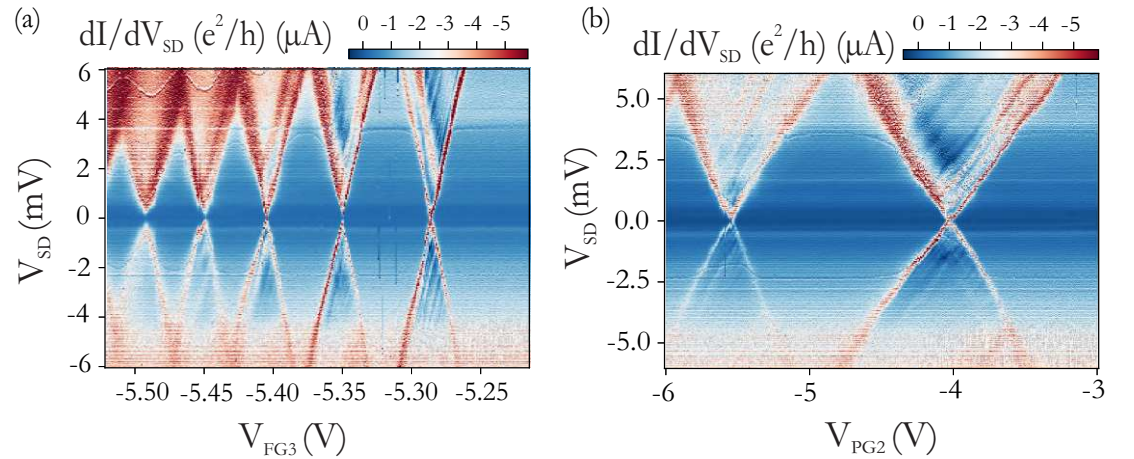
Figure 4.5: (a) Differential conductance as a function of source-drain and FG3 voltages is shown at zero magnetic fields. The lever arms for FG3 are in close agreement with FG1 (b) Differential conductance as a function of V_{SD} and PG2 voltage showing the formation of a coulomb diamond in the bias window. The low value of the lever arm indicates that the PG is inefficient in tuning the fermi energies for confining charge carriers in a QD formed underneath FG1. All the lever arms are tabulated in 4.1

Lever-arms α_i					
N_{QD}	FG1	FG3	PG2	SG	BG
1	0.128	0.091	0.00532	0.310	0.368
2	0.128	0.100			0.378
3	0.127	0.100			0.371
4	0.122				
5	0.129				
6	0.124				
7	0.126				
8	0.122				
9	0.131				
10	0.117				
$\sum$	0.125±0.004	0.097±0.005	0.00532	0.310	0.372±0.005

Table 4.1: Lever-arms α_i for QDs extracted from Coulomb diamonds for FGs, SG, PG2, and BG. Standard deviation and mean are calculated for FG1, FG3, BG. The errors for each lever arm are less than 5 %

Figure 4.6: Finite Bias Spectroscopy for voltage across BG as a function of source-drain voltages. The white arrows indicate the electron transport via ES transitions. The appearance of tiny diamonds within the big coulomb diamonds is because of the formation of several small regions (puddles) of localized charges underneath the SG that behave as QDs and participate in electron transport.

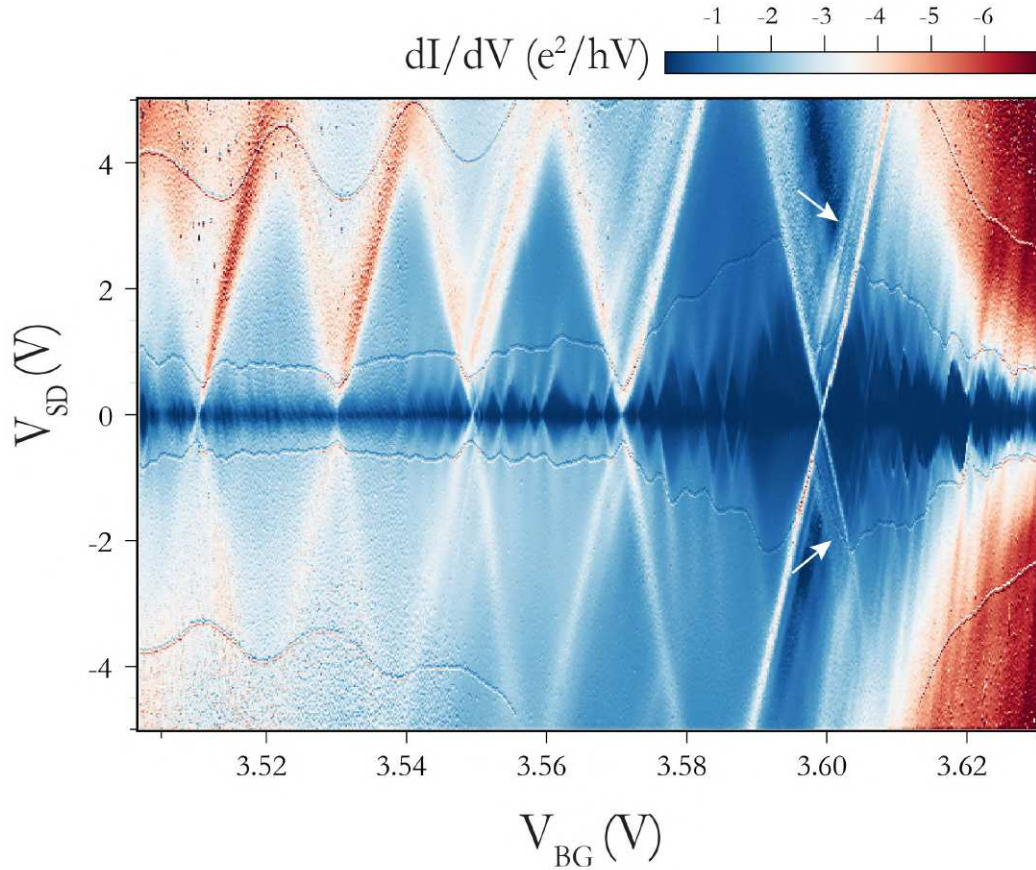The excited state transitions appear as traces of white lines within the coulomb diamonds, as shown by white arrows in figure 4.6 where the bias spectroscopy measurements are plotted for voltage across BG and varying source-drain voltages. The lever arms for the first three diamonds are estimated and tabulated in 4.1. The values for these lever arms are higher than those found from the diamonds for FGs indicating a stronger capacitive coupling offered by the BG. The BG capacitance using C_{total}= 18 aF and the lever arm for the first diamond is estimated to be C_{BG}= 6.6 aF which is larger than the capacitance offered by FG confirming stronger capacitive coupling. The reason is that the BG lies closer to the BLG than the FG, which is further away because of an insulating layer of 15 nm in between.
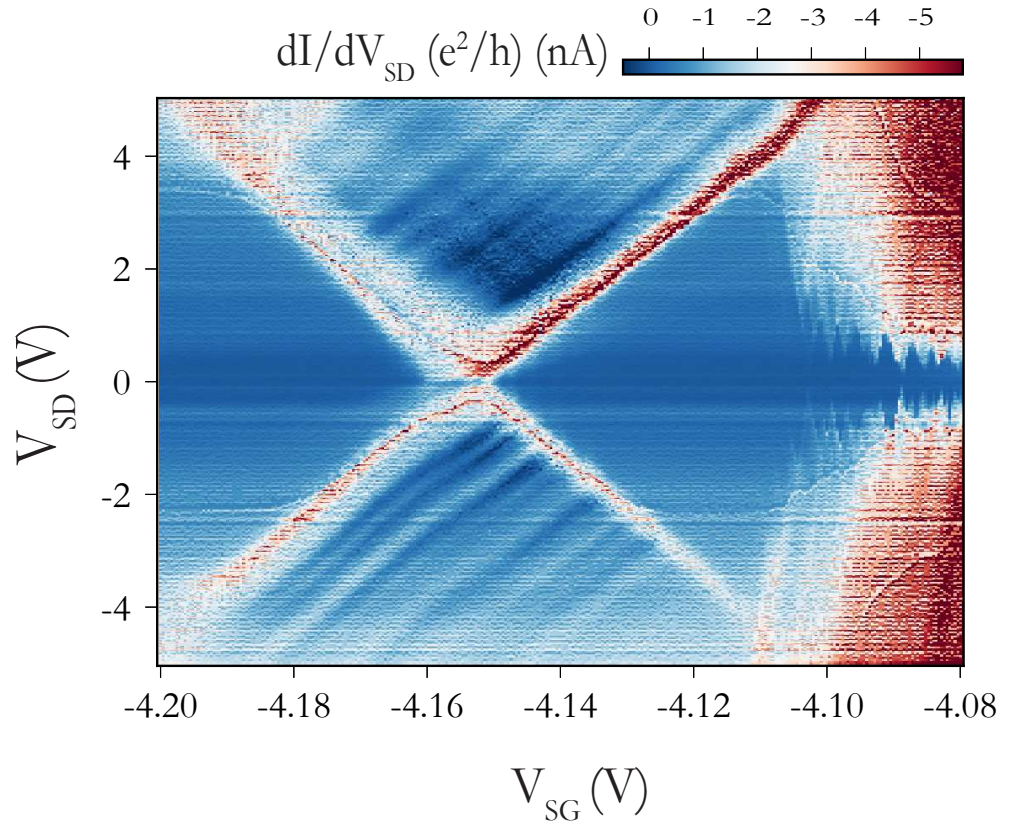
Figure 4.7: Finite Bias Spectroscopy for voltage across SG as a function of source-drain voltages.

Figure 4.7 shows the finite bias spectroscopy for SG voltages as a function of V_{SD}. The lever arm for the diamond is found to be 0.310 which is less as compared to BG indicating the SG lies away from BLG as compared to BG. The lever arms calculated from the bias spectroscopy measurements for SG, BG, and FGs have indicated the sensitivity of the energies of discrete energy states of QDs due to changes in gate voltages. This has

quantified a ratio between a change in the gate voltage and the resulting change in energy of the quantum dot levels indicating the strength of capacitive coupling. A higher lever arm obtained from spectroscopy measurements for the BG and SG has led to a larger change in energy, while a lower lever arm implies that a larger change in gate voltage is needed to produce the same change in energy for the QD. Understanding the lever arms has been crucial for accurately tuning and manipulating the electronic states of quantum dots using different gate voltages and has provided general feasibility for the creation of QDs in the fabricated samples.

This has demonstrated a general viability for the fabricated samples for creating clean well-defined QDs in BLG. Forming electrostatically tunable QDs is a prerequisite for performing measurements across an N-QD-S junction that will be discussed in the following section.

4.2   Transport measurement for a N-QD-S junction
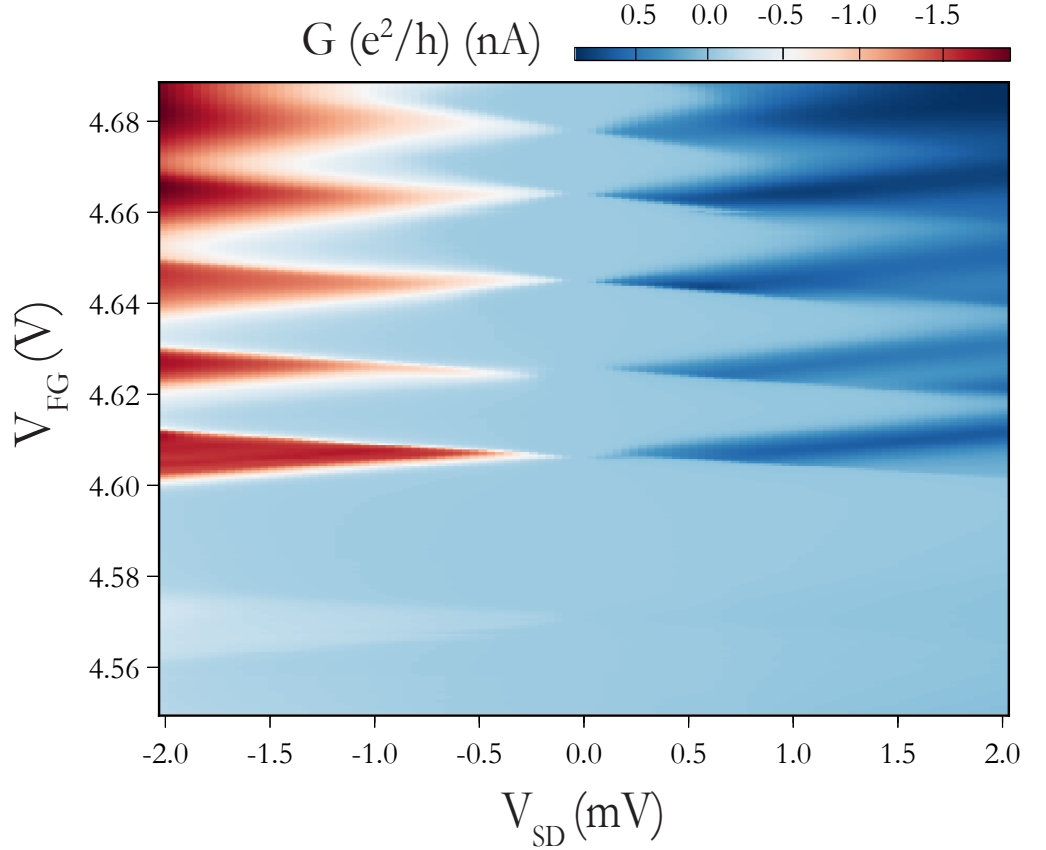
Figure 4.8: Finite Bias Spectroscopy for a N-QD-S junction. A shift in coulomb diamonds is observed in the presence of a superconductor indicating the absence of single quasiparticle excitation within the superconducting gap

In the absence of a magnetic field, finite bias spectroscopy measurements are performed for an N-QD-S junction as shown in figure 4.8. These measurements are performed at fixed V_{SG}= 3.625 V and V_{BG}= -3 V . At a temperature below the critical temperature of the superconductor, there is a formation of a hard superconducting gap. This gap is visible in the bias spectroscopy measurements wherein electrons are forbidden from entering the superconductor leading to a shift in the coulomb diamonds. The gap is estimated to be Δ = 96 μV as shown by a black arrow in 4.9 (a). The figure also highlights a white line which represents the location where the line cut is taken. This line cut for differential current vs source-drain voltage is plotted in figure 4.9 (b). A dip in the conductance is observed in the V_{SD} range from -200 μV to 200 μV. This feature of zero conductance in the gap indicates the presence of cooper pairs occupying the lowest available energy states. The absence of individual energy states for single electrons to occupy leads to zero

conductance within the hard gap thus shifting the coulomb diamonds as displayed in the bias spectroscopy measurements.

In summary, the feature of zero conductance in the hard superconducting gap for an N-QD-S junction was observed thus providing a certainty to perform non-local and local transport measurements to study andreev processes for the fabricated samples.

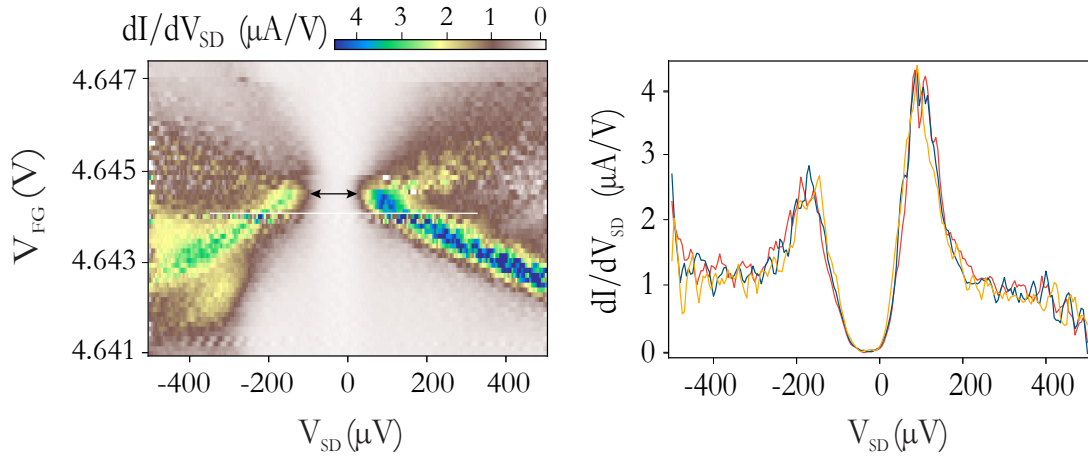Figure 4.9: (a) Zoom in for the bias spectroscopy measurements highlighting the formation of a hard superconducting gap in the superconductor thus indicating the presence of Cooper pairs. (b) Line-cut across the superconducting gap wherein a sudden drop in conductance is observed for low source-drain voltages due to non-availability of single-particle states

Chapter 5

Conclusion and Outlook

The exciting possibilities of combining BLG QDs with superconductors were explored to create a superconductor-semiconductor quantum dot device (SC-QD). This began with the understanding of the fundamentals of BLG QDs and superconductivity to gain insights on how these systems could be integrated. The focus was on studying various processes that occur at the N-QD-S junction and fabricating the SC-QD devices. Transport measurements for two different electrostatically defined QDs in BLG were carried out wherein lever arms were determined from bias spectroscopy measurements for various gates thus highlighting the efficiency of each gate in creating a QD. Occupation of up to 20 electrons was observed within the bias window for FG1. The N-QD-S junction was characterized by a bias spectroscopy measurement highlighting the formation of a hard superconducting gap. Using a line cut, the zero conductance limit was confirmed in the superconducting gap. This also highlights the creation of cooper pairs in the superconductor and the non-availability of single quasiparticle excitation suppressing the flow of electrons from QD to the superconducting lead. These measurements have provided certainty to study andreev processes for the fabricated samples.

This study can be further extended for doing spin selective measurements for the electrons split from a Cooper pair splitter thus acting like a charge detector. Further extensions include creating a kitaev chain (N-QD-S-QD-S-QD-N), which is difficult in terms of fabrication but the presence of two superconductors can lead to a range of new physics appearing at these junctions. Hybrid systems also offer the possibility of detecting a Majorana fermion which is a particle that is its own antiparticle. Although these fermions have zero energy and charge, tunnel spectroscopic measurements can help understand the origin of zero bias peaks (ZBP) which can be due to the Kondo resonances, ABS, or Majorana Bound States (MBS) [123]. Being able to distinguish between these processes in a superconductor quantum dot system can help investigate the existence of Majorana.

Combining semiconductor chips with superconductors is expected to bring significant benefits, especially in creating memory chips that can handle more computations, possibly boosting their capacities by 5-10 % [124]. When referring to accessing data on these chips, the time it takes called the access time is around 580 picoseconds. That's incredibly fast, considering how tiny a picosecond is! In materials like YBaCuO, which have a larger energy gap, the access time is predicted to be even faster [124]. By harnessing the strengths of both types of materials, high-performance computer chips can be created that not only handle more tasks but also do them at blazing speeds. To fully capitalize on the compact nature of semiconductor qubits, recent advancements in quantum dot (QD) array fabrication offer promising solutions to scale up the computations by exploring short-distance coupling between QDs in a 2-D array.

To conclude, the integration of BLG QDs with a superconductor has offered a platform to study the formation of Andreev Bound States and several other processes like Elastic Co-tunneling, Cooper Pair Splitting, and Andreev Reflection helping reach a step closer to realizing andreev qubits.

Bibliography

[1] Francesco Bernardini, Abhijit Chakraborty, and Carlos Ordóñez. Quantum computing with trapped ions: a beginner's guide, 2023.

[2] C. S. Adams, J. D. Pritchard, and J. P. Shaffer. Rydberg atom quantum technologies. 2019.

[3] He-Liang Huang, Dachao Wu, Daojin Fan, and Xiaobo Zhu. Superconducting quantum computing: a review. *Science China Information Sciences*, 63(8), July 2020.

[4] Shannon Harvey. Quantum dots / spin qubits. 2022.

[5] Lars S. Madsen, Fabian Laudenbach, Mohsen Falamarzi. Askarani, Fabien Rortais, Trevor Vincent, Jacob F. F. Bulmer, Filippo M. Miatto, Leonhard Neuhaus, Lukas G. Helt, Matthew J. Collins, Adriana E. Lita, Thomas Gerrits, Sae Woo Nam, Varun D. Vaidya, Matteo Menotti, Ish Dhand, Zachary Vernon, Nicolás Quesada, and Jonathan Lavoie. Quantum computational advantage with a programmable photonic processor. *Nature*, 606(7912):75–81, June 2022.

[6] Chun-Xiao Liu, Guanzhong Wang, Tom Dvir, and Michael Wimmer. Tunable superconducting coupling of quantum dots via andreev bound states in semiconductor-superconductor nanowires. *Physical Review Letters*, 129(26), December 2022.

[7] Sebastiaan L. D. ten Haaf, Qingzhen Wang, A. Mert Bozkurt, Chun-Xiao Liu, Ivan Kulesh, Philip Kim, Di Xiao, Candice Thomas, Michael J. Manfra, Tom Dvir, Michael Wimmer, and Srijit Goswami. Engineering majorana bound states in coupled quantum dots in a two-dimensional electron gas, 2023.

[8] Po Zhang, Hao Wu, Jun Chen, Sabbir A. Khan, Peter Krogstrup, David Pekker, and Sergey M. Frolov. Signatures of andreev blockade in a double quantum dot coupled to a superconductor. *Physical Review Letters*, 128(4), January 2022.

[9] Pujita Das, Sachin Verma, and Ajay. Mean-field study of normal metal-quantum dot-superconductor system in the presence of external magnetic field, 2023.

[10] Zoltán Scherübl, Gergő Fülöp, Jörg Gramich, András Pályi, Christian Schönenberger, Jesper Nygård, and Szabolcs Csonka. From cooper pair splitting to nonlocal spectroscopy of a shiba state. *Physical Review Research*, 4(2), May 2022.

[11] Damaz de Jong, Christian G. Prosko, Lin Han, Filip K. Malinowski, Yu Liu, Leo P. Kouwenhoven, and Wolfgang Pfaff. Controllable single cooper pair splitting in hybrid quantum dot systems. *Phys. Rev. Lett.*, 131:157001, Oct 2023.

[12] Antti Ranni, Fredrik Brange, Elsa T. Mannila, Christian Flindt, and Ville F. Maisi. Real-time observation of cooper pair splitting showing strong non-local correlations. *Nature Communications*, 12(1), November 2021.

[13] Chun-Xiao Liu, Jay D. Sau, Tudor D. Stanescu, and S. Das Sarma. Andreev bound states versus majorana bound states in quantum dot-nanowire-superconductor hybrid structures: Trivial versus topological zero-bias conductance peaks. *Phys. Rev. B*, 96:075161, Aug 2017.

[14] Hongyu Tian and Chongdan Ren. Distinguishing majorana and quasi-majorana bound states in a hybrid superconductor-semiconductor nanowire with inhomogeneous potential barriers. *Results in Physics*, 26:104273, July 2021.

[15] Guang-Yao Huang, Martin Leijnse, Karsten Flensberg, and H. Q. Xu. Tunnel spectroscopy of majorana bound states in topological superconductor/quantum dot josephson junctions. *Physical Review B*, 90(21), December 2014.

[16] Alberto Bordin, Guanzhong Wang, Chun-Xiao Liu, Sebastiaan L.D. ten Haaf, Nick van Loo, Grzegorz P. Mazur, Di Xu, David van Driel, Francesco Zatelli, Sasa Gazibegovic, Ghada Badawy, Erik P.A.M. Bakkers, Michael Wimmer, Leo P. Kouwenhoven, and Tom Dvir. Tunable crossed andreev reflection and elastic cotunneling in hybrid nanowires. *Physical Review X*, 13(3), September 2023.

[17] Joost Ridderbos. *Quantum Dots and Superconductivity in Ge-Si Nanowires.* Phd thesis - research ut, graduation ut, University of Twente, Netherlands, February 2018.

[18] I. van Weperen, B. Tarasinski, D. Eeltink, V. S. Pribiag, S. R. Plissard, E. P. A. M. Bakkers, L. P. Kouwenhoven, and M. Wimmer. Spin-orbit interaction in insb nanowires. *Phys. Rev. B*, 91:201413, May 2015.

[19] M. Hays, V. Fatemi, D. Bouman, J. Cerrillo, S. Diamond, K. Serniak, T. Connolly, P. Krogstrup, J. Nygård, A. Levy Yeyati, A. Geresdi, and M. H. Devoret. Coherent manipulation of an andreev spin qubit. *Science*, 373(6553):430–433, July 2021.

[20] Marta Pita-Vidal, Arno Bargerbos, Rok Žitko, Lukas J. Splitthoff, Lukas Grünhaupt, Jaap J. Wesdorp, Yu Liu, Leo P. Kouwenhoven, Ramón Aguado, Bernard van Heck, Angela Kou, and Christian Kraglund Andersen. Direct manipulation of a superconducting spin qubit strongly coupled to a transmon qubit. *Nature Physics*, 19(8):1110–1115, May 2023.

[21] Guido Burkard, Thaddeus D. Ladd, Andrew Pan, John M. Nichol, and Jason R. Petta. Semiconductor spin qubits. *Reviews of Modern Physics*, 95(2), June 2023.

[22] Mónica Benito and Guido Burkard. Hybrid superconductor-semiconductor systems for quantum technology. 2020.

[23] C. R. Dean, A. F. Young, I. Meric, C. Lee, L. Wang, S. Sorgenfrei, K. Watanabe, T. Taniguchi, P. Kim, K. L. Shepard, and J. Hone. Boron nitride substrates for high-quality graphene electronics. *Nature Nanotechnology*, 5(10):722–726, August 2010.

[24] Alexander A. Balandin. Thermal properties of graphene and nanostructured carbon materials. *Nature Materials*, 10(8):569–581, July 2011.

[25] Suchismita Ghosh, Wenzhong Bao, Denis L. Nika, Samia Subrina, Evghenii P. Pokatilov, Chun Ning Lau, and Alexander A. Balandin. Dimensional crossover of thermal transport in few-layer graphene materials. 2010.

[26] Ed Gerstner. Nobel prize 2010: Andre geim amp; konstantin novoselov. *Nature Physics*, 6(11):836–836, October 2010.

[27] A. K. Geim and K. S. Novoselov. The rise of graphene. *Nature Materials*, 6(3):183–191, March 2007.

[28] Le Minh Tu Phan, Thuy Anh Thu Vo, Thi Xoan Hoang, and Sungbo Cho. Graphene integrated hydrogels based biomaterials in photothermal biomedicine. *Nanomaterials*, 11(4):906, April 2021.

[29] Hao Wang, Zifen Zhao, Panpan Liu, and Xiaogang Guo. Laser-induced graphene based flexible electronic devices. *Biosensors*, 12(2):55, January 2022.

[30] V. J. Emery and S. A. Kivelson. Superconductivity in bad metals. *Physical Review Letters*, 74(16):3253–3256, April 1995.

[31] Patrick A. Lee. Pseudogaps in underdoped cuprates. *Physica C: Superconductivity*, 317–318:194–204, May 1999.

[32] P. W. Anderson. Experimental constraints on the theory of high- t c superconductivity. *Science*, 256(5063):1526–1531, June 1992.

[33] Tingyu Qu, Shangjian Jin, Fuchen Hou, Deyi Fu, Junye Huang, Darryl Foo Chuan Wei, Xiao Chang, Kenji Watanabe, Takashi Taniguchi, Junhao Lin, Shaffique Adam, and Barbaros Özyilmaz. Ferromagnetic superconductivity in two-dimensional niobium diselenide, 2023.

[34] F. K. Unseld, M. Meyer, M. T. Madzik, F. Borsoi, S. L. de Snoo, S. V. Amitonov, A. Sammak, G. Scappucci, M. Veldhorst, and L. M. K. Vandersypen. A 2d quantum dot array in planar 28si/sige. *Applied Physics Letters*, 123(8), August 2023.

[35] Edward McCann and Mikito Koshino. The electronic properties of bilayer graphene. *Reports on Progress in Physics*, 76(5):056503, April 2013.

[36] Emmerich. Investigation of the transport properties and magnetic phase diagram of ultraclean double-graphite-gated bernal bilayer graphene, 2023.

[37] Mikito Koshino and Tsuneya Ando. Transport in bilayer graphene: Calculations within a self-consistent born approximation. *Physical Review B*, 73(24), June 2006.

[38] Eike Icking, Luca Banszerus, Frederike Wörtche, Frank Volmer, Philipp Schmidt, Corinne Steiner, Stephan Engels, Jonas Hesselmann, Matthias Goldsche, Kenji Watanabe, Takashi Taniguchi, Christian Volk, Bernd Beschoten, and Christoph Stampfer. Transport spectroscopy of ultraclean tunable band gaps in bilayer graphene. *Advanced Electronic Materials*, 8(11), July 2022.

[39] Eich, Marius. Electrostatically defined quantum dots in bilayer graphene. 2019.

[40] Yuanbo Zhang, Tsung-Ta Tang, Caglar Girit, Zhao Hao, Michael C. Martin, Alex Zettl, Michael F. Crommie, Y. Ron Shen, and Feng Wang. Direct observation of a widely tunable bandgap in bilayer graphene. *Nature*, 459(7248):820–823, june 2009.

[41] C. Volk. *Quantum transport in graphene nanostructures*. PhD thesis, RWTH Aachen University, 2015.

[42] C. W. J. Beenakker. Theory of coulomb-blockade oscillations in the conductance of a quantum dot. *Phys. Rev. B*, 44:1646–1656, Jul 1991.

[43] Michel H. Devoret, Daniel Esteve, and Cristian Urbina. Single-electron transfer in metallic nanostructures. *Nature*, 360(6404):547–553, December 1992.

[44] F. Kuemmeth, S. Ilani, D. C. Ralph, and P. L. McEuen. Coupling of spin and orbital motion of electrons in carbon nanotubes. *Nature*, 452(7186):448–452, March 2008.

[45] Thomas Ihn. *Semiconductor Nanostructures: Quantum States and Electronic Transport*. Oxford University Press, 2010.

[46] Katrin Hecker. High-frequency manipulation of an electrostatically defined quantum dot in bilayer graphene. Master's thesis, 2nd Institute of Physics A, RWTH Aachen, September 2020.

[47] W. G. van der Wiel, S. De Franceschi, J. M. Elzerman, T. Fujisawa, S. Tarucha, and L. P. Kouwenhoven. Electron transport through double quantum dots. *Rev. Mod. Phys.*, 75:1–22, Dec 2002.

[48] Yuli V. and Yaroslav M. *Quantum Transport: Introduction to nanoscience*. Cambridge University Press, 2010.

[49] Luca Banszerus. *Gate-defined quantum dots in bilayer graphene*. PhD thesis, 2nd Institute of Physics A, RWTH Aachen, August 2022.

[50] Dirk van Delft and Peter Kes. The discovery of superconductivity. *Europhysics News*, 42(1):21–25, January 2011.

[51] J. Bardeen, L. N. Cooper, and J. R. Schrieffer. Theory of superconductivity. *Phys. Rev.*, 108:1175–1204, Dec 1957.

[52] Weng Hong Sio and Feliciano Giustino. Unified ab initio description of fröhlich electron-phonon interactions in two-dimensional and three-dimensional materials. *Phys. Rev. B*, 105:115414, Mar 2022.

[53] Jiahao Yu, Yongman Zhao, Rongshun Pan, Xue Zhou, and Zikai Wei. Prediction of the critical temperature of superconductors based on two-layer feature selection and the optuna-stacking ensemble learning model. *ACS Omega*, 8(3):3078–3090, January 2023.

[54] Ben T. McAllister, Jeremy Bourhill, Wing Him J. Ma, Tim Sercombe, Maxim Goryachev, and Michael E. Tobar. Characterisation of cryogenic material properties of 3d-printed superconducting niobium using a 3d lumped element microwave cavity. 2020.

[55] James William Rohlf. *Modern physics from alpha to Z0*. John Wiley & Sons, Nashville, TN, March 1994.

[56] D. C. Johnston. Elaboration of the alpha-model derived from the bcs theory of superconductivity. 2013.

[57] Silvano De Franceschi, Leo Kouwenhoven, Christian Schönenberger, and Wolfgang Wernsdorfer. Hybrid superconductor–quantum dot devices. *Nature Nanotechnology*, 5(10):703–711, September 2010.

[58] Sayak Ghosh, Arkady Shekhter, F. Jerzembeck, N. Kikugawa, Dmitry A. Sokolov, Manuel Brando, A. P. Mackenzie, Clifford W. Hicks, and B. J. Ramshaw. Thermodynamic evidence for a two-component superconducting order parameter in sr2ruo4. *Nature Physics*, 17(2):199–204, September 2020.

[59] Guanzhong Wang, Tom Dvir, Grzegorz P. Mazur, Chun-Xiao Liu, Nick van Loo, Sebastiaan L. D. ten Haaf, Alberto Bordin, Sasa Gazibegovic, Ghada Badawy, Erik P. A. M. Bakkers, Michael Wimmer, and Leo P. Kouwenhoven. Singlet and triplet cooper pair splitting in hybrid superconducting nanowires. *Nature*, 612(7940):448–453, November 2022.

[60] Guanzhong Wang. Quantum dots coupled to superconductors. 2023.

[61] Jay D. Sau and S. Das Sarma. Realizing a robust practical majorana chain in a quantum-dot-superconductor linear array. *Nature Communications*, 3(1), July 2012.

[62] James F Annett. *Superconductivity, Superfluids and Condensates*. Oxford Master Series in Physics. Oxford University Press, London, England, March 2004.

[63] Michael Tinkham. *Introduction to Superconductivity: v. 1*. Dover Books on Physics. Dover Publications, Mineola, NY, 2 edition, June 2004.

[64] Charles Kittel. *Introduction to solid state physics*. John Wiley & Sons, Nashville, TN, 8 edition, October 2004.

[65] Ruslan Prozorov, Mehdi Zarea, and James A. Sauls. Niobium in the clean limit: An intrinsic type-i superconductor. *Phys. Rev. B*, 106:L180505, Nov 2022.

[66] Hai Li and Gang Ouyang. Nonlocal transport in superconducting heterostructures based on weyl semimetals. *Physical Review B*, 100(8), August 2019.

[67] Ganesh C Paul, Paramita Dutta, and Arijit Saha. Transport and noise properties of a normal metal–superconductor–normal metal junction with mixed singlet and chiral triplet pairings. *Journal of Physics: Condensed Matter*, 29(1):015301, November 2016.

[68] Mikhail S. Kalenkov and Andrei D. Zaikin. Nonlocal andreev reflection at high transmissions. *Physical Review B*, 75(17), May 2007.

[69] V. J. Kauppila, H. Q. Nguyen, and T. T. Heikkilä. Non-equilibrium and proximity effects in superconductor-normal metal junctions. 2013.

[70] Grzegorz P. Mazur, Nick van Loo, Ji-Yin Wang, Tom Dvir, Guanzhong Wang, Aleksei Khindanov, Svetlana Korneychuk, Francesco Borsoi, Robin C. Dekker, Ghada Badawy, Peter Vinke, Sasa Gazibegovic, Erik P. A. M. Bakkers, Marina Quintero-

Pérez, Sebastian Heedt, and Leo P. Kouwenhoven. Spin-mixing enhanced proximity effect in aluminum-based superconductor–semiconductor hybrids. *Advanced Materials*, 34(33), July 2022.

[71] D. Gunnarsson, J. S. Richardson-Bullock, M. J. Prest, H. Q. Nguyen, A. V. Timofeev, V. A. Shah, T. E. Whall, E. H. C. Parker, D. R. Leadley, M. Myronov, and M. Prunnila. Interfacial engineering of semiconductor–superconductor junctions for high performance micro-coolers. *Scientific Reports*, 5(1), December 2015.

[72] Kento Ueda, Sadashige Matsuo, Hiroshi Kamata, Shoji Baba, Yosuke Sato, Yuusuke Takeshige, Kan Li, Sören Jeppesen, Lars Samuelson, Hongqi Xu, and Seigo Tarucha. Dominant nonlocal superconducting proximity effect due to electron-electron interaction in a ballistic double nanowire. *Science Advances*, 5(10), October 2019.

[73] Nathan Tomlin. Using electron-tunneling refrigerators to cool electrons, membranes, and sensors. 01 2008.

[74] So Takei, Benjamin M. Fregoso, Hoi-Yin Hui, Alejandro M. Lobos, and S. Das Sarma. Soft superconducting gap in semiconductor majorana nanowires. 2012.

[75] William S. Cole, S. Das Sarma, and Tudor D. Stanescu. Effects of large induced superconducting gap on semiconductor majorana nanowires. *Physical Review B*, 92(17), November 2015.

[76] M. Kjaergaard, H.J. Suominen, M.P. Nowak, A.R. Akhmerov, J. Shabani, C.J. Palmstrøm, F. Nichele, and C.M. Marcus. Transparent semiconductor-superconductor interface and induced gap in an epitaxial heterostructure josephson junction. *Physical Review Applied*, 7(3), March 2017.

[77] Tudor D. Stanescu, Roman M. Lutchyn, and S. Das Sarma. Soft superconducting gap in semiconductor-based majorana nanowires. *Phys. Rev. B*, 90:085302, Aug 2014.

[78] Kaveh Delfanazari, Reuben K. Puddy, Pengcheng Ma, Teng Yi, Moda Cao, Yilmaz Gul, Ian Farrer, David A. Ritchie, Hannah J. Joyce, Michael J. Kelly, and Charles G. Smith. On-chip andreev devices: Hard superconducting gap and quantum transport in ballistic nb–in0.75ga0.25as-quantum-well–nb josephson junctions. *Advanced Materials*, 29(37), August 2017.

[79] Joost Ridderbos, Matthias Brauns, Folkert K. de Vries, Jie Shen, Ang Li, Sebastian Kölling, Marcel A. Verheijen, Alexander Brinkman, Wilfred G. van der Wiel, Erik P. A. M. Bakkers, and Floris A. Zwanenburg. Hard superconducting gap and diffusion-induced superconductors in ge–si nanowires. *Nano Letters*, 20(1):122–130, November 2019.

[80] Michiel W A de Moor, Jouri D S Bommer, Di Xu, Georg W Winkler, Andrey E Antipov, Arno Bargerbos, Guanzhong Wang, Nick van Loo, Roy L M Op het Veld, Sasa Gazibegovic, Diana Car, John A Logan, Mihir Pendharkar, Joon Sue Lee, Erik P A M Bakkers, Chris J Palmstrøm, Roman M Lutchyn, Leo P Kouwenhoven, and Hao Zhang. Electric field tunable superconductor-semiconductor coupling in majorana nanowires. *New Journal of Physics*, 20(10):103049, October 2018.

[81] Yichun Gao, Wenyu Song, Shuai Yang, Zehao Yu, Ruidong Li, Wentao Miao, Yuhao Wang, Fangting Chen, Zuhan Geng, Lining Yang, Zezhou Xia, Xiao Feng, Yunyi Zang, Lin Li, Runan Shang, Qi-Kun Xue, Ke He, and Hao Zhang. Hard superconducting gap in pbte nanowires. 09 2023.

[82] Xu Cui, Gwan-Hyoung Lee, Young Duck Kim, Ghidewon Arefe, Pinshane Y. Huang, Chul-Ho Lee, Daniel A. Chenet, Xian Zhang, Lei Wang, Fan Ye, Filippo Pizzocchero, Bjarke S. Jessen, Kenji Watanabe, Takashi Taniguchi, David A. Muller, Tony Low, Philip Kim, and James Hone. Multi-terminal transport measurements of mos2 using a van der waals heterostructure device platform. *Nature Nanotechnology*, 10(6):534–540, April 2015.

[83] Riccardo Pisoni, Zijin Lei, Patrick Back, Marius Eich, Hiske Overweg, Yongjin Lee, Kenji Watanabe, Takashi Taniguchi, Thomas Ihn, and Klaus Ensslin. Gate-tunable quantum dot in a high quality single layer mos2 van der waals heterostructure. *Applied Physics Letters*, 112(12), March 2018.

[84] Andreas Pöschl, Alisa Danilenko, Deividas Sabonis, Kaur Kristjuhan, Tyler Lindemann, Candice Thomas, Michael J. Manfra, and Charles M. Marcus. Nonlocal conductance spectroscopy of andreev bound states in gate-defined inas/al nanowires. *Physical Review B*, 106(24), December 2022.

[85] Alejandro M Lobos and S Das Sarma. Tunneling transport in nsn majorana junctions across the topological quantum phase transition. *New Journal of Physics*, 17(6):065010, June 2015.

[86] Alberto Bordin, Guanzhong Wang, Chun-Xiao Liu, Sebastiaan L. D. ten Haaf, Nick van Loo, Grzegorz P. Mazur, Di Xu, David van Driel, Francesco Zatelli, Sasa Gazibegovic, Ghada Badawy, Erik P. A. M. Bakkers, Michael Wimmer, Leo P. Kouwenhoven, and Tom Dvir. Tunable crossed andreev reflection and elastic cotunneling in hybrid nanowires. *Phys. Rev. X*, 13:031031, Sep 2023.

[87] Patrik Recher, Eugene V. Sukhorukov, and Daniel Loss. Andreev tunneling, coulomb blockade, and resonant transport of nonlocal spin-entangled electrons. *Physical Review B*, 63(16), April 2001.

[88] L. Hofstetter, S. Csonka, J. Nygård, and C. Schönenberger. Cooper pair splitter realized in a two-quantum-dot y-junction. *Nature*, 461(7266):960–963, October 2009.

[89] Anindya Das, Yuval Ronen, Moty Heiblum, Diana Mahalu, Andrey V Kretinin, and Hadas Shtrikman. High-efficiency cooper pair splitting demonstrated by two-particle conductance resonance and positive noise cross-correlation. *Nature Communications*, 3(1), November 2012.

[90] Artem V. Galaktionov and Andrei D. Zaikin. Quantum interference and supercurrent in multiple-barrier proximity structures. *Phys. Rev. B*, 65:184507, Apr 2002.

[91] Shun Chi, W. N. Hardy, Ruixing Liang, P. Dosanjh, Peter Wahl, S. A. Burke, and D. A. Bonn. Determination of the superconducting order parameter from defect bound state quasiparticle interference, 2017.

[92] Leonardo Martini, Vaidotas Mišeikis, David Esteban, Jon Azpeitia, Sergio Pezzini, Paolo Paletti, Michał W. Ochapski, Domenica Convertino, Mar Garcia Hernandez, Ignacio Jimenez, and Camilla Coletti. Scalable high-mobility graphene/hbn heterostructures. *ACS Applied Materials & Interfaces*, 15(31):37794–37801, July 2023.

[93] Daniel Rhodes, Sang Hoon Chae, Rebeca Ribeiro-Palau, and James Hone. Disorder in van der waals heterostructures of 2d materials. *Nature Materials*, 18(6):541–549, May 2019.

[94] Tom Vincent, Vishal Panchal, Tim Booth, Stephen R Power, Antti-Pekka Jauho, Vladimir Antonov, and Olga Kazakova. Probing the nanoscale origin of strain and doping in graphene-hbn heterostructures. *2D Materials*, 6(1):015022, December 2018.

[95] Gianluca Giovannetti, Petr A. Khomyakov, Geert Brocks, Paul J. Kelly, and Jeroen van den Brink. Substrate-induced band gap in graphene on hexagonal boron nitride: Ab initio density functional calculations. *Phys. Rev. B*, 76:073103, Aug 2007.

[96] J Sonntag, J Li, A Plaud, A Loiseau, J Barjon, J H Edgar, and C Stampfer. Excellent electronic transport in heterostructures of graphene and monoisotopic boron-nitride grown at atmospheric pressure. *2D Materials*, 7(3):031009, June 2020.

[97] Jeroen Oostinga, Hubert Heersche, Xinglan Liu, Alberto Morpurgo, and Lieven Vandersypen. Gate-induced insulating state in bilayer graphene devices. *Nature materials*, 7:151–7, 03 2008.

[98] Matteo Todeschini, Alice Bastos da Silva Fanta, Flemming Jensen, Jakob Birkedal Wagner, and Anpan Han. Influence of ti and cr adhesion layers on ultrathin au films. *ACS Applied Materials & Interfaces*, 9(42):37374–37385, October 2017.

[99] Min Yi and Zhigang Shen. A review on mechanical exfoliation for the scalable production of graphene. *Journal of Materials Chemistry A*, 3(22):11700–11715, 2015.

[100] Chandkiram Gautam and Selvam Chelliah. Methods of hexagonal boron nitride exfoliation and its functionalization: covalent and non-covalent approaches. *RSC Advances*, 11(50):31284–31327, 2021.

[101] Jan-Lucas Uslu, Taoufiq Ouaj, David Tebbe, Alexey Nekrasov, Jo Henri Bertram, Marc Schütte, Kenji Watanabe, Takashi Taniguchi, Bernd Beschoten, Lutz Waldecker, and Christoph Stampfer. An open-source robust machine learning platform for real-time detection and classification of 2d material flakes. *Machine Learning: Science and Technology*, 5(1):015027, February 2024.

[102] Mallikarjuna Gurram. *Spin transport in graphene - hexagonal boron nitride van der Waals heterostructures*. PhD thesis, University of Groningen, 2018.

[103] Afsal Kareekunnan, Masashi Akabori, Kenji Watanabe, Takashi Taniguchi, and Hiroshi Mizuta. Raman spectroscopy of doubly aligned bilayer graphene. *Applied Physics Letters*, 124(9), February 2024.

[104] J-D. Pillet, C. H. L. Quay, P. Morfin, C. Bena, A. Levy Yeyati, and P. Joyez. Andreev bound states in supercurrent-carrying carbon nanotubes revealed. *Nature Physics*, 6(12):965–969, November 2010.

[105] Travis Dirks, Taylor L. Hughes, Siddhartha Lal, Bruno Uchoa, Yung-Fu Chen, Cesar Chialvo, Paul M. Goldbart, and Nadya Mason. Transport through andreev bound states in a graphene quantum dot. *Nature Physics*, 7(5):386–390, February 2011.

[106] M. Hashisaka, T. Jonckheere, T. Akiho, S. Sasaki, J. Rech, T. Martin, and K. Muraki. Andreev reflection of fractional quantum hall quasiparticles. *Nature Communications*, 12(1), May 2021.

[107] L. Hofstetter, S. Csonka, J. Nygård, and C. Schönenberger. Cooper pair splitter realized in a two-quantum-dot y-junction. *Nature*, 461(7266):960–963, October 2009.

[108] Anindya Das, Yuval Ronen, Moty Heiblum, Diana Mahalu, Andrey V Kretinin, and Hadas Shtrikman. High-efficiency cooper pair splitting demonstrated by two-particle conductance resonance and positive noise cross-correlation. *Nature Communications*, 3(1), November 2012.

[109] L. G. Herrmann, F. Portier, P. Roche, A. Levy Yeyati, T. Kontos, and C. Strunk. Carbon nanotubes as cooper-pair beam splitters. *Phys. Rev. Lett.*, 104:026801, Jan 2010.

[110] J. Schindele, A. Baumgartner, and C. Schönenberger. Near-unity cooper pair splitting efficiency. *Physical Review Letters*, 109(15), October 2012.

[111] Shiro Kawabata. Test of bell's inequality using the spin filter effect in ferromagnetic semiconductor microstructures. *Journal of the Physical Society of Japan*, 70(5):1210–1213, May 2001.

[112] P. Samuelsson, E. V. Sukhorukov, and M. Büttiker. Orbital entanglement and violation of bell inequalities in mesoscopic conductors. *Physical Review Letters*, 91(15), October 2003.

[113] G.C. Ménard, G.L.R. Anselmetti, E.A. Martinez, D. Puglia, F.K. Malinowski, J.S. Lee, S. Choi, M. Pendharkar, C.J. Palmstrøm, K. Flensberg, C.M. Marcus, L. Casparis, and A.P. Higginbotham. Conductance-matrix symmetries of a three-terminal hybrid device. *Physical Review Letters*, 124(3), January 2020.

[114] J. Schindele, A. Baumgartner, R. Maurand, M. Weiss, and C. Schönenberger. Nonlocal spectroscopy of andreev bound states. *Physical Review B*, 89(4), January 2014.

[115] Jeroen Danon, Anna Birk Hellenes, Esben Bork Hansen, Lucas Casparis, Andrew P. Higginbotham, and Karsten Flensberg. Nonlocal conductance spectroscopy of andreev bound states: Symmetry relations and bcs charges. *Physical Review Letters*, 124(3), January 2020.

[116] Patrik Recher, Eugene V. Sukhorukov, and Daniel Loss. Quantum dot as spin filter and spin memory. *Phys. Rev. Lett.*, 85:1962–1965, Aug 2000.

[117] Lev P. Gor'kov and Emmanuel I. Rashba. Superconducting 2d system with lifted spin degeneracy: Mixed singlet-triplet state. *Phys. Rev. Lett.*, 87:037004, Jul 2001.

[118] N. Banerjee, J. A. Ouassou, Y. Zhu, N. A. Stelmashenko, J. Linder, and M. G. Blamire. Controlling the superconducting transition by spin-orbit coupling. *Phys. Rev. B*, 97:184521, May 2018.

[119] S. Konschuh, M. Gmitra, D. Kochan, and J. Fabian. Theory of spin-orbit coupling in bilayer graphene. *Physical Review B*, 85(11), March 2012.

[120] Jingxiang Zhao and Qiang Gu. Cooper pairing in a doped 2d antiferromagnet with spin-orbit coupling. *Scientific Reports*, 8(1), January 2018.

[121] Samuel Moeller. Shell-filling in gate-defined bilayer graphene quantum dots, 2020.

[122] S. Möller, L. Banszerus, A. Knothe, L. Valerius, K. Hecker, E. Icking, K. Watanabe, T. Taniguchi, C. Volk, and C. Stampfer. Impact of competing energy scales on the shell-filling sequence in elliptic bilayer graphene quantum dots. *Phys. Rev. B*, 108:125128, Sep 2023.

[123] V. Mourik, K. Zuo, S. M. Frolov, S. R. Plissard, E. P. A. M. Bakkers, and L. P. Kouwenhoven. Signatures of majorana fermions in hybrid superconductor-semiconductor nanowire devices. *Science*, 336(6084):1003–1007, May 2012.

[124] T. Van Duzer. Superconductor—semiconductor hybrid devices, circuits and systems. *Cryogenics*, 28(8):527–531, August 1988.

Supplementary Reading

In the theory chapter of the thesis, the electron transport processes for the QD-S-QD system where the superconductor was grounded have been discussed. The highlight here will be to understand the difference between grounded and ungrounded superconductors. In the former, ECT and CAR occur via quasiparticle formation in the superconductor but the existence of quasiparticles is considerably forbidden in the ungrounded case [1]. It is possible to electrostatically control the presence of quasiparticles in the superconductor to study the system as shown by a recent study in [2]. The electronic transport processes involved in a QD-S-QD system consist of two coupled QDs. To understand the transport in a QD-S-QD system where the superconductor is ungrounded it is important to understand transport processes for two QDs in series. Although the two QDs in a QD-S-QD system are separated by a superconducting island they induce cross-capacitive talks with each other. The electrostatics and transport behavior of such a system comprising two serially connected quantum dots, known as a double quantum dot (DQD), coupled to a source and drain reservoir will be discussed in the following section.

Capacitance model for a Double Quantum Dot

Figure 1 illustrates the capacitance model of a double quantum dot (DQD). This section has been adapted from [3]. The model consists of two quantum dots that are linked via a mutual tunneling barrier characterized by a tunneling rate t_m. Each quantum dot is connected to either the source or drain reservoir with tunneling rates Γ_S and Γ_D, respectively. Both quantum dots are controlled by gates (G_1 and G_2) with gate voltages V_{G1} and V_{G2} which modulate the electron occupation in a QD through capacitive coupling via $C_{1,1}$ and $C_{2,2}$. The cross-capacitive coupling between the gates and the quantum dots is given by $C_{1,2}$ and $C_{2,1}$. Electrons occupying one quantum dot interact electrostatically with electrons on the other quantum dot, by a mutual capacitance term denoted as C_m. This mutual capacitance reflects the influence of charge on one QD on the energy levels and transport properties of the other QD, contributing to the overall behavior of the DQD system. The quantum energy is assumed to be the single particle energy of each QD and the charges on the QD are assumed to be integer multiples of the elementary charge. With this, a system of equations for the charge on each QD can be set up as follows.

$$A_1 = Q_1 - Q_1^{(0)} - \sum_{j=2}^{n} C_{1j}\phi_j$$

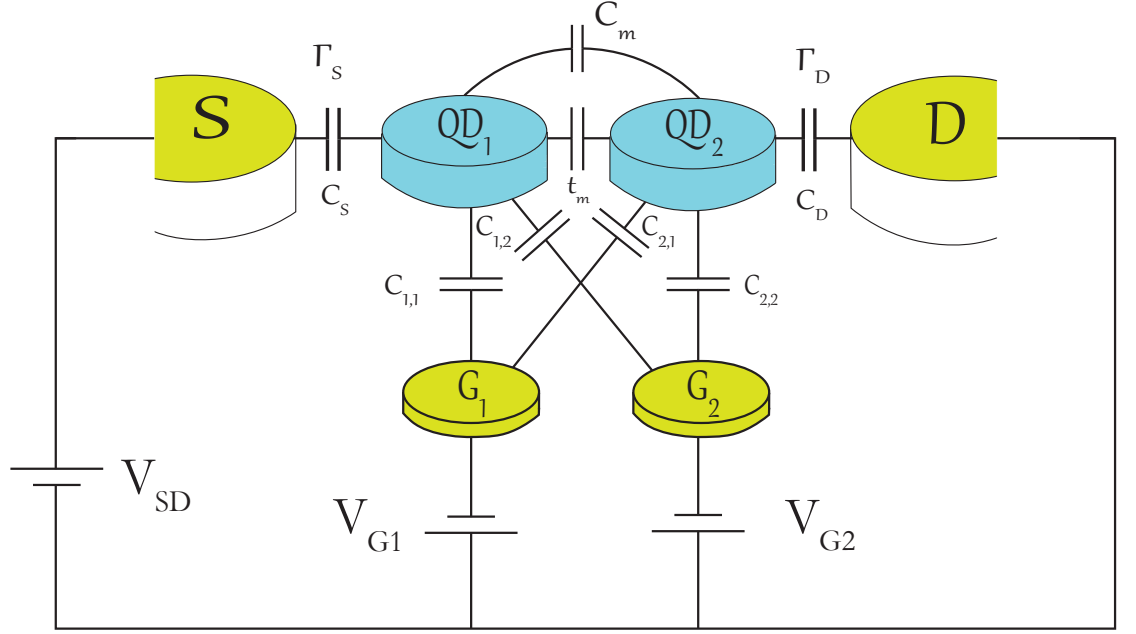$$A_2 = Q_2 - Q_2^{(0)} - \sum_{j=2}^{n} C_{2j}\phi_j.$$

Figure 1: Schematic illustration for capacitance model for a Double Quantum Dot that is tunnel coupled to source and drain reservoir. Both QDs are capacitively coupled to gate electrodes and the inter-dot coupling is given by cross capacitances between QD_1 and G_2 similarly between QD_2 and G_1. The figure is adapted from [4, 5].

Using these equations the electrostatic energy of the QDs can be determined to be

$$E(N_1, N_2) = \frac{e^2 N_1^2}{2C_{11}^1} - eN_1 \sum_{j=2}^{n} \alpha_{1j}\phi_j + \frac{e^2 N_2^2}{2C_{22}^2} - eN_2 \sum_{j=2}^{n} \alpha_{2j}\phi_j + \frac{e^2 N_1 N_2}{C_{\text{TB}}}, \qquad (1)$$

where

$$C_{ii}^{(i)} = C_{ii}(1 - \frac{C_{12}C_{21}}{C_{11}C_{22}}) \quad , i = 1, 2 \qquad (2)$$

is the total capacitance of one QD and

$$C_{\text{TB}} = \frac{C_{11}C_{22} - C_{12}C_{21}}{-C_{12}} \qquad (3)$$

is the mutual capacitance between the two QDs. For the expression of the total energy, the single-particle energies of each QD are added leading to

$$E(N_1, N_2) = \sum_{n=0}^{N_1} \epsilon_n^{(1)} + \frac{e^2 N_1^2}{2C_{11}^1} - eN_1 \sum_{j=2}^{n} \alpha_{1j}\phi_j + \sum_{n=0}^{N_2} \epsilon_n^{(2)} + \frac{e^2 N_2^2}{2C_{22}^2} - eN_2 \sum_{j=2}^{n} \alpha_{2j}\phi_j + \frac{e^2 N_1 N_2}{C_{\text{TB}}}. \quad (4)$$

2

Here, $\epsilon_n^{(1,2)}$ are the single-particle energies in QD$_1$ and QD$_2$. $eN_{1,2} \sum_{j=2}^{n} \alpha_{1,2j} \phi_j$ represents the shifts in energies induced by the gates on QD$_1$ and QD$_2$. $E_{C1} = \frac{e^2 N_1^2}{2C_{1,1}^0}$ and $E_{C2} = \frac{e^2 N_2^2}{2C_{2,2}^1}$ are the charging energies of both QDs while the last term $\frac{e^2 N_1 N_2}{C_{12}}$ represents electrostatic coupling between the two QDs. The electrochemical potentials for each QD are then given by

$$\mu_{N_1}^{(0)}(N_2) = \epsilon_{N_1}^{(0)} + \frac{e^2}{C_{11}^1}(N_1 - \frac{1}{2}) - e \sum_{j=2}^{n} \alpha_{1j} \phi_j + \frac{e^2}{C_{\text{TB}}} N_2$$

$$\mu_{N_2}^{(1)}(N_1) = \epsilon_{N_2}^{(1)} + \frac{e^2}{C_{22}^2}(N_2 - \frac{1}{2}) - e \sum_{j=2}^{n} \alpha_{2j} \phi_j + \frac{e^2}{C_{\text{TB}}} N_1.$$

The electrochemical potential $\mu_{N_1}^{(0)}$ depends on the number of charge carriers in QD$_1$ which in turn shifts the energy in QD$_2$ and vice versa.

Charge Carrier Transport in a Double Quantum Dot

To enable current flow through the double quantum dot (DQD) system, the electrochemical potentials of both quantum dots (QDs) must be aligned with those of the source (S) and drain (D) electrodes [6]. This is referred to as the linear transport regime ($\mu_S = \mu_N = \mu_M = \mu_D$) [4]. This condition ensures that charge carriers can flow freely between the electrodes and the QDs (see 2 (a)). When a bias voltage is applied to facilitate charge carrier transport the electrochemical potentials must satisfy the inequality $\mu_S \geq \mu_N \geq \mu_M \geq \mu_D$. This ensures that the energy levels are appropriately aligned for efficient charge transport through the system. To visualize the behavior of the system, one can plot the applied voltages on both quantum dots against each other, creating a charge stability diagram (CSD). This diagram illustrates regions of stable charge configurations for each quantum dot as the gate voltages are increased. These stable regions depict increasing charge states for each QD. In CSD in figure 3 (a), green lines represent co-tunneling lines, indicating the dominant paths for charge carrier transport when the electrochemical potentials of only one QD are within the bias window. In such cases, charge carriers tunnel from the source to one QD and then directly to the drain, bypassing the second QD.
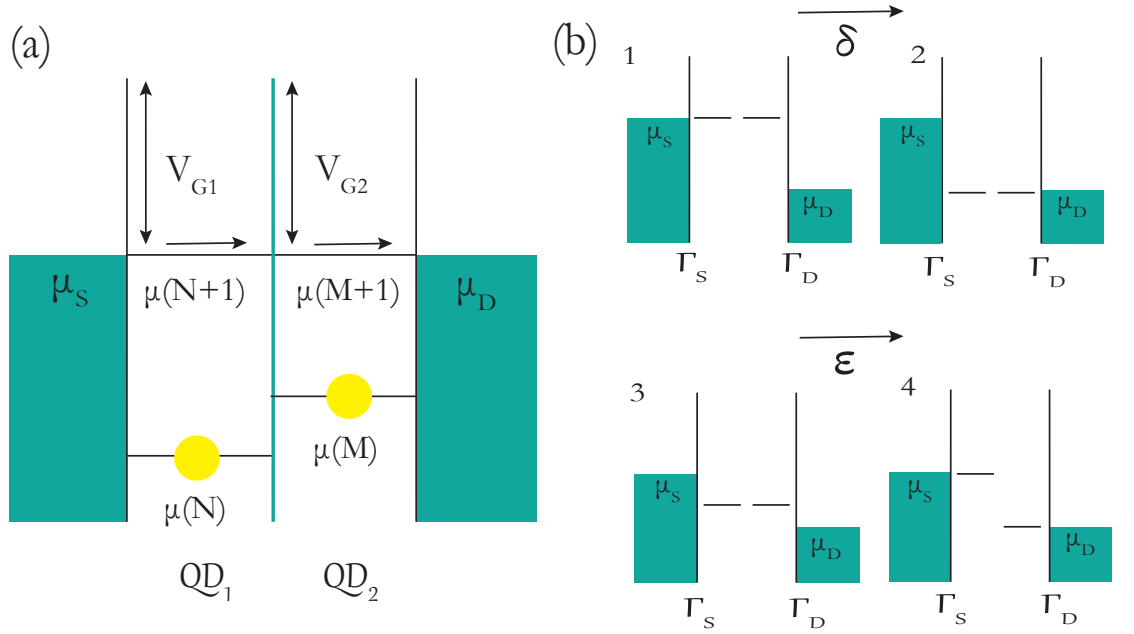
Figure 2: (a) Schematic of electron transport through double QD (DQD) in linear transport regime where potentials of source and drain reservoirs are aligned with the electrochemical potentials of both QDs. (b) Here $\epsilon = E_1 - E_2$ and $\delta = E_1 + E_2$. Increasing δ from 1 to 2 leads to the electrochemical potentials of both QDs being aligned to the drain electrode (in 2) from the source electrode (in 1). Increasing ϵ leads to an increase in the difference between the electrochemical potentials of both QDs. The figure is adapted from [4, 7].

At the intersections of the co-tunneling lines from both QDs, triangular regions known as triple points are formed. These regions are crucial as they facilitate charge transport through the simultaneous involvement of both QDs. Triple points represent a unique configuration where charge carriers can efficiently tunnel through the entire DQD system. Each triple point in the charge stability diagram consists of two triangles, one representing electron transport and the other representing hole transport. The outlines of these triangles form as a result of the alignment of either μ_N or μ_M with μ_S or μ_D, respectively. The size of each triangle is determined by the bias window, allowing for the determination of the lever arm (α) using the formula $\alpha = V_{SD}/dV$, where V_{SD} is the voltage bias and dV is the voltage difference on the gate axis. Two key parameters characterize the triple points i.e. detuning (ϵ) and common energy (δ). The detuning energy ($\epsilon = E_1 - E_2$) quantifies the energy difference between the two quantum dots (QDs). At the onset of the triple point, ϵ is zero, and it increases along the detuning axis until it reaches eV_{SD} at the end of the triple point, marked by circles in the figure 3 (d). On the other hand, the common energy ($\delta = E1 + E2$) represents the total energy of both QDs. These parameters, detuning and common energy, provide valuable insights into the energy

landscape of the triple points, offering a comprehensive understanding of the charge transport dynamics in the DQD system.
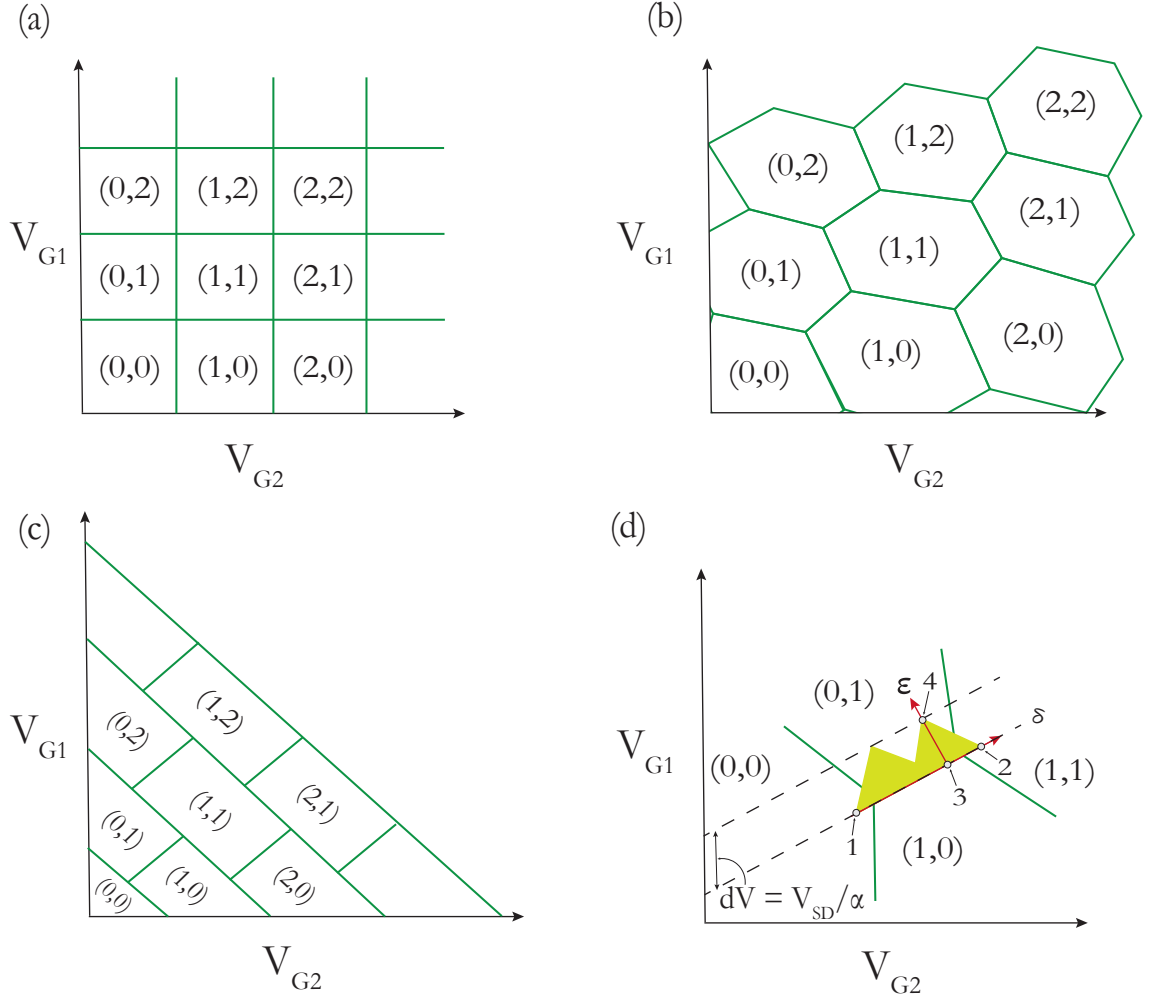

Figure 3: (a) CSD in the case of small Inter-Dot Coupling (b) CSD for intermediate inter-dot coupling (c) CSD for strong interdot coupling (d) Zoom in of (b) showing triple point for intermediately coupled QDs. The figure is adapted from [4, 7, 8]

Initially, the cross-capacitances of the gates and the mutual capacitance of the QDs are assumed to be zero. Under this simplification, each QD's electrochemical potential is solely determined by its respective gate voltage where the CSD is given by 3 (a). However, considering the cross capacitances of the gates, μ_1(N) and μ_2(M) become dependent on both gate voltages, resulting in a tilt of the horizontal and vertical co -tunneling lines which appear as hexagonal-shaped regions of fixed charge occupation in the intermediately coupled QD regime (see Figure 3(b)). Considering that three

consecutive tunneling processes are necessary for an electron to pass through the DQD from source to drain, two possible situations are present. These will be explained here.

For electron transport, the DQD is in a charge state (0,0). An electron tunnels into QD_1, changing the charge state to (1,0). The excess electron then tunnels into QD_2 (0,1) before exiting QD_2 to the drain electrode, resulting in the initial charge state of (0,0). For hole transport, the charge state is (1,1). An electron leaves QD_2, resulting in a charge state of (1,0). Subsequently, an electron tunnels from QD_1 to QD_2, yielding (0,1) before another electron tunnels into QD_1 from the source lead that results in the initial state of (1,1) (see Figure 3 (a)). Overlap between electron and hole transport occurs in the charge stability diagram if the mutual capacitance is neglected (see figure 3 (d)) [6]. However, considering C_m, electron and hole transport are separated by the mutual capacitive coupling, forming triple points where three charge states intersect. In the triangular areas in the gate space around the triple points, a measurable conductance can be observed. The sizes of these triangles directly relate to the applied bias voltage. The base of these triangles is the common energy axes (δ-axis). At right angles to the δ-axis is the detuning axis, or ϵ-axis, where the QDs' electrochemical potentials shift relative to each other. The maximum detuning at which current can still flow happens when the detuning equals the bias window, and both QDs' electrochemical potentials line up with one of the reservoirs. Figure 3 (c) shows the CSD when there is a strong interdot coupling between the two QDs.

Charge Stability Diagram when the superconductor is not grounded

In the section on superconductor-semiconductor junction, the family of andreev processes was described when the superconductor was grounded. What would happen if the superconductor is ungrounded or floating? The answer to this question will be described here. In a system with a superconductor coupled to two quantum dots, quasiparticle poisoning can occur under certain conditions. Quasiparticle poisoning refers to the presence of non-superconducting quasiparticles (e.g., single electrons) in the superconductor. When the superconductor is grounded, it is effectively connected to a reference point of zero potential (e.g., the Earth). This grounding can create a pathway for the dissipation of excess charge or energy, including quasiparticles. In a system with two quantum dots, where charge transport can occur, any non-superconducting quasiparticles generated by the quantum dots or other sources may have a pathway to exit the superconductor through the grounded connection. This process can lead to quasiparticle poisoning, as the presence of non-superconducting quasiparticles can disrupt the formation and dynamics of Cooper pairs. In contrast, when the superconductor is ungrounded, there may be less efficient pathways for the dissipation of excess charge or

energy, including quasiparticles. Without a direct connection to a reference point of zero potential, the quasiparticles generated within the system may remain trapped or localized within the superconductor. As a result, the probability of quasiparticle poisoning decreases because there are fewer pathways for the quasiparticles to escape the superconductor [1]. Fabrication of superconductors parallel to the semiconducting channel, as shown in studies of cooper pair splitters [1] has enabled charge transport without the presence of quasiparticle states. The measurement scheme with an ungrounded superconductor leads to CAR and ECT currents without ABS. It would be interesting to notice the difference between ECT and CAR currents when the superconductor is grounded and ungrounded. Here, the CSD will be studied for two systems wherein for the first one the presence of an ungrounded superconductor parallel to the semiconducting channel and finite charging energy for the superconductor diminishes the probabilities of occurrence of single quasiparticles [1]. The devices fabricated for this thesis consist of superconductors perpendicular to the semiconducting channel and grounding them can lead to the appearance of CSD as studied in [9].

In Cooper pair splitting of electrons, it is important to be able to retain the spin of split electrons to study entanglement. One technique for studying the spins of split electrons is dispersive gate sensing (DGS) [10]. With DGS it is possible to detect changes in parities for the coupled QDs [11, 12]. Measurement of the Charge Stability diagram (CSD) can help identify if ECT or CAR has occurred. Figure 4 shows the CSD for the left and right QD whose electrochemical potentials are tuned using V_{G1} and V_{G2} (FG voltages). The appearance of red lines in these hexagonal CSD represents the case when an electron is transferred from the ungrounded superconductor to the left QD (CAR). The orange lines in these hexagonal CSD represent the case when an electron is transferred from the superconductor to the right QD (CAR). Whereas, the blue lines showcase electron co-tunneling where an electron tunnels directly from the left QD to the right QD [13, 14] without the formation of single quasiparticles in the superconducting island. The electron number in the left QD, superconductor, and right QD can be denoted as ($n_{QD,L}$, n_S, $n_{QD,R}$). In the case when the charging energy of the superconductor (E_S) is much lower than the lowest energy odd parity state (in the absence of magnetic fields) of the superconductor (E_0) the transitions from (0 2 0) to (1 0 1) are possible. When (E_S) and (E_0) are comparatively closer quasiparticle poisoning occurs leading to (1 1 0) or (0 1 1) states thus suppressing the splitting of cooper pairs across the left and right arms [15, 2].
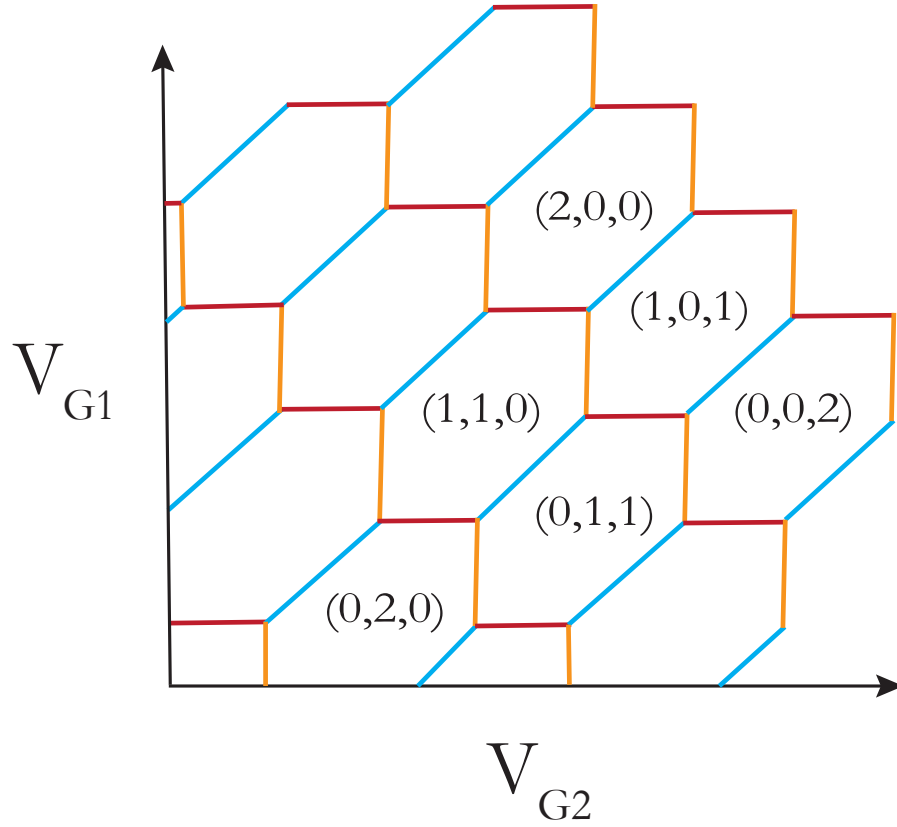
Figure 4: Charge Stability Diagram for a double QD in proximity to a superconductor. The illustration shows the formation of hexagonal-shaped coulomb-blockaded regions when the finger gate voltages for two QDs on the left and right sides of the superconductor are tuned. The blue lines represent the direct co-tunneling of electrons from the left dot to the right. Whereas the red and orange lines represent a transfer of an electron from the superconductor to the left dot and right dot respectively. The figure is adapted from [1].

The occurrence of CAR or ECT processes via the superconductor depends on the coherence length and length of the superconductor. CAR is suppressed by a factor of $e^{-L/\pi\xi}$ where ξ is superconducting coherence length [16]. To measure entanglement it is important to maintain a ratio for E_0/E_S much greater than one or by reducing the length of the superconductor relative to the coherence length. Charge sensing is possible when the DQDs are probed by DGS leading to the change in parities of coupled QDs which can be observed in CSD as shown in figure 4. The hexagonal-shaped structures represent regions of coulomb blockade which can be distinguished with DGS. Thus it is possible to

observe cooper pair splitting by controlling finger gate voltages across the QDs. When the levels of QD are spin-polarized the electrons that have entered the left and right dots become selective to spin measurements in the presence of charge detectors. This enables the verification of the Bell-inequality test for two spin qubits with Clauser-Horne-Shimony-Holt inequality [17, 18].

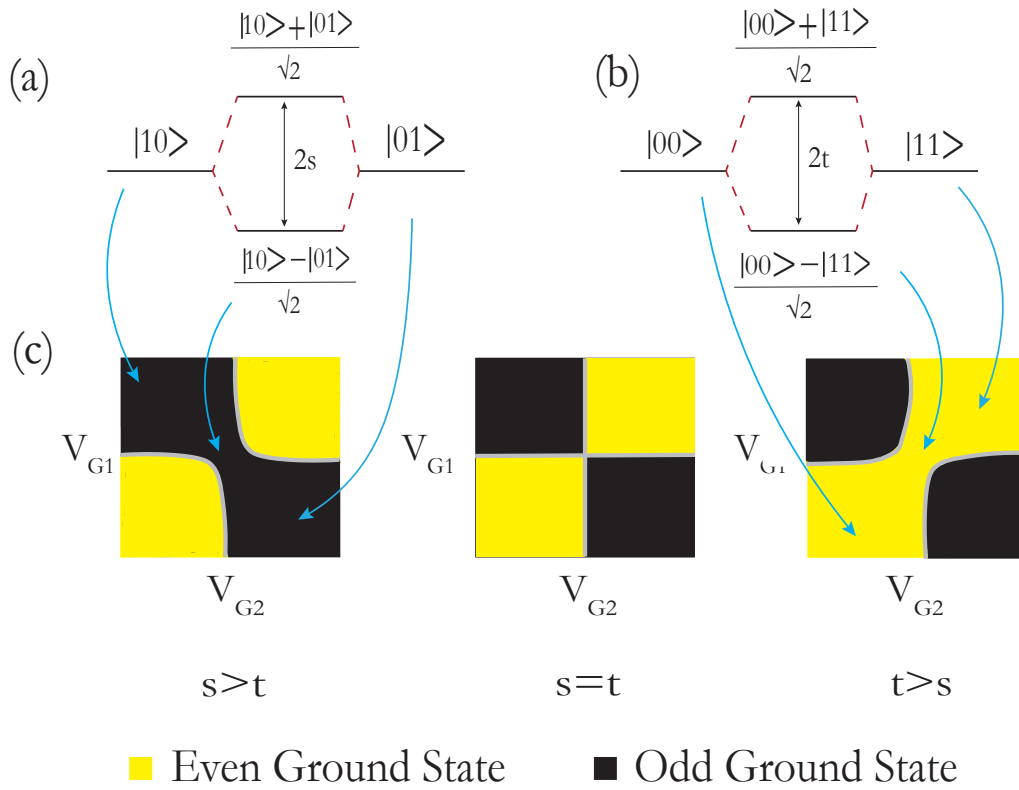**Charge Stability Diagram for Grounded Superconductor**

Figure 5: (a) The ECT process involves the formation of bonding and antibonding states with (1,0) and (0,1). (b) The CAR process involves the formation of bonding and antibonding states with (0,0) and (1,1). (c) Charge Stability diagrams with yellow colored regions representing even ground state and black regions representing odd ground state. The center of all three squares is the region of charge degeneracy. The figure is adapted from [9]

In the presence of single quasiparticle states in the superconductor the charge stability diagrams are no longer the same. The amplitude for ECT transition via an ABS in the superconductor is assumed to be 's' while that for CAR can be assumed to be 't'. ECT

results in eigenstates of the form $\alpha \left| 10 \right\rangle + \beta \left| 01 \right\rangle$ whereas CAR results in eigenstates of the form $u \left| 00 \right\rangle + v \left| 11 \right\rangle$. When the amplitude of ECT signals is higher than CAR (s $\rangle$ t) the odd bonding state is dominant as compared to the even bonding state at the charge degeneracy point of coupled QDs whereas when CAR signals are stronger than ECT the even bonding state is dominant as compared to odd bonding state at charge degeneracy (see s$\rangle$t and t$\rangle$s in 5 (c)). When s=t the ABS peaks are strongly visible because of the formation of even and odd pairs of symmetry states [9].

Bibliography

[1] Damaz de Jong, Christian G. Prosko, Lin Han, Filip K. Malinowski, Yu Liu, Leo P. Kouwenhoven, and Wolfgang Pfaff. Controllable single cooper pair splitting in hybrid quantum dot systems. *Phys. Rev. Lett.*, 131:157001, Oct 2023.

[2] H. Q. Nguyen, D. Sabonis, D. Razmadze, E. T. Mannila, V. F. Maisi, D. M. T. van Zanten, E. C. T. O'Farrell, P. Krogstrup, F. Kuemmeth, J. P. Pekola, and C. M. Marcus. Electrostatic control of quasiparticle poisoning in a hybrid semiconductor-superconductor island. *Phys. Rev. B*, 108:L041302, Jul 2023.

[3] Thomas Ihn. *Semiconductor Nanostructures: Quantum States and Electronic Transport*. Oxford University Press, 2010.

[4] Luca Banszerus. *Gate-defined quantum dots in bilayer graphene*. PhD thesis, 2nd Institute of Physics A, RWTH Aachen, August 2022.

[5] C. Volk. *Quantum transport in graphene nanostructures*. PhD thesis, RWTH Aachen University, 2015.

[6] W. G. van der Wiel, S. De Franceschi, J. M. Elzerman, T. Fujisawa, S. Tarucha, and L. P. Kouwenhoven. Electron transport through double quantum dots. *Rev. Mod. Phys.*, 75:1–22, Dec 2002.

[7] Tobias Deuben. Landau-zener-st¨uckelberg-majorana spectroscopy on bilayer graphene double quantum dots. Master's thesis, 2nd Institute of Physics A, RWTH Aachen, December 2023.

[8] Deividas Sabonis. *Superconductor - Semiconductor Quantum Dots in InAs/Al Nanowires for Majorana based Quantum Information*. PhD thesis, University of Copenhagen, August 2017.

[9] Tom Dvir, Guanzhong Wang, Nick van Loo, Chun-Xiao Liu, Grzegorz P. Mazur, Alberto Bordin, Sebastiaan L. D. ten Haaf, Ji-Yin Wang, David van Driel, Francesco Zatelli, Xiang Li, Filip K. Malinowski, Sasa Gazibegovic, Ghada Badawy, Erik P. A. M. Bakkers, Michael Wimmer, and Leo P. Kouwenhoven. Realization of a minimal kitaev chain in coupled quantum dots. *Nature*, 614(7948):445–450, February 2023.

[10] Antti Ranni, Fredrik Brange, Elsa T. Mannila, Christian Flindt, and Ville F. Maisi. Real-time observation of cooper pair splitting showing strong non-local correlations. *Nature Communications*, 12(1), November 2021.

[11] Damaz de Jong, Jasper van Veen, Luca Binci, Amrita Singh, Peter Krogstrup, Leo P. Kouwenhoven, Wolfgang Pfaff, and John D. Watson. Rapid detection of coherent tunneling in an InAs nanowire quantum dot through dispersive gate sensing. *Phys. Rev. Appl.*, 11:044061, Apr 2019.

[12] K. D. Petersson, C. G. Smith, D. Anderson, P. Atkinson, G. A. C. Jones, and D. A. Ritchie. Charge and spin state readout of a double quantum dot coupled to a resonator. *Nano Letters*, 10(8):2789–2793, July 2010.

[13] *Single Charge Tunneling*. Springer US, 1992.

[14] F. R. Braakman, P. Barthelemy, C. Reichl, W. Wegscheider, and L. M. K. Vandersypen. Long-distance coherent coupling in a quantum dot array. *Nature Nanotechnology*, 8(6):432–437, April 2013.

[15] Sebastian Heedt, Marina Quintero-Pérez, Francesco Borsoi, Alexandra Fursina, Nick van Loo, Grzegorz P. Mazur, Michał P. Nowak, Mark Ammerlaan, Kongyi Li, Svetlana Korneychuk, Jie Shen, May An Y. van de Poll, Ghada Badawy, Sasa Gazibegovic, Nick de Jong, Pavel Aseev, Kevin van Hoogdalem, Erik P. A. M. Bakkers, and Leo P. Kouwenhoven. Shadow-wall lithography of ballistic superconductor–semiconductor quantum devices. *Nature Communications*, 12(1), August 2021.

[16] Martin Leijnse and Karsten Flensberg. Coupling spin qubits via superconductors. *Physical Review Letters*, 111(6), August 2013.

[17] Juan P. Dehollain, Stephanie Simmons, Juha T. Muhonen, Rachpon Kalra, Arne Laucht, Fay Hudson, Kohei M. Itoh, David N. Jamieson, Jeffrey C. McCallum, Andrew S. Dzurak, and Andrea Morello. Bell's inequality violation with spins in silicon. *Nature Nanotechnology*, 11(3):242–246, November 2015.

[18] John F. Clauser, Michael A. Horne, Abner Shimony, and Richard A. Holt. Proposed experiment to test local hidden-variable theories. *Phys. Rev. Lett.*, 23:880–884, Oct 1969.